

SURFACE ANALYSIS TECHNIQUES FOR METALLURGICAL APPLICATIONS

Carbonara/Cuthill

 STP 596

AMERICAN SOCIETY FOR TESTING AND MATERIALS

SURFACE ANALYSIS TECHNIQUES FOR METALLURGICAL APPLICATIONS

A symposium
sponsored by ASTM Subcommittee E02.02
on Surface Analysis of ASTM Committee E-2 on
Emission Spectroscopy
AMERICAN SOCIETY FOR
TESTING AND MATERIALS
Cleveland, Ohio, 4 March 1975

ASTM SPECIAL TECHNICAL PUBLICATION 596
R. S. Carbonara and J. R. Cuthill, editors

List price \$15.00
04-596000-28



AMERICAN SOCIETY FOR TESTING AND MATERIALS
1916 Race Street, Philadelphia, Pa. 19103

© by American Society for Testing and Materials 1976
Library of Congress Catalog Card Number: 75-39442

NOTE

The Society is not responsible, as a body,
for the statements and opinions
advanced in this publication.

Printed in Baltimore, Md.
March 1976

Foreword

The symposium on Surface Analysis Techniques for Metallurgical Applications was held in conjunction with the 1975 Pittsburgh Analytical Conference in Cleveland, Ohio, 4 March 1975. Subcommittee E02.02 on Surface Analysis of Committee E-2 on Emission Spectroscopy sponsored the symposium. G. L. Mason, Canada Center for Mineral and Energy Technology, served as organizing chairman of the symposium. J. R. Cuthill, National Bureau of Standards, presided as symposium chairman at the morning session, and A. H. Gillieson, Canada Center for Mineral and Energy Technology, presided at the afternoon session. R. S. Carbonara, Battelle Columbus Laboratories, and R. J. Koch, Armco Steel Corporation, along with Mason and Cuthill, served as the symposium committee.

Related ASTM Publications

Metallography—A Practical Tool for Correlating the Structural Properties of Materials, STP 557 (1974), \$24.25, 04-557000-28

Manual on Electron Metallography Techniques, STP 547 (1973), \$5.25, 04-547000-28

Electron Beam Microanalysis, STP 506 (1972), \$3.75, 04-506000-28

A Note of Appreciation to Reviewers

This publication is made possible by the authors and, also, the unheralded efforts of the reviewers. This body of technical experts whose dedication, sacrifice of time and effort, and collective wisdom in reviewing the papers must be acknowledged. The quality level of ASTM publications is a direct function of their respected opinions. On behalf of ASTM we acknowledge their contribution with appreciation.

ASTM Committee on Publications

Editorial Staff

Jane B. Wheeler, *Managing Editor*
Helen M. Hoersch, *Associate Editor*
Charlotte E. DeFranco, *Senior Assistant Editor*
Ellen J. McGlinchey, *Assistant Editor*

Contents

Introduction	1
Chemical Analysis of Surfaces—R. L. PARK	3
Some Quantitative Aspects of the X-Ray Photoelectron Spectroscopy Analysis of Metal and Oxide Surfaces—N. S. MCINTYRE AND M. G. COOK	18
ESCA Studies of Nickel-Boron Electroless Coatings—R. S. SWINGLE, II, C. R. GINNARD, AND G. I. MADDEN	28
Composition of Protective Films Formed on Iron and Stainless Steels—J. B. LUMSDEN AND R. W. STAEHLE	39
Quantitative Auger Electron Spectroscopy with Elemental Sensitivity Factors—L. E. DAVIS AND A. JOSHI	52
Application of Auger Electron Spectroscopy to the Study of Embrittlement in Nickel—J. M. WALSH AND N. P. ANDERSON	58
Determination of the Low Temperature Diffusion of Chromium Through Gold Films by Ion Scattering Spectroscopy and Auger Electron Spectroscopy—G. C. NELSON AND P. H. HOLLOWAY	68
Comparison of Evaporated Surface Coatings Using the Ion Scattering Spectrometer and the Auger Electron Spectrometer—W. D. BINGLE	79
Chemistry of Metal and Alloy Adherends by Secondary Ion Mass Spectroscopy, Ion Scattering Spectroscopy, and Auger Electron Spectroscopy—W. L. BAUN, N. T. MCDEVITT, AND J. S. SOLOMON	86
Errors Observed in Quantitative Ion Microprobe Analysis—D. E. NEWBURY, K. F. J. HEINRICH, AND R. L. MYKLEBUST	101
Small Area Depth Profiling with the Ion Microprobe—T. A. WHATLEY, D. J. COMAFORD, JOHN COLBY, AND PAUL MILLER	114
Analysis of Solids Using A Quadrupole Mass Filter—R. D. FRALICK, H. J. RODEN, AND J. R. HINTHORNE	126
Summary	141
Index	145

Introduction

The 12 papers in this volume, which were presented at the Symposium on Surface Analysis Techniques for Metallurgical Applications in Cleveland, March 1975, embrace the following four surface analysis techniques: (1) ion scattering spectroscopy (ISS), (2) Auger electron spectroscopy (AES), (3) electron spectroscopy for chemical analysis (ESCA), which is also known as X-ray-induced electron spectroscopy (XPS), and (4) ion microprobe mass analysis/secondary ion mass spectroscopy (IMMA/SIMS). These techniques, using commercial equipment, have been perfected only during the last decade. These are powerful analytical techniques that have been shown to have application to many types of metallurgical problems that are dependent upon surface composition. Their use is now expanding beyond the bounds of the fundamental research laboratories and into industrial control laboratories. This has prompted the establishment of ASTM Subcommittee E02.02 on Surface Analysis. This symposium, presenting state-of-the-art applications of these surface analysis techniques to an illustrative range of metallurgical surface problems, was one of the first activities of this Subcommittee.

But the purpose of this symposium was more than just to illustrate the range of applications of these techniques; there are characteristic differences between the types of chemical composition information provided by the four techniques due to the inherent nature of the respective techniques. The message carried by the symposium is that one or another of the techniques may be more helpful in a particular problem because of the inherent way in which the particular technique looks at the "surface." Also, because of these inherent differences, a combination of techniques will often yield critical complementary information. No one surface analysis technique is categorically better for all applications.

The keyword in the comparison of the surface analysis techniques is "surface." The surface in each case is defined by the technique itself in that the depth of the material sampled, that is, from a single atomic layer to several layers, is a function of the technique. However, this seemingly variable interpretation of a surface can be looked upon as a strength of this group of surface analysis techniques because the very range of physical phenomena that these techniques are being called upon to

explain, often lumped together under the general heading of surface phenomena, can involve anything from islands of monolayer films of contaminant, to a full monolayer, to several atomic layers, and even to diffusion gradients and selective diffusion phenomena. Some types of examples, though not necessarily in the same order, are: catalytic phenomena, bonding of coatings, composition of coatings, corrosion, bonding of laminates, fracture of spot welded electrical leads, wear and abraded surfaces, heat treated surfaces, and dopant distribution in semiconductors. Some specific cases of these categories of surface problems, and the application of ISS, AES, XPS, or IMMA/SIMS to the problem, are discussed in detail in the papers that follow.

J. R. CUTHILL

Institute for Materials Research, National
Bureau of Standards, Washington, D. C.
20234; symposium cochairman.

R. S. CARBONARA

Battelle Columbus Laboratories, Durham,
N.C.; symposium cochairman.

R. L. Park¹

Chemical Analysis of Surfaces

REFERENCE: Park, R. L., "Chemical Analysis of Surfaces," *Surface Analysis Techniques for Metallurgical Applications, ASTM STP 596*, American Society for Testing and Materials, 1976, pp. 3-17.

ABSTRACT: All methods of elemental identification depend on a determination of either the mass or the charge of the atomic nucleus. The nuclear charge can be inferred from the energy required to create a vacancy in an inner electron shell or from the energies of the electronic transitions involved in the decay of the vacancy. The masses are determined from the recoil momentum imparted to a noble gas ion or by removing atoms from the surface, by sputtering or high electric fields, for analysis in a mass spectrometer. Quantitative analysis, which is not yet possible, will depend on an understanding of structural information contained in secondary features of the spectrum such as line shapes or ion yields.

KEY WORDS: spectroscopy, chemical analysis, surfaces, contamination, chemical shift, X-ray photoelectron spectroscopy, characteristic loss spectroscopy, appearance potential spectroscopy, retarding analyzer, cylindrical mirror analyzer, Auger electron spectroscopy, soft X-ray emission, proton induced X-rays, ion scattering spectroscopy, Rutherford scattering, secondary ion mass spectroscopy, atom probe, field-ion microscope, field desorption spectrometer

The surface region of a solid may be defined as the layer in which the atomic potentials differ from those of atoms still deeper within the solid [1].² This includes those substrate atoms which sense the loss of translational symmetry, as well as adsorbed foreign atoms. This surface region determines the characteristics of the solid with respect to lubrication, corrosion, catalysis, emissive properties, and adhesion; yet prior to 1967, no general method existed by which the surface composition could be analyzed. The materials scientist is confronted today with a choice between some dozen possible techniques for the analysis of surface elemental composition [2]. All of these methods depend on a determina-

¹ Director, Center of Materials Research, and professor, Department of Physics and Astronomy, University of Maryland, College Park, Md. 20742.

² The italic numbers in brackets refer to the list of references appended to this paper.

tion of either the mass or the charge of the atomic nucleus. The strategems by which these properties are deduced are the subject of this symposium.

It is not surprising in a field of such recent origin that much remains to be learned about the effective use of these tools. In this introductory paper, therefore, it is my intention to take a critical view of surface analysis techniques and to emphasize the problems at least as much as the promise.

Scorekeeping

As each technique is discovered (or rediscovered) it must go through a period of contrived enthusiasm during which it is extolled as a cure for every infirmity. Any objective evaluation of these claims must consider first the parameters by which spectroscopies are measured.

Band Width and Statistical Noise

A unifying feature of the surface spectroscopies is their reliance on a vacuum environment. Even at a pressure of 10^{-10} torr a complete monolayer of contamination could condense on a surface in about 2 h. This contamination rate determines the maximum time constant that can be tolerated in a surface experiment.

The imposition of a finite time interval in which a measurement must be completed results in an unavoidable statistical uncertainty. This "shot effect" is a consequence of the fact that the signal consists of discrete quanta. Despite the finite contamination time, it might be supposed that we could reduce the shot noise indefinitely by increasing the rate at which we sample the surface (that is, increase the source intensity). There are however practical limitations on the intensity that can be achieved in X-ray sources or beams of electrons or ions.

Demolition

Delicate surfaces, of course, cannot tolerate an intense probe beam. Electron bombardment induces desorption; incident ions cause sputtering; high electric fields may tear the surface apart, etc. Indeed, these generally disagreeable side effects provide the means for an important class of spectroscopies in which the nature of the surface is inferred by sifting through the rubble created from its destruction. Photons are probably the least destructive probes of the surface, and this is an important advantage of X-ray photoelectron spectroscopy (XPS). Just how important it is depends on the strength of the surface bonds.

Sensitivity and Background

Let us suppose that the surface we are examining is sufficiently refractory so that we can ignore the damage inflicted by the probe beam.

Does this imply that by increasing the intensity we can detect ever weaker features of the spectrum? Unfortunately, it does not.

The sensitivity of every analytical technique is limited ultimately by a background which is correlated in some way with the desired signal. Changes in the background level with time, due to small variations in any parameter of the measurement system, will completely obscure a weak signal. Thus, improvements in sensitivity result from the reduction of background levels.

It is important to distinguish the sensitivity of a technique, which is a measure of its detection threshold, from its band width, which is a measure of the speed with which the spectrum can be acquired.

Resolution

All spectroscopic measurements rely on the limited response of the instrument to filter out high frequency noise. However, any cosmetic applied to a spectrum to cover the blemishes of noise may also obscure physical information. Fortunately, nature provides us with fairly clear goals for the resolution of our instruments. Nothing is gained in the core-level spectroscopies by the ability to resolve features separated by less than the width of the core level which is typically a few tenths of an electron volt. In mass analysis techniques, the ability to resolve one atomic mass unit is generally sufficient.

For many purposes it is not important to approach these goals. If the object of the measurement is just the elemental identification of surface atoms, an energy resolution three orders of magnitude greater than the width of a core level may suffice as in proton induced X-rays. It is the secondary features related to chemical bonding that place stringent demands on resolution.

Sampling Depth

The extent to which a measurement is specific to the surface region is determined either by the attenuation of the escaping particles which convey information about the surface or of the probe which excites them. The mechanisms by which a particle loses energy in its passage through a solid are strongly dependent on energy. For electrons, the inelastic mean free path is generally a minimum in the range of 50 to 100 eV and may be as short as 3 Å [3].

The stopping of an electron by a solid leaves the lattice essentially undisturbed, although adsorbed gas layers may be removed. For ions, however, the situation may be very different. At very high energies (~1 MeV) The principal loss mechanism is by electronic excitation and ions may penetrate very deeply [4]. As the energy decreases, momentum coupling becomes more likely, and, at energies below perhaps 10 keV, the

displacement of lattice atoms, including sputtering, accounts for most of the energy loss.

Core-Level Excitation Techniques

The atomic number of a surface atom can be inferred from the energy required to create a vacancy in an inner electron shell. Although the inner shells do not directly participate in chemical bonds, the excitation may be to unoccupied states within a few electron volts above the Fermi energy. The line shapes associated with these transitions thus reflect the local chemical environment of the atoms. The core levels themselves may be shifted measurably by redistributions of the valence electrons. These "chemical shifts" are small compared to the binding energies of the core electrons and do not seriously interfere with elemental identification, but they can provide important information on the chemical state of the atom. Our view of these effects is obscured to some extent by the uncertainty in core electron binding energy which results from the finite lifetime of the core hole. This lifetime broadening may be as little as 0.1 eV for 2p levels and as much as 5 eV for 2s.

X-Ray Photoelectron Spectroscopy

Using a magnetic spectrometer, Robinson and Rawlinson [5] observed in 1914 that the photoelectron energy distribution produced by a monochromatic X-ray beam impinging on a solid contained a number of discrete lines corresponding to electrons excited from the inner levels of the atoms. These electrons must have escaped from the specimen without inelastic scattering. For most photoemitted electrons, however, this is not the case. Robinson recognized that this effect, which he termed "straggling," causes an abrupt increase in the apparent background on the low energy side of each photoelectron peak.

The benefits of a half century of technology have relieved many of the experimental constraints suffered by Robinson and Rawlinson, but few scientists seem to appreciate the problems introduced by straggling. Attempts to correct for it usually involve some sort of arbitrary subtraction, but in fact the step is the convolution product of the "true" photoelectron peak with a function that must resemble the secondary electron energy distribution [6]. To extract accurate line shapes and positions is thus a difficult theoretical problem that has not yet been attacked.

Burdensome though inelastic straggling may be from the standpoint of line shape analysis, it alone is responsible for the surface sensitivity of XPS and many of the other surface spectroscopies. Thus, the sharp peak is composed of electrons which have lost essentially zero energy in escaping from the solid and must therefore have originated very near the

surface. The mean free path for inelastic scattering may vary from as little as 3 Å for 50 eV electrons to 30 Å at 1000 eV [3].

The XPS spectrum is complicated by the presence of Auger electron emission lines resulting from the decay of the core holes vacated by the photoelectrons. We will discuss the Auger process in detail later.

Core-Level Characteristic Loss Spectroscopy

The relative simplicity of electron sources as compared to X-ray sources makes it attractive to consider doing the XPS experiment with incident electrons rather than X-rays. Unfortunately, incident electrons, unlike photons, have no hesitation in transferring only part of their energy to a core electron. Thus, the backscattered electron spectrum will exhibit only weak edges where XPS gives strong peaks. The shape of this edge is to a first approximation given by the local density of conduction band states. Thus, it is a potentially powerful source of information on the chemical nature of the surface.

Unfortunately, the strong electron-electron interaction, necessary for the technique to be surface sensitive, results in a great many secondary electrons which did not scatter from core levels. To enhance the sharp but relatively weak core level ionization edges, the higher frequency Fourier components of the spectrum can be selectively amplified by measuring the derivative of the spectrum. This amounts to weighing each Fourier component by its frequency [7]. To make much use of these features, however, they must still be distinguished from the stronger and far more abundant Auger peaks.

This distinction depends on the fact that the ionization edges are fixed relative to the incident electron energy, whereas the Auger features are fixed relative to the Fermi energy. One method of making this distinction is to oscillate the incident electron energy about some value and detect only those features in the secondary electron spectrum which vary synchronously [8].

The potential value of this technique lies in the shape of the ionization edges, which should closely resemble X-ray absorption edges, but its main use has been to resolve ambiguities in Auger emission spectra.

Appearance Potential Spectroscopy (APS)

Excitation spectroscopy has its roots early in this century when, in 1911, Franck and Hertz provided one of the first and most direct proofs of the existence of discrete atomic energy states [9]. They determined the threshold potential for inelastic scattering of electrons from atoms in a metal vapor and correlated this threshold with the appearance of characteristic light emission. This concept was extended during the 1920's to the core levels of atoms in a solid and used to construct X-ray energy-level diagrams of the elements. The method, a forerunner of modern APS, consisted of detecting abrupt, albeit small, changes in the total X-ray yield

of an anode as a function of the applied potential [10]. It was not a very sensitive method because of the large bremsstrahlung background, which tends to obscure the subtle changes in total yield that result from the excitation of characteristic X-rays.

This limitation was only recently overcome with potential modulation differentiation and synchronous detection to extract the thresholds from the smoothly varying bremsstrahlung background [11] (Fig. 1). In this form, soft X-ray APS represents the highest resolution core-level spectroscopy available. It is also a remarkably simple technique, in the sense of being uncomplicated rather than easy! Failure to appreciate this distinction has led to some disenchantment among dilettantes.

Both the simplicity and the high resolution are a consequence of the fact that no dispersive analyzer is required. It is the energy of the incident electrons that is measured, and this is determined simply by the potential applied between the specimen and a thermionic emitter. Thus, the resolution is ultimately limited only by the thermal spread in electron energies. The photocurrent from a metal surface exposed to X-rays from the specimen can serve as a measure of the total X-ray yield; such a spectrometer has roughly the complexity of an ion gage. The efficiency of the photoelectric detection scheme is, however, quite low. To compensate most researchers use incident electron currents of several milliamps.

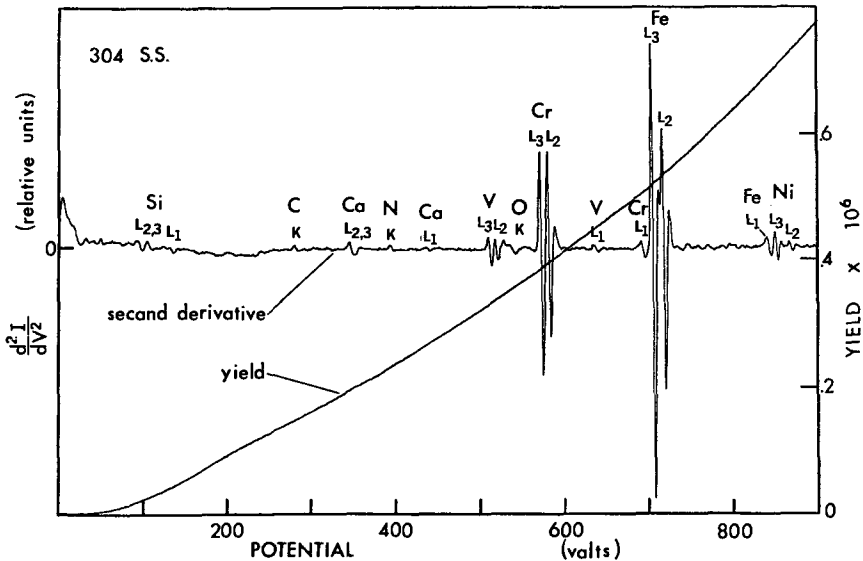


FIG. 1—Soft X-ray appearance potential spectrum of a Type 304 stainless steel surface showing the enhancement of the excitation edges by differentiation. The edges correspond to the minimum energy required to excite a core hole. Vanadium, which is easily distinguished in this spectrum, is difficult to separate from oxygen and chromium Auger features in XPS and AES. The spectrum was obtained by Park [6].

These high currents are easily achieved even at low energies since a focused beam is not required, but fragile surfaces may be destroyed by such a bombardment. More sensitive detection schemes utilizing solid-state detectors can reduce the incident current by two orders of magnitude and have recently been used to study the spectrum of chemisorbed gases [12].

Binding energies determined by APS are identical to those obtained by XPS to within experimental uncertainty [13]. Therefore, spectral features can generally be identified unambiguously from standard X-ray tables. There is, however, an enormous variation in sensitivity to different elements depending on the density of states above the Fermi energy, the fluorescent yield, and the oscillator strength connecting the core level to states above the Fermi energy [14]. Thus, although APS has been used to study elements from lithium to uranium in the form of metals, semiconductors, and insulators, at least two elements, palladium and gold, do not exhibit detectable thresholds with existing methods.

To a first approximation the shape of an appearance potential edge should be given by the self convolution of the density of unoccupied states broadened by the width of the core level [14]. The self convolution arises because both the incident and excited core electrons must fit into the available states.

Core Hole Recombination

All of the techniques discussed thus far determine the energy required to create a core vacancy. This vacancy will be filled by an electron from a higher level as the atom, in a series of transitions, convulses its way back to the ground state. Energy is conserved in the decay transitions by the emission of X-ray photons or Auger electrons.

Electron-Excited Auger Electron Spectroscopy (AES)

Auger electron emission peaks were first identified in secondary electron energy distributions by Lander in 1953, but only the most intense Auger transitions could be identified above the background of other secondary events [15]. Electron excited Auger spectroscopy thus did not appear to offer a sensitive method of elemental surface analysis. Fifteen years later, however, Harris demonstrated the remarkable enhancement of the relatively sharp Auger features that can be achieved by differentiation [16].

The acceptance of AES was facilitated because many surface physicists already had spherical grid low energy electron diffraction (LEED) systems that could be converted to retarding-potential energy analyzers by the addition of external electronics [17]. Because of the obvious advantages of coupling LEED and Auger, the retarding analyzer remains an important instrument. For applications where LEED would be irrelevant,

there is wide use of the cylindrical mirror electrostatic deflection analyzer [18] which permits the spectrum to be scanned in a relatively short period of time. As with all deflection analyzers, the percent resolution is fixed. This severely distorts the spectrum, but at low energies it approximately compensates for the increasing background and gives a more aesthetic spectrum.

The acquisition of the spectrum, however, may be far simpler than its interpretation. The complexity results from the fact that an Auger line represents term differences between three levels. For a heavy element the L-shell Auger spectrum alone consists of hundreds of lines, the energies of which are not susceptible to precise first principle calculations. Generally, it is possible to identify spectral groups but not individual features within those groups (Fig. 2). Serious ambiguities, therefore, arise in the identification of Auger transitions for all but the lightest elements, and elemental analysis is generally based on matching spectra against "standard" plots taken from the specimens of known composition.

If one or both of the final state holes lies in the valence band, it should be possible to interpret the Auger line shape in terms of the density of states. Unfortunately, few Auger spectra have been taken with the resolution (<1 eV) required to extract this kind of information. The line shape is, in any case, complicated by straggling. Attempts to correct for this by subtracting out some assumed background are without justification. The line shape often serves as a "fingerprint" of the surface condition, however, even where it cannot be analyzed in terms of a density of states [20].

Soft X-Ray Emission Spectroscopy (SXE)

The escape depth of a soft X-ray photon is orders of magnitude greater than for an electron of the same energy. Thus, the classic method of soft X-ray band spectra is generally regarded as a bulk probe. By using grazing-incidence electrons to excite the X-rays, however, it is possible to confine the sampling depth to the outermost layers of the solid [21]. Such studies were initially undertaken to avoid the distortion caused by self absorption; the elimination of self absorption is equivalent, of course, to probing only the outermost layer of a solid. This technique was exploited in 1967 by Sewell and Cohen to examine the composition of a surface while simultaneously studying its crystallography by reflection high-energy electron diffraction (RHEED) [22]. A month earlier, however, Weber and Peria had published news of the first use of a LEED system to obtain an Auger spectrum [17]. Auger electron spectroscopy has since become the most popular surface analytical technique, whereas only a handful of laboratories persist in SXE. The different reception accorded the two techniques is an indication of relative difficulty of detecting and energy analyzing soft X-rays. The soft X-ray spectrum is, however, less

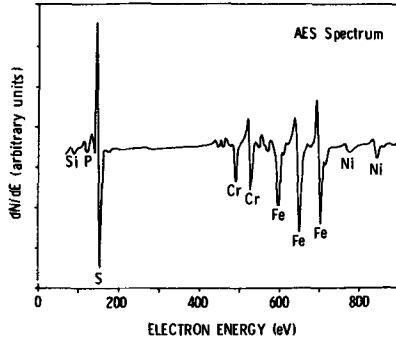


FIG. 2—Electron-excited Auger electron spectrum of Type 304 stainless steel. Individual peaks represent term differences between three levels and generally cannot be uniquely identified. Elemental analysis is based on comparison with spectra of known specimens. The AES is remarkably sensitive to sulfur, which does not show up in the other techniques. The figure was obtained by Musket [19].

complex than the AES because only two levels are involved, and the interpretation of line shapes is correspondingly simplified (Fig. 3).

Proton Induced X-Rays (PIX)

The technologist is inclined to regard the dependence of spectral line shapes on chemical environment as more of a hindrance than a help, because these effects are imperfectly understood and may interfere with determinations of elemental abundance. This suggests that it might be advantageous for some purposes to degrade the resolution of our spectrometers deliberately to make them insensitive to changes in line shape. If, however, we excessively degrade the resolution, the background may begin to overwhelm the signal.

The sensitivity of electron-excited soft X-ray emission, for example, is generally limited by a background of bremsstrahlung radiation produced by the radiative capture of incident fast electrons. The collision of energetic ions with a solid, on the other hand, results in negligible bremsstrahlung. This has led to the use of ion-induced X-rays in the analysis of surface composition. Protons are used most frequently, but heavier ions may have advantages in some cases. The X-rays produced are of course characteristic of the projectile as well as the target.

The comparatively weak signals encountered in PIX analysis rule out the use of dispersive analyzers; measurements are made instead with solid-state detectors [24]. The achievable energy resolution of such detectors is approximately 140 eV which rather overachieves the objective of making the spectrum insensitive to line shape. Although it may dismay electron spectroscopists accustomed to thinking of resolution in terms of tenths of electron volts, it is frequently adequate for elemental analysis (Fig. 4).

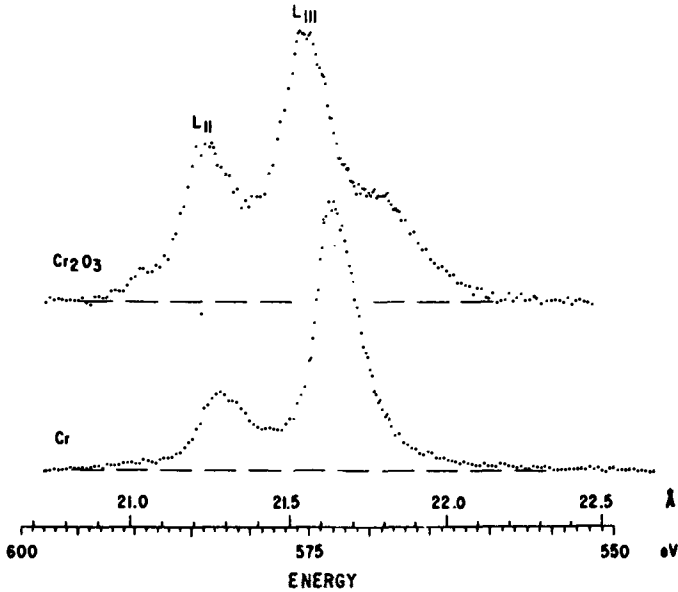


FIG. 3—Soft X-ray emission spectra of the chromium $L_{2,3}$ bands from chromium and from chromium sesquioxide. The shapes of the peaks have not been analyzed but it is clear that they provide a fingerprint of the chemical environment of the chromium atoms. The spectra were obtained by Holliday and Frankenthal [23].

Considering the cost of the accelerators and the quality of the information obtained, it would be difficult to rationalize the use of PIX for surface analysis, were it not for its use in combination with Rutherford scattering which we will describe later in the paper.

Ion Backscattering

The collision of energetic ions with a surface has several consequences in addition to the production of characteristic X-rays. The incident ions may impart sufficient momentum to the specimen to cause sputtering, or they may recoil either as ions or as neutrals. The energies of these backscattered particles can generally be treated within the framework of classical mechanics, changes in their internal energy being, for the most part, a small perturbation.

Ion Scattering Spectroscopy (ISS)

When an ion approaches a surface it is highly probable that it will be neutralized by an electron tunneling from the solid. Some ions, however, survive the encounter and are backscattered as ions. It is observed experimentally that for noble gas ions in the energy range of a few hundred electron volts, the encounter with the surface can be described as

a simple elastic binary collision [25]. Thus the masses of the atoms on the surface can be determined from the recoil momentum of the backscattered ions (Fig. 5).

If the mass of the incident ion is greater than the mass of the surface atoms, it cannot be backscattered. If, on the other hand, the mass of the incident ion is much less than that of the surface atoms, the difference in momentum due to scattering from similar masses cannot be resolved. These contradictory requirements often necessitate the use of several different probe gases to obtain a complete analysis.

When the ion beam first impinges on a clean surface, the spectrum is extremely difficult to interpret because of the high probability of multiple scattering collisions. As the beams disrupts the surface order, the structure due to multiple scattering is washing out and only the single scattering peaks remain [27]. The possibility of using the multiple scattering peaks for structure analysis is an intriguing but largely unexploited possibility [28]. One advantage of this method at present seems to be the ease with which it can be used in sputter profiling.

Rutherford Scattering

At energies two or three orders of magnitude greater than those used in ISS, the cross section for displacement collisions is very much lower and ions lose energy principally to electronic excitations. Under these conditions, an ion may penetrate relatively deeply before being backscattered. It is assumed generally that before and after the backscattering event the ion gives up energy uniformly. If the stopping power is accurately known, the energy spectrum of backscattered high-energy ions provides a mea-

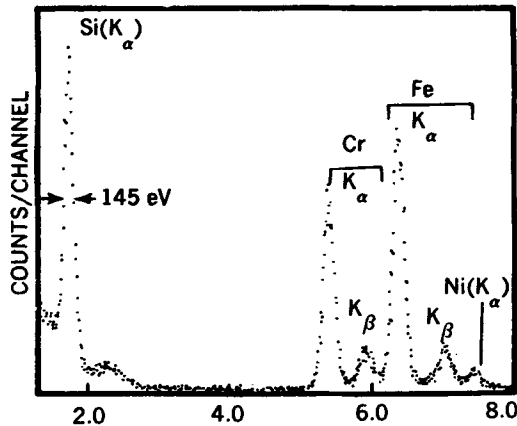


FIG. 4—Proton induced X-ray spectrum of a Type 304 stainless steel surface. Despite a resolution of ~ 140 eV it is possible to resolve most of the common constituents of stainless steel, but there is no chemical information in the line shapes. This spectrum was obtained by Bauer and Musket [24].

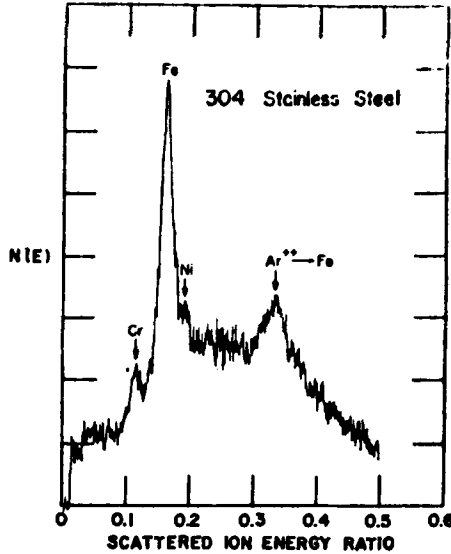


FIG. 5—Ion scattering spectrum of a Type 304 stainless steel surface. 1500-eV A^+ ions were used to probe the surface. Chromium, iron and nickel are just resolved. Elements of mass < 40 cannot be detected without using a lighter probe gas such as neon ($M = 20$, but the resolution of chromium, iron, and nickel would be worse). The spectrum was obtained by Goff and Smith [26].

sure of thickness of a surface film. Combined with ion-induced X-ray analysis, Rutherford scattering is a powerful technique for thin film analysis.

Removal Spectroscopies

The composition of a surface can be inferred by sifting through the rubble created from its destruction. Perhaps the most obvious way to remove material from a surface is to increase its temperature. Weakly bound molecules can also be desorbed by electron impact which may excite the molecule from its normal attractive state to a positively ionized repulsive state. These processes are, however, too selective in their effect to provide much information on surface composition, although they are useful in studying binding states. We must seek more general techniques.

Secondary Ion Mass Spectroscopy (SIMS)

The impact of energetic ions provides a very general method of removing surface material, some of which will be charged. The method of SIMS [29] consists of measuring the mass-to-charge ratios of these sputtered ions by conventional mass analysis techniques (Fig. 6).

For certain atoms, particularly the alkalis, the probability that they will sputter as ions is quite high and leads to truly remarkable sensitivity. The

probability that a sputtered atom will be ionized, however, can vary by three or four orders of magnitude depending on its chemical environment. This severely limits the use of SIMS for any sort of quantitative measurements, but this chemical sensitivity most certainly will be exploited. No other method can boast of a parameter which is so dependent on chemical bonding.

Variations in the SIMS approach have been devised that provide information on the spatial distribution of surface atoms, either by rastering a fine ion beam over the surface or by using the ion optics of the mass filter to image the area covered by the incident ion beam.

Atom-Probe Field Ion Microscope (FIM)

The field-ion microscope depends on the high electric fields that can be created at a sharp metal point to ionize noble gas atoms [31]. The ions are accelerated away from the point to a fluorescent screen where they produce an image of the point in which spots identified with individual surface atoms are clearly resolved.

If the field is further increased, surface atoms themselves are torn from the tip as ions. These field-evaporated ions follow the same trajectories as the noble gas ions. This has been exploited to analyze the mass-to-charge ratio of the desorbed ions corresponding to a selected surface region, by desorbing a surface layer by a narrow voltage pulse, and timing the flight of desorbed surface ions to a detector at the end of a long drift tube (Fig. 7). The sensitivity of the atom-probe FIM is the highest of any analytical technique in existence, but its band width is quite low. That is, to obtain meaningful statistics the experiment must be repeated many times.

Field-Desorption Spectrometer (FDS)

The gated field desorption microscope uses a pair of concentric curved channel plate electron multiplier arrays as an image intensifier to

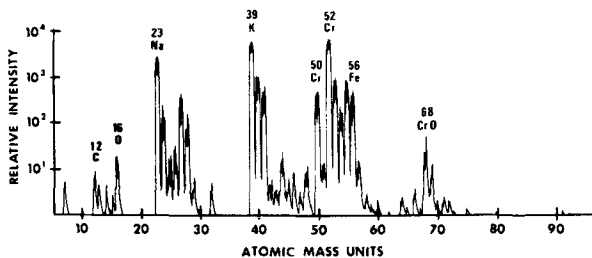


FIG. 6—Secondary ion mass spectrum of a stainless steel surface bombarded with 2-keV A^+ ions. The intense sodium and potassium peaks are the result of a high yield as ions rather than a large abundance; CrO^+ is observed but no FeO^+ , indicating that the oxygen is bound on chromium sites. The spectrum was obtained by Schubert [30].

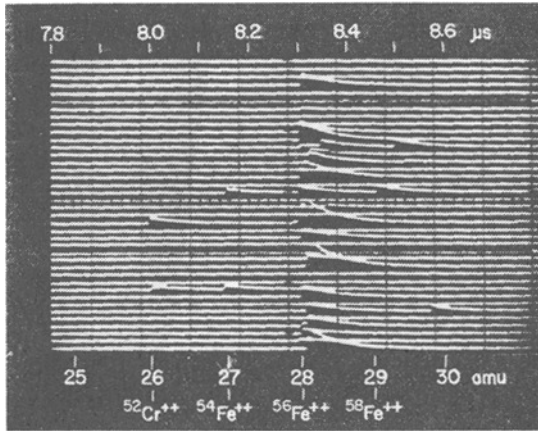


FIG. 7—Field evaporated time-of-flight spectra of a stainless steel tip surface with a radius of $\sim 800 \text{ \AA}$. A large number of such traces are required to obtain good statistics on composition. The spectra were obtained by Krishnaswamy et al [32].

record the arrival of pulse desorbed ions. By time gating the image intensifier to coincide with the arrival of an ion of preselected mass-to-charge ratio, an image of the complete crystallographic distribution of this species over the surface of the point is obtained [33].

Alternatively, the multiplier current can be monitored as a function of time following the pulse to obtain a complete spectrum of the elements present on the surface. The resolution is not as good as that achieved with the atom probe because of the short drift length, but it offers an elegant method of analyzing metal specimens which can be fabricated into the required sharp point.

“Quantitative” Surface Analysis

With so many techniques for the study of surface composition at our disposal, it might seem a small matter to perform the calibrations required to quantify our results. Indeed, extravagant claims of “quantitative” surface analysis have been published [34]. Such claims are rooted in an unclear notion of what the problem is.

The misapprehension is that we should be able to define the surface composition by attaching a percentage to each element as we do for homogeneous bulk specimens. This has no definite meaning for the surface, which is necessarily inhomogeneous along its normal. However, the composition might be stated in percentages layer by layer. Thus a precise statement of surface composition must include the atomic arrangement. This is still beyond our best efforts for all but the simplest cases.

What can be done? I think we must place greater emphasis on the

secondary features of spectra that convey information on chemical structure. This includes line shapes, chemical shifts, ion yields, multiple scattering peaks, etc. Unfortunately, these effects are generally imperfectly understood and often obscured by the poor response of our instruments. These spectroscopies were, of course, developed initially to meet the needs of basic research, and it is to basic research that we must turn for their refinement.

References

- [1] Park, R. L. in *Experimental Methods in Catalysis*, Vol. II, R. A. Anderson and P. W. Dawson, Eds., Academic Press, New York, 1975.
- [2] Park, R. L. in *Surface Physics of Crystalline Solids*, J. M. Blakely, Ed., Academic Press, New York, 1975.
- [3] Powell, C. J., *Surface Science*, Vol. 44, 1974, p. 29.
- [4] Lindhard, J., Nielsen, V., Scharff, M., and Thomsen, P. V., *Matematisk-fysiske Meddelelser, Kongelige Danske Videnskabernes Selskab*, Vol. 33, No. 10, 1963.
- [5] Robinson, H. and Rawlinson, W. F., *Philosophical Magazine*, Vol. 28, 1914, p. 277.
- [6] Park, R. L., *Physics Today*, Vol. 28, April 1975, p. 52.
- [7] Houston, J. E. and Park, R. L., *Review of Scientific Instruments*, Vol. 43, 1972, p. 1437.
- [8] Gerlach, R. L., Houston, J. E., and Park, R. L., *Applied Physics Letters*, Vol. 16, 1970, p. 179.
- [9] Franck, J. and Hertz, G., *Verhandlungen der Deutschen Physikalischen Gesellschaft*, Vol. 16, 1911, p. 12.
- [10] Richardson, O. W. and Bazzoni, C. B., *Philosophical Magazine*, Vol. 42, 1921, p. 1015.
- [11] Park, R. L. and Houston, J. E., *Journal of Vacuum Science and Technology*, Vol. 11, 1974, p. 1.
- [12] Andersson, S., Hammarqvist, H., and Nyberg, C., *Review of Scientific Instruments*, Vol. 45, 1975, p. 877.
- [13] Webb, C. and Williams, P. M., *Physical Review Letters*, Vol. 33, 1974, p. 824.
- [14] Park, R. L., *Surface Science*, Vol. 48, 1975, p. 80.
- [15] Lander, J. J., *Physical Review*, Vol. 91, 1953, p. 1382.
- [16] Harris, L. A., *Journal of Applied Physics*, Vol. 39, 1968, p. 1419.
- [17] Weber, R. E. and Peria, W. T., *Journal of Applied Physics*, Vol. 38, 1967, p. 4355.
- [18] Sar-el, H. Z., *Review of Scientific Instruments*, Vol. 38, 1967, p. 1210.
- [19] Musket, R. G., *Journal of Vacuum Science and Technology*, Vol. 9, 1972, p. 603.
- [20] Haas, T. W. and Grant, J. T., *Physics Letters*, Vol. 30A, 1969, p. 272.
- [21] Cuthill, J. R. in *X-Ray Spectroscopy*, L. V. Azaroff, Ed., McGraw-Hill, 1974.
- [22] Sewell, P. B. and Cohen, M., *Applied Physics Letters*, Vol. 11, 1967, p. 298.
- [23] Holliday, J. E. and Frankenthal, R. P., *Journal of the Electrochemical Society*, Vol. 119, 1972, p. 1190.
- [24] Bauer, W. and Musket, R. G., *Journal of Applied Physics*, Vol. 44, 1973, p. 2606.
- [25] Smith, D. P., *Journal of Applied Physics*, Vol. 38, 1967, p. 340.
- [26] Goff, R. and Smith, D. P., *Journal of Vacuum Science and Technology*, Vol. 7, 1970, p. 72.
- [27] Heiland, W., Schäffler, H. G., and Taglauer, E., *Surface Science*, Vol. 35, 1973, p. 381.
- [28] Brongersma, H. H., *Journal of Vacuum Science and Technology*, Vol. 11, 1974, p. 231.
- [29] Benninghoven, A., *Surface Science*, Vol. 35, 1973, p. 427.
- [30] Schubert, R., *Journal of Vacuum Science and Technology*, Vol. 11, 1974, p. 903.
- [31] Muller, E. W. and Tsong, T. T. in *Field Ion Microscopy*, American Elsevier, New York, 1969.
- [32] Krishnaswamy, S. V., McLane, S. B., and Muller, E. W., *Journal of Vacuum Science and Technology*, Vol. 11, 1974, p. 899.
- [33] Panitz, J. A., *Journal of Vacuum Science and Technology*, Vol. 11, 1974, p. 206.
- [34] Change, C. C. in *Characterization of Solid Surfaces*, P. F. Kane and G. B. Larrabee, Eds., Plenum, New York, 1974.

N. S. McIntyre¹ and M. G. Cook¹

Some Quantitative Aspects of the X-Ray Photoelectron Spectroscopy Analysis of Metal and Oxide Surfaces

REFERENCE: McIntyre, N. S. and Cook, M. G., "Some Quantitative Aspects of the X-Ray Photoelectron Spectroscopy Analysis of Metal and Oxide Surfaces," *Surface Analysis Techniques for Metallurgical Applications, ASTM STP 596*, American Society for Testing and Materials, 1976, pp. 18-27.

ABSTRACT: Using metal and metal oxide surfaces as examples, three aspects of quantitative X-ray photoelectron spectroscopy are discussed, namely, the effects of surface contamination and structure, dilution effects in mixtures, and the influences of stoichiometry on photoelectron intensity ratios. The intensity attenuating effect of carbon was determined for several types of surfaces, and, in all cases, a quasi-linear relationship was found between the intensities of carbon and those of the specimen matrix. The slope of the line is dependent upon the surface structure of the matrix as well as the kinetic energy of the matrix photoelectron. Excess oxygen in an oxide matrix has little effect on the metal and oxide line intensities, but heavy metal impurities incorporated into the surface strongly attenuate the matrix lines. The metal line intensities from copper-nickel and iron-nickel alloys were determined as a function of composition. The intensity of each component varied linearly with the atomic fraction indicating that the electron scattering cross section is not significantly different in these metals or their alloys. Quantitative measurement of these surfaces is practical only when the more deeply probing M(3p) electron lines are used. Oxygen/metal photoelectron intensity ratios are a reproducible property of a particular oxide. Their ratios, however, are altered not only by changes in stoichiometry, but to some extent by changes in structure. Quantitative analysis of an oxide surface is thus reliable only for specimens where the oxide structure is identical to the standard throughout the compositional range of interest.

KEY WORDS: spectroscopy, photoelectron spectroscopy, X-ray photoelectron spectroscopy, stoichiometry, surface analysis, surface finishing, metals, oxides

¹ Whiteshell Nuclear Research Establishment, Atomic Energy of Canada Limited, Pinawa, Manitoba, Canada.

The practicability of quantitative measurements using X-ray photoelectron spectroscopy (XPS) was demonstrated in the early work of Siegbahn et al [1].² Relative elemental photoelectron cross sections have since been measured for a large segment of the periodic table by Wagner [2] and by Jorgensen and Berthou [3], and calculations of cross sections have recently been made by Scofield [4] which are in generally good agreement with earlier experimental data. Although the use of XPS line intensities for surface analytical measurements has not been discussed very widely in the literature, some industrial laboratories have been using XPS intensities in an empirical manner for several years to help characterize particular chemical and catalyst systems. In this laboratory, we have been concerned with the XPS analysis of metal oxide systems, and, as part of this program, line intensities for a number of oxides and metals have been recorded under various conditions and their relationship to surface composition has been studied. In this paper we discuss several different intensity effects encountered in this study and their relevance to the quantitative analysis of surfaces.

Experimental

A McPherson ESCA-36 electron spectrometer was used for all the work reported. In this nonretarding spectrometer, photoelectron intensity is a linear function of kinetic energy [5], and intensities reported are corrected for this, unless otherwise stated. The specimen surface is mounted at 45 deg to the incident X-ray beam and to the acceptance slit. Specimen chamber pressures were maintained below 1.33×10^{-6} Pa by cryogenic pumping.

Results and Discussion

Effects of Surface Contamination and Structure

Carbon is the major contaminant on most metals and metal oxides studied by XPS. Some carbon is known to result from the background hydrocarbon vapor pressure in the spectrometer specimen chamber, and its rate of deposition is found to sharply increase when the X-ray beam is on. In other cases, the carbon appears to have been present on the original sample surface. In either case, the observed C(1s) binding energy, normally 285.0 ± 0.2 eV, is that found for a long chain aliphatic hydrocarbon. Since the surface carbon is often of mixed origin and little structural information is obtained from the binding energy, the presence of the carbon is of little value except to sometimes act as a surface charging reference [1].

The attenuating effect of carbon on other photoelectron intensities has

² The italic numbers in brackets refer to the list of references appended to this paper.

been studied for several different surface structures. Figure 1 shows the effect of surface carbon contamination for the integrated intensities of Fe(2p), Fe(3p), and O(1s) photoelectrons emerging from a magnetite (Fe_3O_4) surface. The carbon was introduced during the growth of the oxide on an iron base and was removed gradually in the spectrometer by a very light flux (20 mA/m^2) of 10-keV argon ions. The intensity of photoelectrons from the magnetite matrix varies inversely with the C(1s) intensity, and these contamination response curves can be extrapolated to give Fe(2p), Fe(3p), and O(1s) intensity values for zero contamination. Experiments with other magnetite surfaces all gave zero carbon intercepts within 10 percent of these values. For a given C(1s) intensity, the relative attenuation is greater for the lower kinetic energy Fe(2p) line than for the Fe(3p) line. A small change in the O(1s)/Fe(3p) ratio occurs as a function of carbon intensity because of differing kinetic energies of the two matrix lines.

The effect of carbon contamination on photoelectron intensities from zirconia (ZrO_2) surfaces was also studied. A number of separate zirconium and zircaloy surfaces were prepared using different chemical and abrasive treatments. These were oxidized in a variety of air and water environments. The surfaces were analyzed over a period of several months, and the resultant signifies Zr(3d) intensities are plotted against their corresponding C(1s) intensity in Fig. 2. Despite the apparently high probability of different forms of carbon contamination being present on

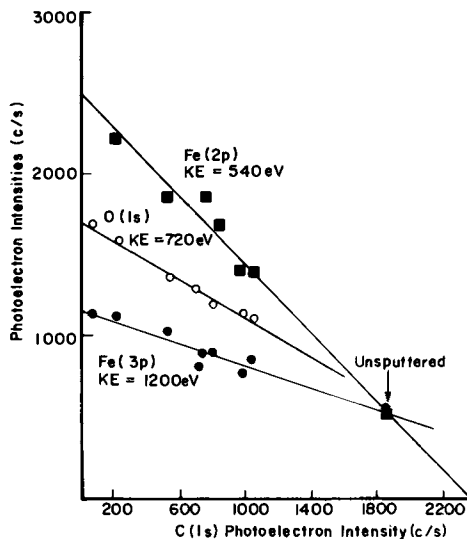


FIG. 1—Attenuation of Fe(2p), Fe(3p) and O(1s) electrons by carbon on a magnetite surface. The intensities of the O(1s) and Fe(2p) electrons are not corrected for kinetic energy.

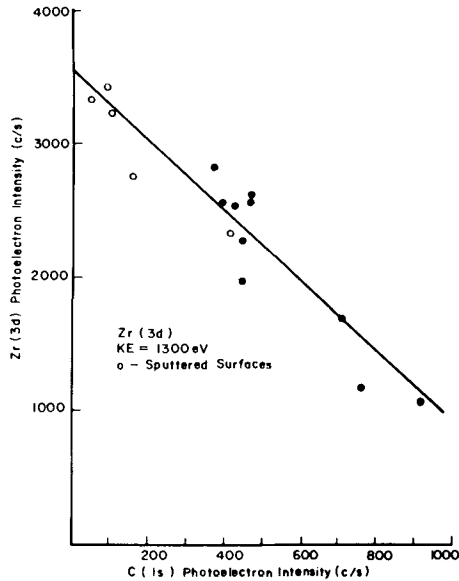


FIG. 2.—Attenuation of $Zr(3d)$ photoelectrons by carbon on ZrO_2 .

different zirconia surfaces, the contamination response curve again can be represented by a straight line. The carbon on one particular surface was removed gradually by ion bombardment, and the response curve is the same as for carbon deposited under experimental conditions. Note that the relative attenuation of ZrO_2 for a given $C(1s)$ intensity is much higher than for magnetite. Contamination response curves have also been determined for copper metal and alumina surfaces, and each surface appears to be affected to a characteristic extent by a given intensity of carbon. The degree to which a matrix is attenuated by carbon may thus depend more on its own characteristic structure than on the nature of the carbon overlayer.

The effect of oxygen in ZrO_2 on various photoelectron intensities has also been studied. In Fig. 3, the $O(1s)$ spectrum shows that two distinct types of oxygen separated by 1.6 eV are observed on ZrO_2 surfaces exposed previously to air. This multipeak structure is also commonly observed in a number of other metal oxide systems. The intensity of the low binding energy $O(1s)$ peak varies directly with the $Zr(3d)$ intensity. This peak represents the more electronegative oxygen, and it is assigned to the lattice oxygen in ZrO_2 . The higher binding energy $O(1s)$ peak has been ascribed in other systems to a form of adsorbed oxygen sitting on the original oxide surface [6,7]. For the ZrO_2 surfaces studied, the adsorbed oxygen intensity relative to lattice oxygen varied from 26 to 140 percent. A plot of adsorbed oxygen intensity against $Zr(3d)$ intensity shown in Fig.

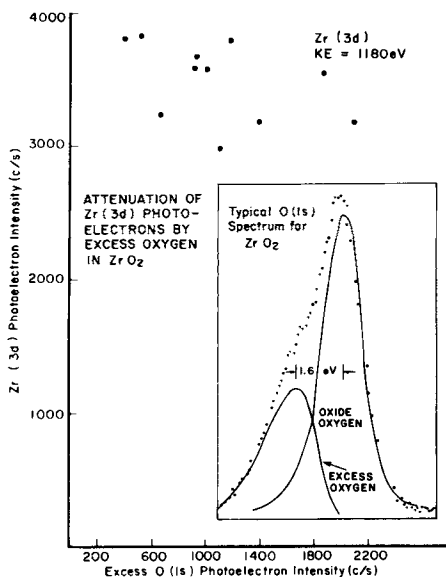


FIG. 3—Attenuation of $Zr(3d)$ photoelectrons by excess oxygen in ZrO_2 .

3 gives no indication that the zirconium intensity is depressed significantly even when this surface oxygen species has a high intensity. The lack of an attenuation effect for adsorbed oxygen is due to the considerably higher sensitivity of XPS to adsorbed oxygen than to carbon contamination. Not only is the $O(1s)$ photoelectron cross section about three times higher than $C(1s)$ at these exciting energies [2–4], but also the oxygen species is situated preferentially on the outermost surface while carbon contamination is distributed more widely through the surface layer. It appears that the intensities of adsorbed oxygen normally observed on metal oxide surfaces do not affect the other matrix intensities significantly.

Surface area also has an effect on the photoelectron intensity from some oxide surfaces. In some previous work [8] the changes in the surfaces of nickel-chromia catalysts were studied by XPS as a function of the catalytic activity. As shown in Fig. 4, the intensity of the $Ni(2p)$ peak, as well as other nickel photoelectron intensities, clearly change with the measured surface area of the oxide. Chromium (III) oxide (Cr_2O_3) is believed to act as a “structural promoter” to lower the nickel particle size and raise its surface area. The effect of surface area can be readily followed by XPS, and, in fact, the XPS intensity could be used as a test of the oxide area in a given catalyst.

During the study of ZrO_2 surfaces, oxide surfaces containing small quantities of other metals were also produced. The incorporation of oxides of these foreign metals into the ZrO_2 lattice results in a reduction in

Zr(3d) intensity that appears to be out of proportion to the quantity of impurity oxide present. For example, on a surface where the corrected Fe(3p) intensity was only 6 percent of the value for pure magnetite, the Zr(3d) intensity was attenuated by 45 percent. This too could have resulted from an induced change in the ZrO_2 surface area; however, due to the small size of the specimen no supporting surface area measurements were obtained. Under conditions where the surface area is affected, even semiquantitative determinations (± 50 percent) become difficult.

Analysis of Metal Alloys

Some intensity effects in alloys have also been studied. For our work involving the surface analysis of nickel rich alloys [9] a series of copper-nickel and iron-nickel alloys were prepared and their photoelectron intensity calibration curves were studied. Some XPS studies of copper-nickel [10,11] and gold-silver [10,12] alloys have been previously published.

Melts of the appropriate compositions were swaged, annealed, and quenched in such a manner as to retain a solid solution across the composition ranges. All specimen surfaces were argon ion sputtered to remove surface oxidation products. For each specimen the M(2p) and M(3p) intensities were plotted against the atomic percent determined for the bulk specimen by chemical analysis. In Fig. 5, the plots for all M(3p) lines show a very clear linear response with bulk composition, and this linearity indicates that the inelastic scattering coefficients for Cu(3p), Ni(3p), and Fe(3p) electrons at 1200 eV can be considered identical [12].

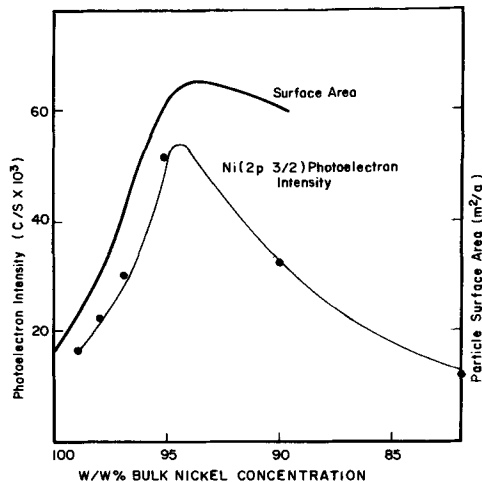


FIG. 4—Effect of the surface area of nickel on the nickel photoelectron intensity.

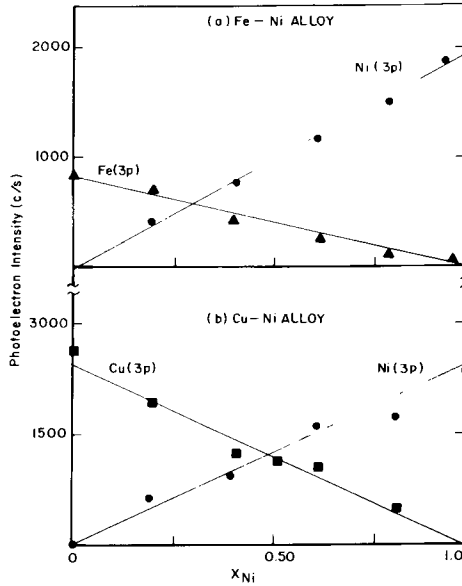


FIG. 5— $M(3p)$ photoelectron intensities as a function of bulk composition in some copper-nickel and iron-nickel alloys.

With such straightforward calibration curves using $M(3p)$ electrons, the composition of alloys of these metals can be measured with a standard deviation of five percent. Relative cross sections for $Cu(3p)$, $Ni(3p)$, and $Fe(3p)$ in their respective metals were determined to be 1.00:0.81:0.37. The $Fe(3p)/Ni(3p)$ cross-section ratio is particularly low compared with Scofield's calculated relative values of 1.00:0.91:0.69 [4].

In Fig. 6 the $Cu(2p)$ and $Ni(2p)$ intensities are plotted for the sputtered copper-nickel alloys series. A distinct curvature is seen for the intensities of the low energy $Cu(2p)$ electrons. It is likely that this represents a true depletion in surface copper concentration rather than a change in the scattering cross section for copper in the alloy. Ebel [11] has studied the ratio of $Cu(2p)/Ni(2p)$ intensities in alloys whose surfaces were not sputtered and has found very little curvature over the same concentration range. The sputtering-induced depletion of copper from copper-nickel alloy surfaces has also been suggested by the Auger electron results of Quinto et al [13]. Such depletion must occur only on the extreme outer surface layer since the response from the $Cu(3p)$ line deviates less than 10 percent from linearity. In the iron-nickel alloys, the response for the $M(2p)$ lines is quite erratic giving no indication that one constituent is preferentially sputtered. Quantitative surface measurements require the use of higher kinetic energy photoelectron lines (>1000 eV) to minimize the effects of compositional irregularities on the extreme outer surface.

Line Intensity Ratios in Oxides

Knowledge of the oxygen/metal intensity ratio for metal oxide films is useful for quantitative treatment of the matrix or to provide additional identification of the major phase on a surface. This ratio is a discrete property of each oxide species. For example, the measured O(1s)/Zr(3d) ratio for 12 zirconium dioxide surfaces prepared under a variety of conditions had a standard deviation of only 9 percent and similar reproducibility was found for other oxides. The reproducibility is considerably poorer if the lower kinetic energy metal photoelectron lines are used.

To determine the effect of chemical stoichiometry on the oxygen/metal intensity ratios, the O(1s)/M(3p) ratio was measured for a series of copper and nickel oxides. The measured ratios, shown in Fig. 7, clearly increase with the oxygen/metal atomic ratios, but the relationship is not linear. Such deviations probably result from the effect of the different oxide structures on the electron scattering mechanism. Swingle [14] has recently discussed the effect of some of these energy loss mechanisms on the Na(1s)/Fe(1s) ratio in some sodium and fluorine containing compounds.

An extreme example of the effect of structure on the relative photoelectron intensity occurs in the case of cuprous oxide and cupric oxide where, despite the doubling of the copper/oxygen atom ratio, the intensity ratio is hardly changed. Thus, while the intensity ratio is useful as confirmatory evidence of a given oxide species, the true atom ratio can not be inferred

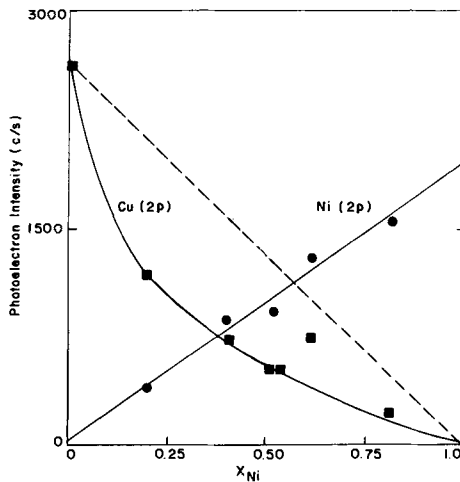


FIG. 6— $M(2p)$ photoelectron intensities in some copper-nickel following argon ion bombardment of the surface.

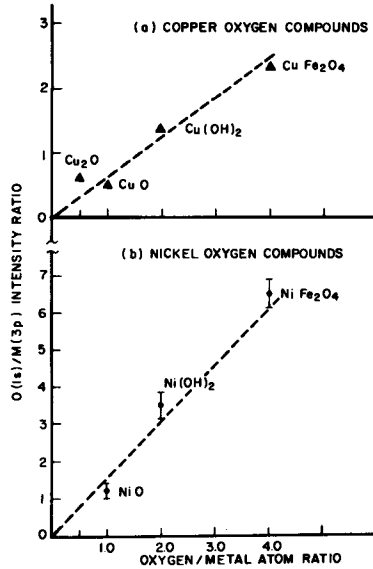


FIG. 7—Effect of chemical stoichiometry on the $O(1s)/M(3p)$ ratio for some copper and nickel oxygen compounds. $M(3p)$ intensities include the areas under shake-up and shake-off structure up to 10 eV above the principal photoelectron line; $O(1s)$ intensities include only the area under the oxide oxygen peak.

with much certainty from intensity data alone. Inclusion of discreet energy loss peaks as part of the ratio may result in more reliable data [14].

Conclusions

We have shown that some of the photoelectron intensity effects due to surface contamination and sputtering damage can be minimized. Photoelectron intensities are normally a reproducible property for a given species. For alloys containing metals of similar scattering cross sections, the photoelectron intensity varies directly with concentration. Similar behavior would be expected if the metals were present in an oxide matrix of consistent structure, but again calibration with a matrix of known structure is first necessary to determine the absolute metal intensities. If the structure of the oxides change within the composition range where analysis is desired, reliable quantitative analysis becomes very difficult. Large changes in the oxide surface area can also affect the accuracy of such an analysis.

Acknowledgments

The authors thank A. Reich for the preparation of the metal alloys and G. Schultz for their chemical analysis.

References

- [1] Siegbahn, K., Nordling, C., Fahlman, A., Nordberg, R., Hamrin, K., Hedman, J., Johansson, G., Bergmark, T., Karlson, S. E., Lindgren, I., and Lindberg, B., *ESCA, Atomic, Molecular, and Solid State Structure Studies by Means of Electron Spectroscopy*, Alqvist and Wiksells, Uppsala, 1967.
- [2] Wagner, C. D., *Analytical Chemistry*, Vol. 44, 1972, p. 1050.
- [3] Jorgensen, C. K. and Berthou, H., *Discussions of the Faraday Society*, Vol. 54, 1972, p. 269.
- [4] Scofield, J. H., Report UCRL-51326, University of California Radiation Laboratory, 1973.
- [5] Sevier, K. D., *Low Energy Electron Spectrometry*, Wiley-Interscience, New York, 1972.
- [6] Robert, T., Bartel, M., and Offergeld, G., *Surface Science*, Vol. 33, 1972.
- [7] Brundle, C. R. and Carley, A. F., *Chemical Physics Letters*, Vol. 31, 1975, p. 423.
- [8] McIntyre, N. S., Sagert, N. H., Pouteau, R. M. L., and Practor, W. G., *Canadian Journal of Chemistry*, Vol. 51, 1973, p. 1670.
- [9] McIntyre, N. S. and Rummery, T. E., to be published.
- [10] Ebel, H. and Ebel, M., *X-ray Spectrum*, Vol. 2, 1973, p. 19.
- [11] Ebel, M., *Journal of Electron Spectry*, Vol. 5, 1974, p. 837.
- [12] Larson, P. E., *Analytical Chemistry*, Vol. 44, 1972, p. 1678.
- [13] Quinto, D. T., Sandaram, V. S., and Robertson, W. D., *Surface Science*, Vol. 28, 1971.
- [14] Swingle, R. S., II, *Analytical Chemistry*, Vol. 47, 1975, p. 21.

R. S. Swingle, II,¹ C. R. Ginnard,¹ and G. I. Madden¹

ESCA Studies of Nickel-Boron Electroless Coatings

REFERENCE: Swingle, R. S., II, Ginnard, C. R., and Madden, G. I., *ESCA Studies of Nickel-Boron Electroless Coatings, Surface Analysis Techniques for Metallurgical Applications, ASTM STP 596*, American Society for Testing and Materials, 1976, pp. 28–38.

ABSTRACT: Electron spectroscopy for chemical analysis (ESCA) has been used to study the surface chemistry of electroless nickel-boron coatings. Changes in relative surface composition and element oxidation state were observed for boron, nickel, thallium, and sulfur as the coating was heated at 10^{-3} torr and heated in air. Under these conditions, boron was more easily oxidized than nickel, accounting for the oxidation resistance of the coating as compared to nickel metal. A small portion of sulfate stabilizer in the coating bath was reduced to sulfide and codeposited during the electroless plating process.

KEY WORDS: spectroscopy, coatings, surface chemistry, electron spectroscopy for chemical analysis, nickel-boron, electroless, X-ray photoelectron

Electroless plating is a process in which metal cations in solution react with a reducing agent to produce a metallic coating on a substrate. Since no electron transfer through the substrate is required, the electroless process can be used to deposit coatings on nonconductive as well as conductive materials.

The preparation of nickel-boron alloys using electroless plating techniques has been described elsewhere in detail [1-5].² The process uses boron-containing reducing agents such as sodium borohydride (NaBH_4) or dimethylamine borane (DMAB) to reduce nickel ions in aqueous solution. Boron is codeposited with the nickel as it is reduced. The

¹ Research chemist, ESCA applications chemist, and senior development specialist, respectively, Central Research and Industrial Chemicals Departments, Experimental Station, E. I. du Pont de Nemours and Company, Wilmington, Del. 19898.

² The italic numbers in brackets refer to the list of references appended to this paper.

resulting nickel-boron alloy is best described as a solid solution that is metastable at room temperature. Heating the "as plated" combination of nickel and boron to temperatures of $\sim 200^\circ\text{C}$ produces crystalline phases of nickel and Ni_3B [6]. These heat treated coatings have Knoop Hardness Numbers (KHN (100)) around 1200 and are more wear resistant than tool steels, hard chromium, and a variety of other metallic coatings.

In addition to hardness or wear resistant applications, nickel-boron coatings are of interest as a possible replacement for gold in the electronics industry. The coatings are electrically conducting, resistant to air oxidation, and can be brazed and soldered readily.

This paper describes our study of electroless nickel-boron coatings with X-ray photoelectron spectroscopy (electron spectroscopy for chemical analysis (ESCA)) [7-8]. The work was undertaken in order to correlate physical properties of the nickel-boron system with changes in surface chemistry resulting from the coating being heated in vacuum and heated in air. The ESCA technique is especially appropriate for this study since it measures changes in atomic surface composition plus changes in the immediate chemical or electronic environment of each element at a surface.

Experimental

Specimen Preparation

The plating bath used to prepare the nickel-boron coatings was operated with the following conditions

reducing agent = NaBH_4 ,
 ph = 12 to 14,
 temperature = 95°C , and
 deposition rate = $15 \mu\text{m/h}$.

In addition to the reducing agent, the bath contained organic complexing agents and stabilizers, including thallium sulfate (Tl_2SO_4) [9] which prevented spontaneous reduction and provided for the formation of uniform coatings. Coatings produced with this bath contained bulk concentrations of nickel, boron, and thallium in approximately a 73:17:1 atomic ratio. (At this concentration, thallium probably substitutes for nickel in the structure of the coating.) Specimen holders made of Type 304 stainless steel were immersed in the coating bath until a nickel-boron coating of $\sim 25 \mu\text{m}$ thickness was deposited.

Instrumentation

The ESCA spectra were taken using a spectrometer designed and constructed at the duPont Engineering Physics Laboratory [10-11]. A signal averager was interfaced to the spectrometer providing the capabil-

ity of coherent addition over energy regions of 10 to 200 eV. The spectrometer was equipped with a stainless steel reaction chamber which permitted specimens to be heat treated from 25 to 500°C in vacuum ($\sim 10^{-5}$ torr) or in the presence of a reactive gas mixture, and subsequently analyzed without exposure to the atmosphere.

Reaction Chamber Conditions

The nickel-boron specimen holder was examined by ESCA after each of the following sequential treatments: (1) as plated, surface cleaned with ethanol, (2) heated to 200°C/90 min/vacuum, (3) heated to 400°C/90 min/vacuum, (4) surface cleaned with ethanol, (5) heated to 200°C/90 min/air, (6) heated to 400°C/30 min/air, (7) surface cleaned with ethanol, and (8) surface mechanically abraded under nitrogen.

Treatments 1, 4, and 7 involved cleaning the specimen surface with a cotton swab saturated with ethanol. Treatment 8 involved polishing the coated specimen holder under nitrogen with an abrasive nylon pad.

Results and Discussion

The results of the ESCA analyses taken after each treatment are summarized in Table 1. Binding energies, E_b , are charge corrected to 854.0 eV for the $\text{Ni}_{2p_{3/2}}$ electrons. Peak intensities are normalized for atomic sensitivity using relative photoelectric cross sections as calculated by Scofield [12]. Changes in atomic ratios from treatment to treatment can only be considered significant when the ratios differ by a factor of ~ 2 or more. Interpretation of smaller differences is limited by possible changes in the electron scattering mechanisms between chemically nonequivalent surfaces [13].

In order to distinguish the effects of temperature on the surface chemistry of the nickel-boron coatings from the effects of high-temperature air oxidation, two sets of experiments were performed. The first set (Treatments 2 to 3) involved heating the coating at 10^{-5} torr in the spectrometer reaction chamber and subsequently analyzing the surface by ESCA without exposing it to the atmosphere. In the second set of experiments (Treatments 4 to 6), the coating was heated in air before ESCA analysis. Finally the surface was partially abraded (Treatment 8) under nitrogen (N_2) in order to distinguish surface from bulk effects.

Effect of Heating in Vacuum

Figures 1 to 3 compare the $\text{B}_{1s}/\text{S}_{2p}$, $\text{Ni}_{2p_{3/2}}$, and $\text{Ti}_{4f_{5/2-7/2}}$ spectra, respectively, for the vacuum heat treatments. At least three distinct B_{1s} lines at ~ 192 , ~ 188 , and ~ 182 eV are evident in Fig. 1. A comparison of these binding energies with those of selected standards (Table 2) indicates that the high E_b peak at ~ 192 eV is due to an oxide or mixed oxide of boron. The peak at 188.0 to 188.5 eV could be due to a number of

TABLE 1—Results of ESCA analyses.

	C-1s		B-1s		Ni-2p _{3/2}			S-2p			
	Elemental ^a	Oxidized	0-1s	Boron Oxides	Borides	Boron Hydride	Ni ²⁺ Ni ₃ B	Ni ²⁺	Tl-4f _{7/2}	Sulfates	Sulfides
CHARGE CORRECTED BINDING ENERGIES											
As plated/ethanol	285.4	288.5	532.8	192.0	188.6	... ^b	854.0	857.5	117.5	169.2	162.6
200°C/vacuum	285.3	289.1	533.2	192.6	188.4	182.3	854.0	...	117.7	169.4	162.7
400°C/vacuum	284.8	...	533.6	193.2	188.1	...	854.0	...	117.5	169.4	162.0
Ethanol	285.1	...	533.2	192.6	188.0	...	854.0	...	117.7	169.7	162.3
200°C/air	284.9	288.1	532.7	192.3	188.3	...	854.0	857.7	118.8	169.1	162.8
400°C/air	284.7	...	532.6	192.7	854.0	857.9	119.4	169.3	...
Ethanol	284.8	...	532.7	192.6	854.0	857.6	119.2	168.8	...
Abraded	285.0	...	532.5	192.0	188.1	...	854.0	...	118.2
NORMALIZED INTENSITIES											
As plated/ethanol	14746	2450	5869	404	1024	...	1331	683	124	250	93
200°C/vacuum	15010	1267	3676	1061	2039	1504	1967	...	98	204	195
400°C/vacuum	5934	...	8103	4720	2392	...	3848	...	98	114	435
Ethanol	10377	...	5505	2492	1933	...	2836	...	59	70	366
200°C/air	11881	2000	7296	1873	1029	...	1291	912	37	98	195
400°C/Air	7343	...	15145	9108	176	861	254	108	...
Ethanol	12368	...	13952	7822	101	608	339	86	...
Abraded	10660	...	5143	600	1014	...	2525	...	254
Relative intensity factors	1.00	1.00	2.85	0.49	0.49	0.49	13.90	13.90	11.80	1.75	1.75

^a Main carbon peak due to surface contaminate
^b Trace amount detected.
^c Not detected.

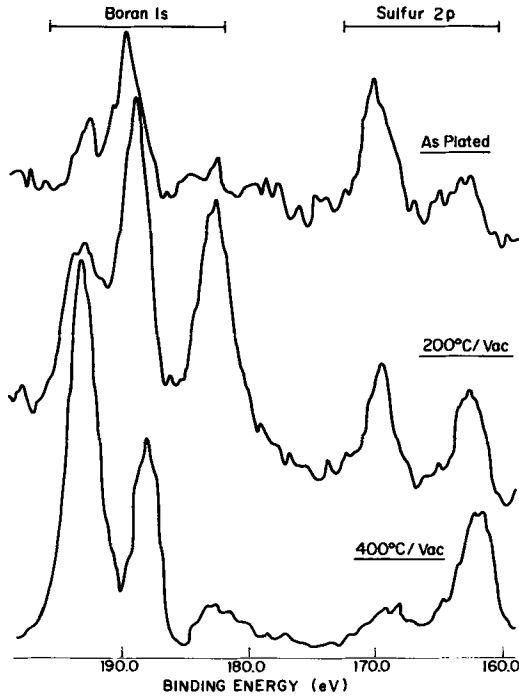


FIG. 1— B_{1s} and S_{2p} spectra after vacuum-heat treatments.

boron-containing species including the intermetallic Ni_3B phase. (Amorphous boron would not be expected to separate from the coating under these conditions and is not a likely source of this peak.) Note that both the ~ 192 eV and ~ 188 eV peaks show small changes in peak widths and relative binding energies from treatment to treatment, indicating that more than one distinct species contributes to each of the peaks. The third peak at 182.0 eV presents a problem in interpretation, since no B_{1s} binding energies this low have been measured in our laboratory for standard compounds or, to our knowledge, have been reported in the literature. However, the peak is almost certainly due to boron since no other reasonable photoelectron or Auger lines occur in this region of the spectrum. (The peak may be due to the borohydride anion randomly distributed in the bulk nickel-boron solid solution, with extra-atomic relaxation [14] of the conduction electrons accounting for the ~ 5 eV difference in binding energy between the observed peak and that from "standard" $NaBH_4$.)

Two sulfur peaks are also shown in Fig. 1. The high E_b peak at 169.3 eV is characteristic of sulfate, probably from the Tl_2SO_4 stabilizer in the bath. The second peak at 162.6 eV is characteristic of a sulfide and suggests that

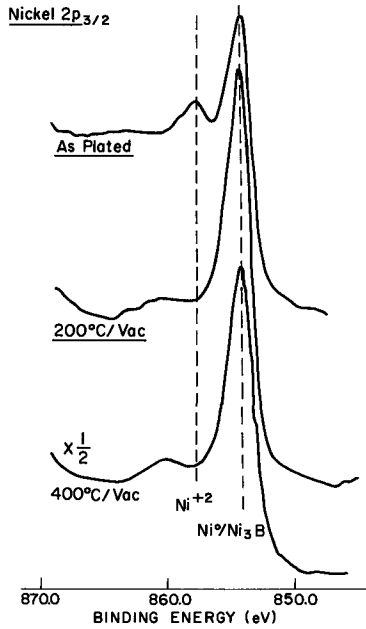

 FIG. 2— $Ni_{2p_{3/2}}$ spectra after vacuum-heat treatments.

 TABLE 2—Binding energies^a of selected standards (eV).

Compound	B _{1s}	Tl 4f _{7/2}	Ni 2p _{3/2}
B (amorphous)	188.3
B ₂ O ₃ (coating on amorphous boron)	192.6
B(OH) ₃	193.1
Tl ₂ O ₃	...	117.0 117.2	...
Tl ₂ CO ₃	...	118.4	...
Tl ₂ SO ₄	...	119.0	...
Ni ⁰	853.9 854.0
Ni ₃ B	187.9	...	854.3
NiB	188.1	...	854.7
NiB ₂	192.7	...	854.9
NiO	856.9 857.0

^a Charge corrected to C_{1s} at 285.0.

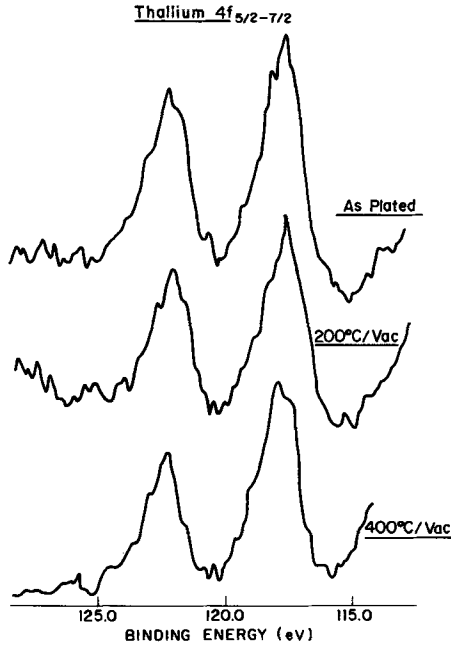


FIG. 3— $Tl_{4f_{5/2-7/2}}$ spectra after vacuum-heat treatments.

some sulfate is reduced to sulfide in the bath and codeposited with the other elements during the plating process.

It is apparent that heating the coating in vacuum significantly alters its surface composition. The total amount of boron at the surface increases, and the two lower E_b boron species are partly oxidized. This oxidation is in sharp contrast to the reduction evident in the sulfur and nickel spectra. Note that the sulfate/sulfide ratio decreased from 2.5 in the as plated condition to 0.25 after heating at 400°C in vacuum. In addition, Fig. 2 shows that the small amount of Ni^{+2} on the surface of the plated coating is removed completely after the first heat treatment. There is no formation of Ni^{+2} even at 400°C where oxidation is more likely. Figure 3 indicates no change in the $Tl_{4f_{5/2-7/2}}$ peak intensities or binding energies under these treatment conditions.

As noted in Table 2, Ni_3B cannot be distinguished from Ni^0 by the $Ni_{2p_{3/2}}$ binding energy. Also, the B_{1s} binding energy from Ni_3B is not unique, and it was not possible to identify by ESCA the formation of the Ni_3B phase with heating. However, the oxidation of boron and the coincident reduction of sulfur and nickel indicated by these spectra may be important chemistry in determining the oxidation resistance properties of these coatings.

Effect of Heating in Air

Figures 4 to 6 compare the B_{1s}/S_{2p} , $Ni_{2p_{3/2}}$, and $Tl_{4f_{5/2-7/2}}$ spectra, respectively, after heating the nickel-boron coating in air. As expected, the surface composition of the coating changes drastically under these treatment conditions. Boron is further oxidized, with only a single boron-oxide peak at 192.7 eV in evidence after heating at 400°C in air (Treatment 6). In addition, the sulfide is reoxidized to sulfate, and the $Ni_{2p_{3/2}}$ spectrum shows both the chemical shift and shake-up satellite structure characteristic of the high-spin +2 nickel oxidation state [15]. Finally, as illustrated in Fig. 6, the thallium peak intensities increase by nearly an order of magnitude after treatment [6], and the $Tl_{4f_{7/2}}$ peak is shifted to 1.7 eV higher E_b when compared to the binding energy observed after the heat/vacuum experiments (Treatment 4).

Note in Fig. 5 that a peak due to Ni^0/Ni_3B is still evident after the sequential 200°/air and 400°/air treatments. In order to observe this peak with the ESCA technique, the oxide layer formed above the Ni^0/Ni_3B cannot have a thickness greater than 2 to 3 times the mean escape depth, λ , of the $Ni_{2p_{3/2}}$ electron [16,17]. Thus, if λ is of the order of 15 to 20 Å, this layer likely has a thickness less than 60 Å. This is somewhat surprising considering the harsh conditions of these sequential treat-

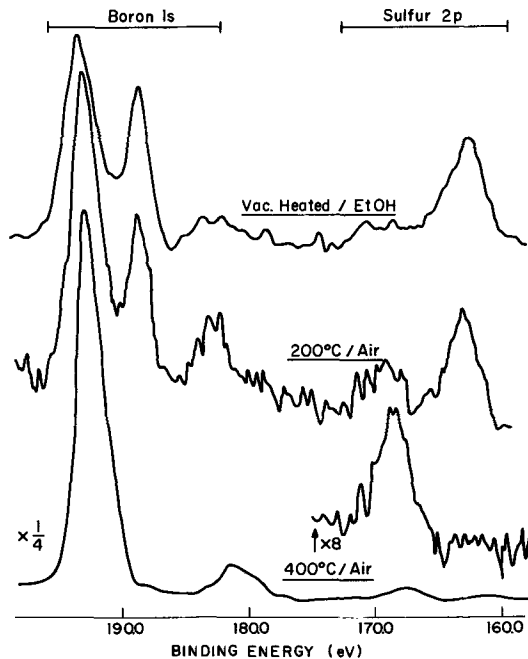


FIG. 4— B_{1s} and S_{2p} spectra after air-heat treatments.

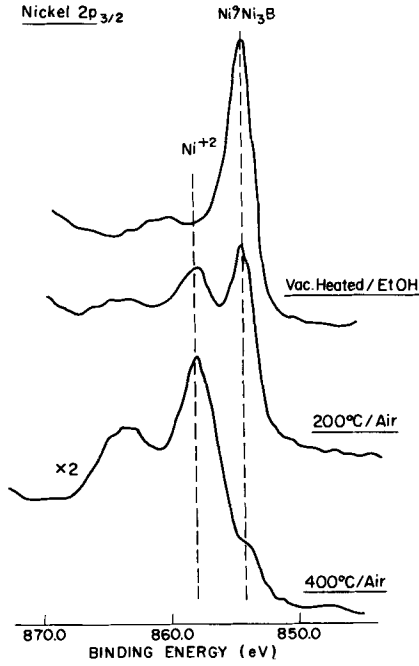


FIG. 5— $Ni_{2p_{3/2}}$ spectra after air-heat treatments.

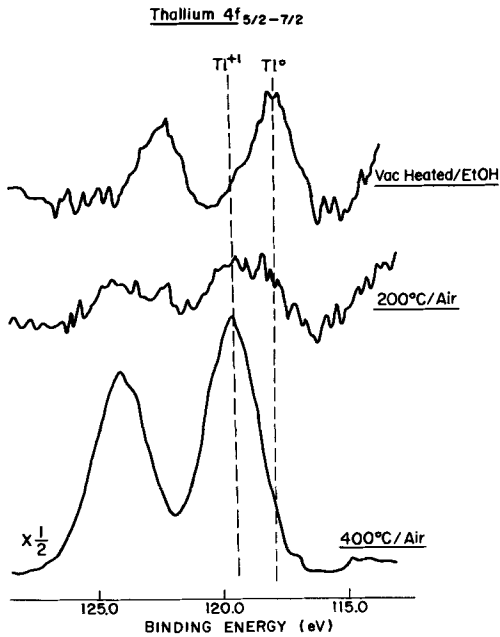


FIG. 6— $Tl_{4f_{5/2-7/2}}$ spectra after air-heat treatments.

ments. (The $\text{Ni}_{2p_{3/2}}$ ESCA spectrum of nickel foil, for example, shows no peak due to Ni^0 after being heated in air at 400°C .) It is apparent that the oxide layer on nickel-boron effectively "passivates" the coating and presents a very strong barrier to further oxidation.

It is not possible from the ESCA data alone to deduce the exact composition of this protective layer; however, several important conclusions concerning its nature are evident. First, the $\text{Ni}_{2p_{3/2}}$ binding energy of the Ni^{+2} species is consistently 0.5 to 0.9 eV higher than that for simple nickel oxide (NiO), suggesting Ni oxidation products other than NiO must be present. Second, the surface layer is thallium rich compared to bulk stoichiometry, and, from Table 2, the thallium is likely oxidized to Tl^{+1} . (Thallium oxide (Tl_2O_3) is not the oxidation product as it has a $\text{Tl}_{4f_{7/2}}$ binding energy ~ 2 eV lower than that observed after the high temperature air oxidation (Treatment 6) of the coating.) Last, in contrast to nickel, all the boron detected after Treatment 6 has been oxidized. Because λB_{1s} is greater than $\lambda \text{Ni}_{2p_{3/2}}$, this result suggests that the oxide layer is not homogeneous with depth and that boron is oxidized preferentially toward the bottom of the layer. This conclusion is in agreement with the preferential boron oxidation noted previously in the vacuum/heat treatments.

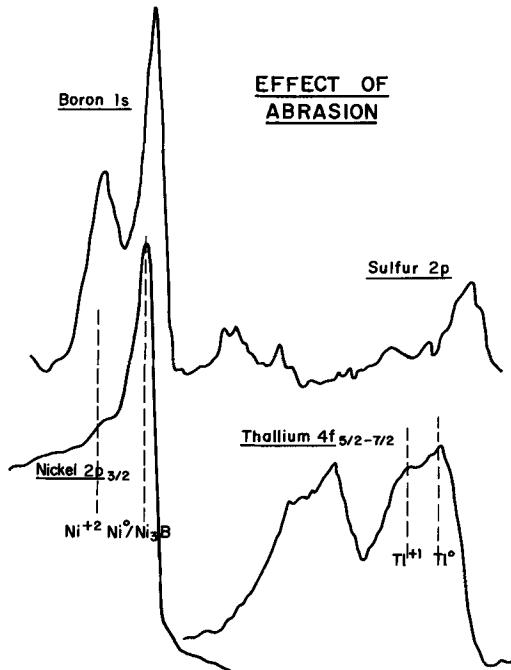


FIG. 7— B_{1s} — S_{2p} , $\text{Ni}_{2p_{3/2}}$, and $\text{Tl}_{4f_{5/2-7/2}}$ spectra after abrasion.

Effect of Abrasion

As shown in Fig. 7, the abrasion process completely removes the Ni^{+2} and reduces by several orders of magnitude the intensity of the B_{1s} peak from the oxidized boron species, relative to that from Ni_3B . The thallium spectrum shows clear evidence of both the 0 and +1 oxidation states and also indicates that the mild abrasion used in Treatment 8 does not reduce significantly the amount of thallium at the surface. Abrasion completely removes sulfate from the surface; however, the trace amount of sulfide detected after abrasion indicates that some sulfur is distributed throughout the coating.

References

- [1] Klein, H. G., Niederprum, H., and Horn, E. M., *Metalloberflaeche*, Vol. 25, No. 9, 1971, p. 305.
- [2] Mallory, G., "Electroless Coatings," Paper 690646, Society of Automotive Engineers, 1969.
- [3] Narkus, H., *Plating*, Vol. 54, 1967, p. 380.
- [4] Berzins, T., E. I. du Pont de Nemours, U. S. Patents 3,045,334 and 3,338,726.
- [5] Dennis, J. K. and Such, T. E. in *Nickel Chromium Plating*, Wiley, New York, 1972, p. 285.
- [6] Portnoi, K. I. et al, *Poroshkovaia Metallurgii*, Vol. 50, No. 2, 1967, p. 15.
- [7] Siegbahn, K. et al, *ESCA: Atomic Molecular and Solid State Structure Studies by Means of Electron Spectroscopy*, Almqvist and Wiksells, Uppsala, Sweden, 1967.
- [8] Siegbahn, K. et al, *ESCA Applied to Free Molecules*, North Holland, Amsterdam, 1969.
- [9] Bellis, H. E., E. I. du Pont de Nemours, U. S. Patent 3,674,447.
- [10] Lee, J. D., *Review of Scientific Instruments*, Vol. 43, 1972, p. 1291.
- [11] Davies, R. D. et al in *Advances in X-Ray Analysis*, L. S. Brics, Ed., Plenum, New York, 1973, Vol. 16, p. 90.
- [12] Scofield, J. H., "Theoretical Photoionization Cross Sections from 1 to 1500 MeV," Technical Report No. 51326, University of California Radiation Laboratory, Livermore, Calif., 1973.
- [13] Swingle, R. S., II, *Analytical Chemistry*, Vol. 47, No. 1, 1975, p. 21.
- [14] Citrin, P. H. and Hamann, D. R., *Physical Review B.*, Vol. 10, 1974, p. 4948; Davis, D. W., Banna, M. S., and Shirley, D. A., *Journal of Chemical Physics*, Vol. 60, 1974, p. 237.
- [15] Tolman, C. A. et al, *Inorganic Chemistry*, Vol. 12, No. 12, 1973, p. 2770.
- [16] Carlson, T. A. and McGuire, G. E., *Journal of Electron Spectroscopy and Related Phenomena*, Vol. 1, No. 2, 1972, p. 161.
- [17] Klasson, M. et al, *Physica Scripta*, Vol. 5, 1972, p. 93.

J. B. Lumsden¹ and R. W. Staehle¹

Composition of Protective Films Formed on Iron and Stainless Steels

REFERENCE: Lumsden, J. B. and Staehle, R. W., "Composition of Protective Films Formed on Iron and Stainless Steels," *Surface Analysis Techniques for Metallurgical Applications, ASTM STP 596*, American Society for Testing and Materials, 1976, pp. 39-51.

ABSTRACT: The composition of passive films formed on austenitic stainless steels have been determined using Auger electron spectroscopy. The films were found to be enriched in chromium which is consistent with the understanding of the relative insolubility of chromium compared to that of iron and nickel. However, the films were depleted in both silicon and molybdenum which are thermodynamically more stable than chromium in the solutions used. Thus, it is not possible to rationalize the improved resistance to acid solutions and solutions containing chlorides obtained by the addition of silicon and molybdenum to stainless steels using a selective-dissolution-enrichment model.

KEY WORDS: spectroscopy, iron, stainless steels, protective coatings, chemical analysis

Metals owe their chemical integrity to the presence of thin layers of reaction products on the surface. The amount of protection afforded by these layers depends upon their insolubility, adherence, and defect structure. This film is sometimes called a passive film; a metal is said to be passive if it is thermodynamically unstable under the conditions to which it is exposed, but, nevertheless, corrodes at a very low rate.

Faraday [1]² was one of the first to investigate this phenomenon when he studied the corrosion of iron in nitric acid. He found that iron dissolves rapidly in dilute nitric acid; however, in concentrated nitric, where according to thermodynamics iron should also dissolve, the metal becomes stable and is unattacked. Figure 1 shows the attacked and

¹ Adjunct assistant professor and professor, respectively, Department of Metallurgical Engineering, The Ohio State University, Columbus, Ohio 43210.

² The italic numbers in brackets refer to the list of references appended to this paper.

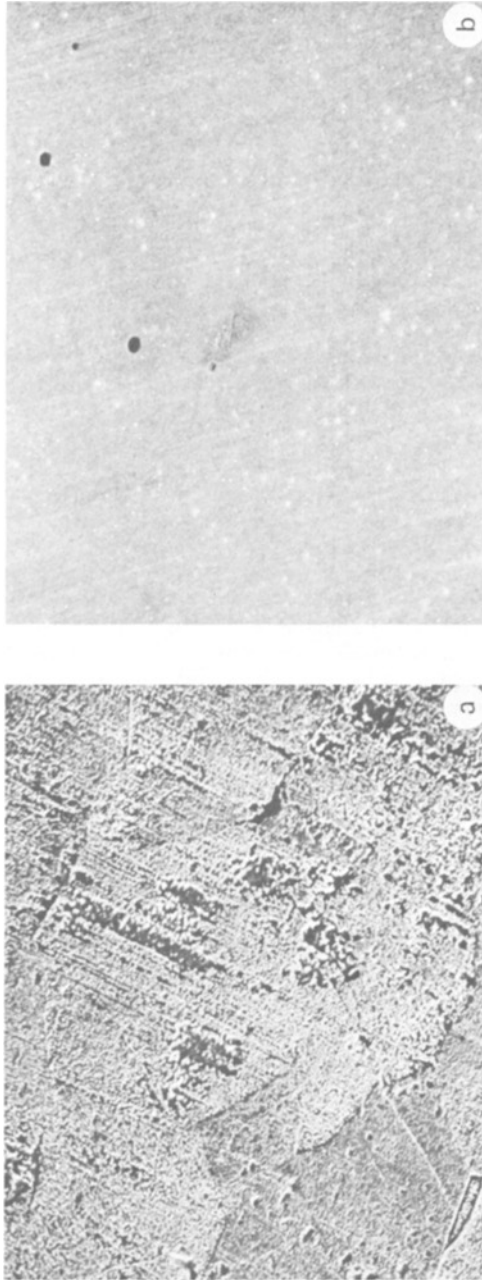


FIG. 1—Effects of dilute (a) and concentrated nitric acid (b) on iron.

unattacked surface of iron in dilute and concentrated nitric acid. The Auger electron spectroscopy (AES) analysis of these surfaces (Fig. 2) shows that in both cases the product layer film has the same composition, thus indicating the complexity of the phenomenon.

This work is particularly concerned with rationalizing the role of alloy species with respect to their critical influences on the protective quality of the films on stainless steel. Alloying iron with chromium and nickel to form austenitic stainless steel renders it passive under a wide range of environmental conditions including dilute nitric acid solutions. The addition of silicon and molybdenum produces a further resistance to attack in acid solutions and a substantial improvement in resistance to pitting in chloride containing environments [2,3].

For the various alloying elements to exert a significant effect, presumably they should be associated with the protective film. Rhodin [3-5] determined film compositions by chemical analysis of the isolated film. He used a film stripping procedure in which an aggressive reagent (an anhydrous methanol-bromine solution) was employed to attack the metal and float the film away. The improved corrosion behavior of stainless steels was found to correlate with the enrichment of silicon and molybdenum in the surface films.

The technique utilized here to obtain film compositions is AES, which permits the relative amounts of chemical species in the surface layers to be determined. Barnes et al [6] have used AES to determine the surface

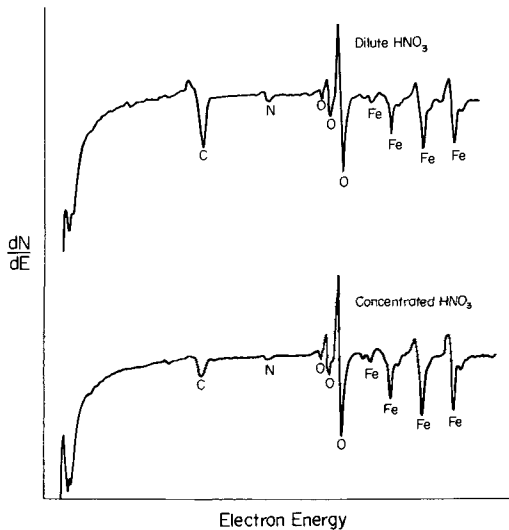


FIG. 2—Auger electron spectroscopy spectra from the attacked and unattacked iron surfaces on Fig. 1.

composition of stainless steels containing molybdenum. It was found in these studies that mill processing (the exact nature of the surface treatment was unknown) produced a surface concentration of molybdenum which was a factor seven larger than that of the bulk. In contrast, the study reported herein considers the formation of films resulting from exposure to aqueous environments.

Experimental

The alloys used were the austenitic stainless steels AISI Types 304, 316, 347, and a duPont experimental alloy, SP-2, which is a silicon modified Type 316L stainless steel. Compositions are given in Table 1.

The specimens were first vacuum annealed and then metallographically polished down to $0.3 \mu\text{m}$ and passivated. One passivation procedure was identical to that used by Rhodin. It consisted of first pickling the specimens in 10 percent nitric acid (HNO_3)-2 percent hydrofluoric acid (HF)-1 percent hydrochloric acid (HCl) at 80°C for 1 min. After rinsing the specimens in demineralized double distilled water, the passive films were formed by treating the pickled surface in 5 percent HNO_3 -0.5 percent potassium dichromate ($\text{K}_2\text{Cr}_2\text{O}_7$) at 60°C for 30 min. In order to examine the effect of the dichromate ion on the protective film, the specimens were also passivated by immersion in the 5 percent HNO_3 solution without the $\text{K}_2\text{Cr}_2\text{O}_7$.

In order to examine the influence of chloride ions, passive films were formed potentiostatically in a pH 7, 1.0 M sodium chloride (NaCl) + 0.1 M sodium sulfate (Na_2SO_4) solution. After mechanical polishing, the specimens were reduced cathodically and then polarized at 0 mV against the saturated calomel electrode (SCE). The solution was open to the air.

Comprehensive reviews of AES have been given elsewhere [7,8]; therefore, this technique will not be discussed here. The AES spectra were taken using a cylindrical mirror analyzer with a coaxial electron gun. A 2 keV, 50 μA electron beam was used having a diameter of approximately 50 Å. The modulation amplitude was 2 V peak to peak, and a frequency of 17 kHz was used.

The composition profiles of the passive films were obtained by the sequential application of sputtering by argon ion bombardment and AES analysis [9]. Ions of 600 eV energy and current densities in the 10^{-6} A/cm^2 range were used. The estimated sputtering rate was 2 to 4 Å/min. A base pressure of 8×10^{-10} torr or less was always used. A typical spectrum is shown in Fig. 3.

Results

The AES results for the specimens passivated in the HNO_3 - $\text{K}_2\text{Cr}_2\text{O}_7$ solution are shown in Figs. 4, 5, 6, and 7. Peak-to-peak heights versus sputtering time are given for the silicon (92 eV), columbium (167 eV),

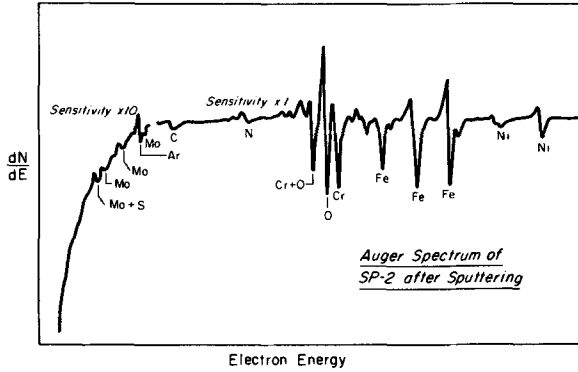


FIG. 3—Auger electron spectroscopy spectrum of passive film on Type SP-2 after sputtering.

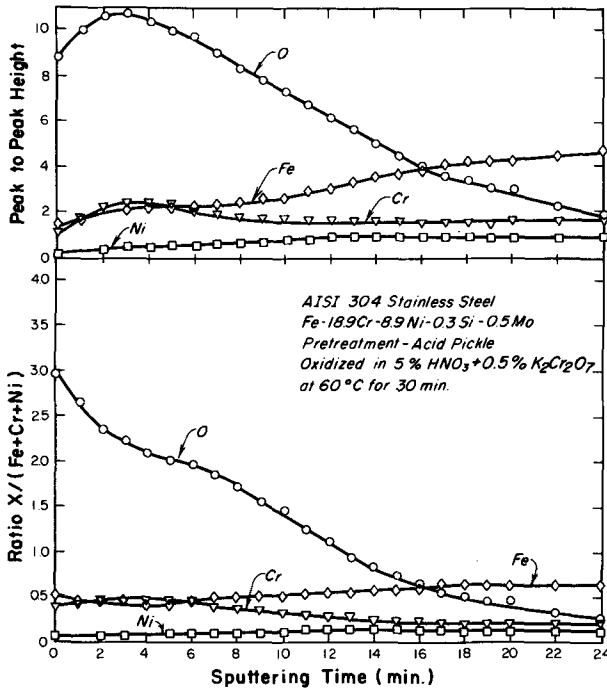


FIG. 4—Depth-composition profile of the film on Type 304 stainless steel passivated in a nitric acid-dichromate solution.

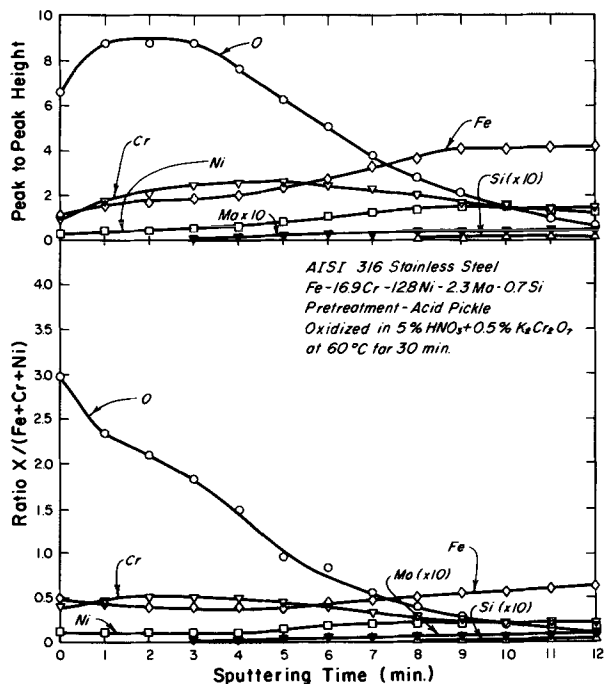


FIG. 5—Depth-composition profile of the film on Type 316 stainless steel passivated in a nitric acid-dichromate solution.

molybdenum (186 eV), oxygen (510 eV), chromium (529 eV), iron (703 eV), and nickel (848 eV) lines; also given are the normalized peak heights versus sputtering time, where the peak-to-peak heights of each of the above lines have been divided by the sum of the peak-to-peak heights for iron and nickel.

The results indicate that there was no enrichment of the molybdenum or silicon in the film. In fact, a depletion of these elements is observed. They were not detected in the surface or near surface layers of the films even at a sensitivity level ten times that used to obtain the remaining portion of the spectrum; likewise, there was no enrichment of columbium in the film on Type 347. This too was not detected until the metal substrate was

TABLE 1—Composition of stainless steel alloys, percent.

	Cr	Ni	Si	Mo	Cb
Type 304	18.9	8.8	0.33	0.46	...
Type 316	16.9	12.8	0.66	2.3	...
Type 347	18.7	11.0	0.41	...	0.59
Type SP-2	18.8	9.2	2.5	2.4	...

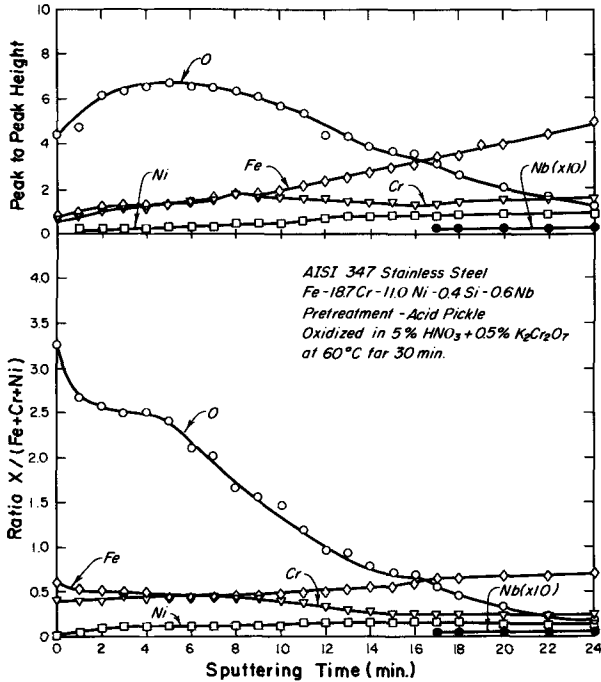


FIG. 6—Depth-composition profile of the film on Type 347 stainless steel passivated in a nitric acid-dichromate solution.

approached. The results also show that there was a substantial enrichment of chromium in the films. The peak-to-peak heights of the chromium line is greater than that of iron at several points within the films on all four alloys. Comparing the ratio of the normalized iron peak amplitude to chromium at the maximum chromium level in the film with the same ratio at the last point of the profile, an "enrichment factor" can be defined. This factor has the value of 3.5, 3.5, 3.2, and 3.3 for Types 304, 316, 347, and SP-2, respectively. The normalized nickel line changes little throughout the profile.

The compositions of the films formed in the 5 percent HNO₃ solution without the dichromate ions are shown in Figs. 8, 9, 10, and 11. These results are very similar to the previous ones. The differences are that the chromium enrichment was somewhat less and the normalized oxygen peak heights are also less. The enrichment factors in this case are 2.7, 2.7, 2.4, and 2.8 for Types 304, 316, 347, and SP-2, respectively. But here again no enrichment of molybdenum nor silicon was observed in the films, and the surface layers were depleted of these elements.

Figure 12 shows the current density-potential curve for Types 304, 316, and SP-2 in the sulfate-chloride (SO₄⁼-Cl⁻) solution. This shows the increase in the range of stability as the molybdenum and silicon contents

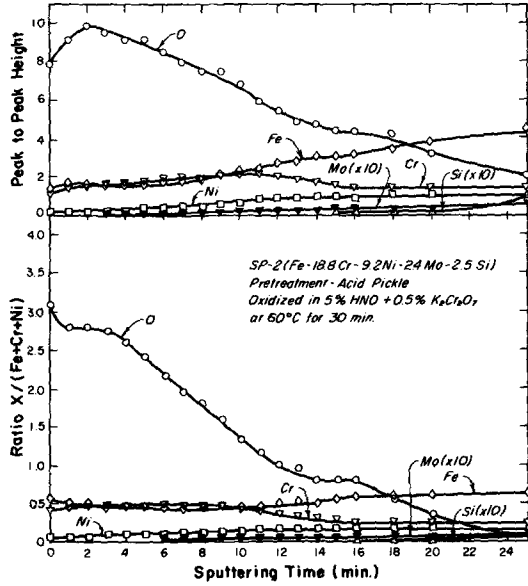


FIG. 7—Depth-composition profile of the film on Type SP-2 stainless steel passivated in a nitric acid-dichromate solution.

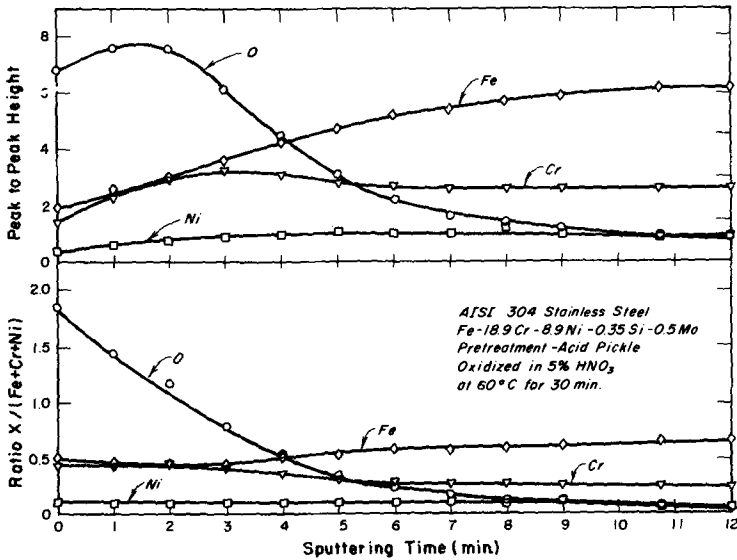


FIG. 8—Depth-composition profile of the film on Type 304 stainless steel passivated in nitric acid.

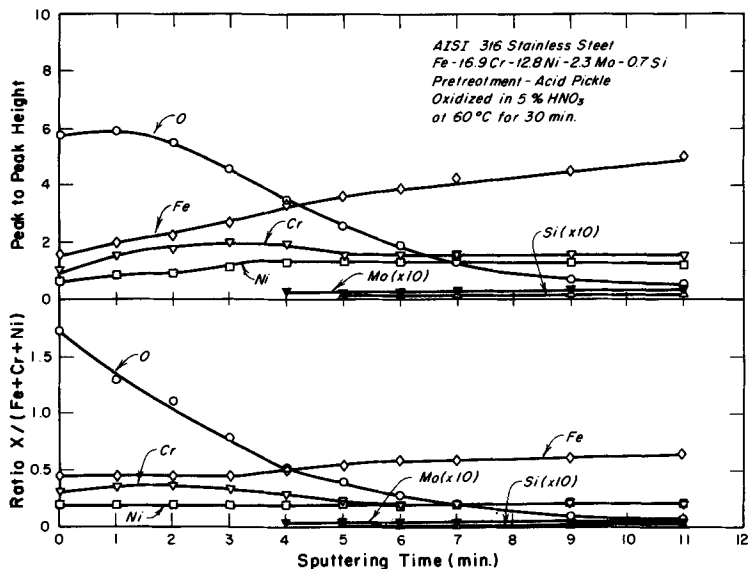


FIG. 9—Depth-composition profile of the film on Type 316 stainless steel passivated in nitric acid.

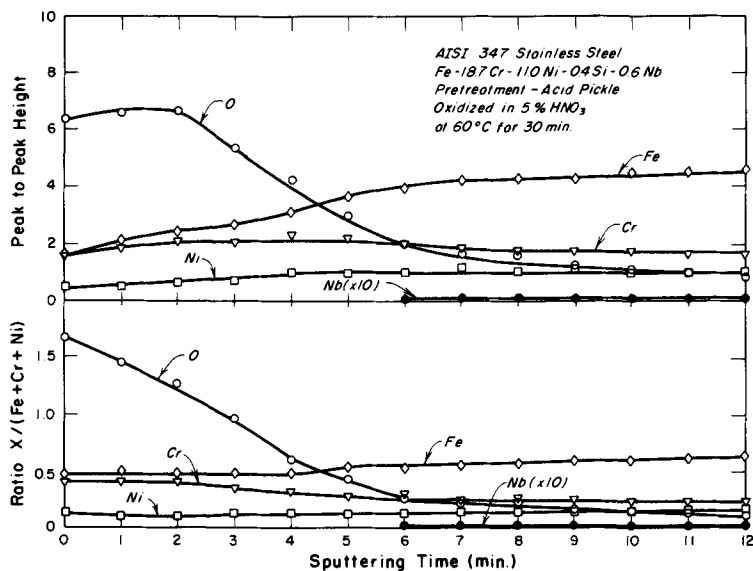


FIG. 10—Depth-composition profile on the film on Type 347 stainless steel passivated in nitric acid.

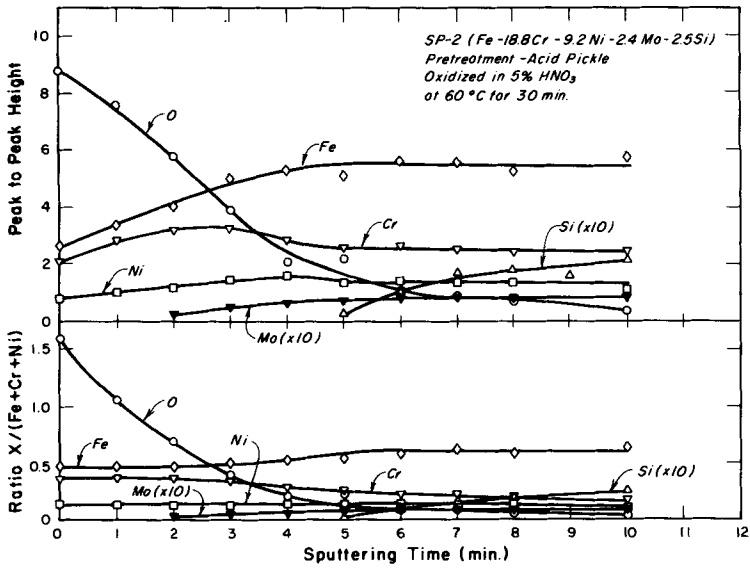


FIG. 11—Depth-composition profile of the film on Type SP-2 stainless steel passivated in nitric acid.

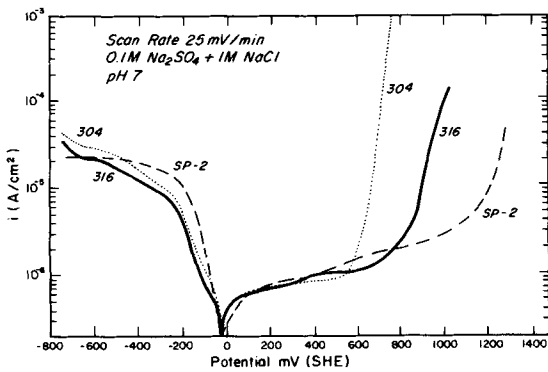


FIG. 12—Current density-potential curve for Types 304, 316, and SP-2 stainless steels exposed to a sulfate-chloride solution.

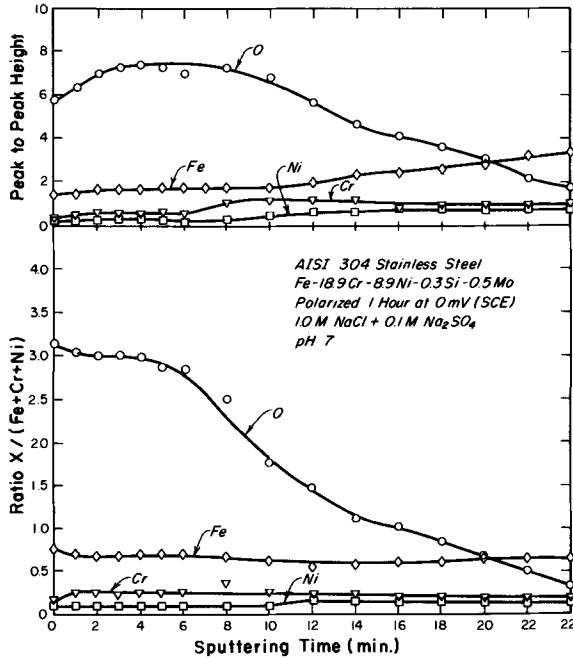


FIG. 13—Depth-composition profile of the film on Type 304 stainless steel passivated by potentiostatic polarization in a sulfate-chloride solution.

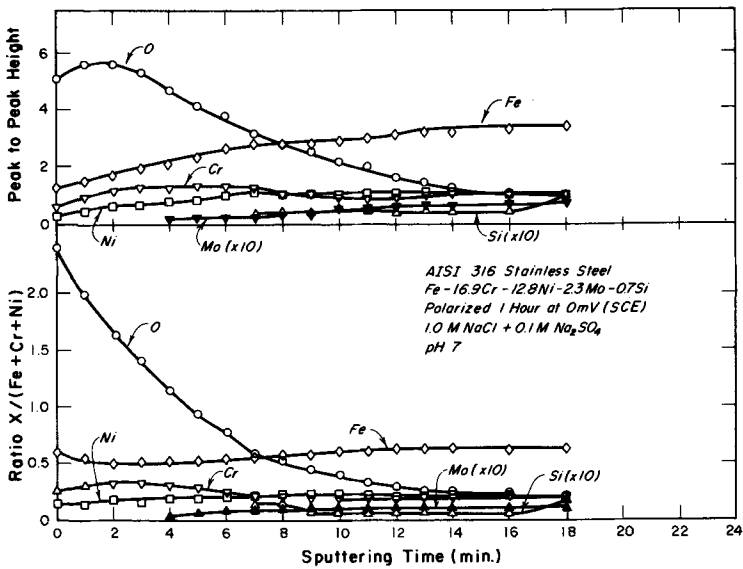


FIG. 14—Depth-composition profile of the film on Type 316 stainless steel passivated by potentiostatic polarization in a sulfate-chloride solution.

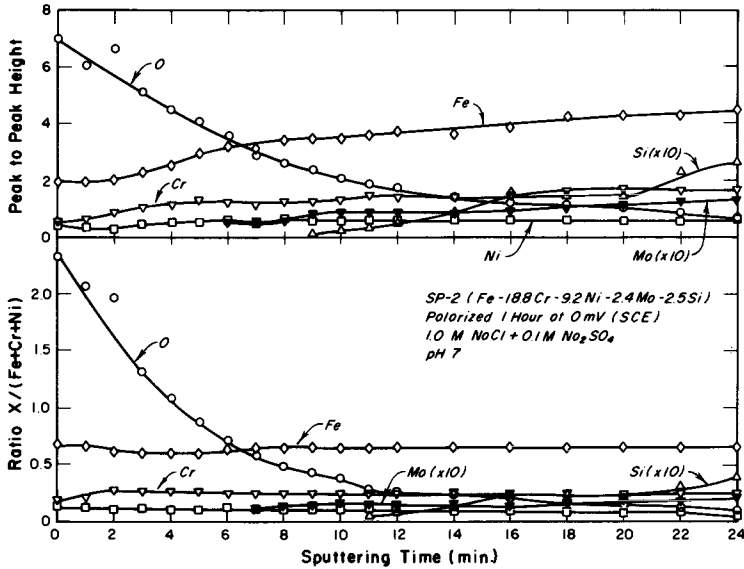


FIG. 15—Depth-composition profile of the film on Type SP-2 stainless steel passivated by potentiostatic polarization in a sulfate-chloride solution.

are increased. The AES results for the films formed in this solution are given in Figs. 13, 14, and 15. Only a slight enrichment of chromium is observed in the film on Type 304. The compositional behavior of silicon and molybdenum is identical to those observed in the previous two cases.

Discussion

The following are significant observations made using AES to analyze passive films on stainless steels.

1. There appears to be no enrichment of molybdenum or silicon in the surface film.
2. Chromium is enriched in the surface layers of the protective films which result from passivation in HNO_3 and HNO_3 plus $\text{K}_2\text{Cr}_2\text{O}_7$ solutions.
3. There is little, if any, chromium enrichment in films formed potentiostatically in a pH 7 $\text{SO}_4^{2-}\text{-Cl}^-$ solution.
4. The normalized nickel content remains essentially constant through the film.
5. The films formed by electrochemical polarization and in the HNO_3 solution containing the dichromate ion appear to have higher oxygen levels than those films formed in the HNO_3 solution without the dichromate ion.

The enrichment of chromium is consistent with the understanding of the

relative insolubility of chromium compared to that of iron and nickel in these environments and has been predicted in previous studies [10]; however, these results cannot be explained simply from thermodynamic considerations since silicon and molybdenum are both more stable than chromium at low pH's and these elements do not enrich in the film.

These results are substantially different from those obtained by Rhodin using a chemical analysis technique. He found a factor of 10 enrichment in silicon compared to the percentage in the alloy. In the case of molybdenum, he found an enrichment ranging from approximately 2 for Type 316 to slightly more than 10 for Type SP-2. He further found that the enrichment of silicon and molybdenum in the film corresponded to a depletion of iron. No enrichment of chromium was observed. In the case of Type 347, columbium enriched in the film by a factor of nine. None of these phenomena were observed using AES to determine film composition. Also the higher chromium levels found after passivation in the dichromate solutions could explain the increased improvement in pitting resistance following the treatment compared to that for alloys passivated in HNO₃ solutions without dichromate ions [3].

Considering the compositions of the films on Type 316 and SP-2, one must be concerned about the role of molybdenum and silicon since they do have a major influence on suppressing the pitting behavior; however, the AES analysis of these films gives no evidence that molybdenum and silicon are present to any substantial extent in the films on Type 316 and SP-2. Indeed, these elements are depleted in the outer layers of the film; therefore, it appears one must look in other directions for rationalizing the role of molybdenum and silicon.

Acknowledgments

The authors gratefully acknowledge support from the National Science Foundation, Grant No. DMR74-08061.

References

- [1] Faraday, M., *Philosophical Magazine*, Vol. 9, 1836, pp. 57, 122, 153.
- [2] Streicher, M. A., *Journal of the Electrochemical Society*, Vol. 103, 1956, p. 375.
- [3] Nielsen, N. A. and Rhodin, T. M., *Zeitschrift für Elektrochemie*, Vol. 62, 1958, p. 707.
- [4] Rhodin, T. N., *Corrosion*, Vol. 11, 1956, p. 465t.
- [5] Rhodin, T. N., *Corrosion*, Vol. 12, 1956, p. 123t.
- [6] Barnes, G. J., Aldag, A. W., and Jerner, R. C., *Journal of the Electrochemical Society*, Vol. 116, 1972, p. 684.
- [7] Chang, C. C., *Surface Science*, Vol. 25, 1971, p. 53.
- [8] Palmberg, P. W. in *Electron Spectroscopy*, D. A. Shirley, Ed., North-Holland, Amsterdam, 1972.
- [9] Palmberg, P. W., *Journal of Vacuum Science and Technology*, Vol. 9, 1972, p. 160.
- [10] Evans, U. R., *Research*, Vol. 6, 1953, p. 130.

L. E. Davis¹ and A. Joshi¹

Quantitative Auger Electron Spectroscopy with Elemental Sensitivity Factors

REFERENCE: Davis, L. E. and Joshi, A., "Quantitative Auger Electron Spectroscopy with Elemental Sensitivity Factors," *Surface Analysis Techniques for Metallurgical Applications*, ASTM STP 596, American Society for Testing and Materials, 1976, pp. 52-57.

ABSTRACT: An ultrahigh vacuum scanning Auger microprobe (SAM) system was used to obtain elemental sensitivity factors from selected metal alloys and oxides. The specimens were prepared to establish surface compositions equivalent to bulk concentration levels. Two-dimensional surface topographical and compositional SAM studies were made to determine the extent of impurity segregation or precipitation. Relative elemental sensitivity factors computed from published data were applied to ductile fracture surface measurements of Inconel and stainless steels. The metal alloy surface concentrations were compared to bulk concentrations. Relative elemental sensitivity factors were obtained from abraded surfaces of magnesium oxide, aluminum oxide, and silicon dioxide at primary beam energies of 3, 5, and 10 keV. The results from fractured and abraded standards were compared to measurements made after sputtering with argon ions.

KEY WORDS: spectroscopy, sensitivity, stainless steels, oxides, Auger electrons, fractures (materials), sputtering

In applications of Auger electron spectroscopy (AES) to practical problem solving it is often sufficient to identify the elemental components at the surface or interface. For example, AES measurements have shown that relative amounts of surface impurities can be related directly to good or poor bonding on integrated circuits [1].² A major portion of AES utilization, no doubt, will continue to be qualitative analysis. In the evaluation of new processes and chemical characterization of new materials, however, it is important to improve the quantitative capabilities of AES.

¹ Director and assistant director, respectively, Analytical Laboratory, Physical Electronics Industries, Eden Prairie, Minn. 55343.

² The italic numbers in brackets refer to the list of references appended to this paper.

A very practical method for quantitative analysis involved the use of elemental sensitivity factors. Assuming that the density of element x is uniform over the excitation volume (created by a primary electron beam of current I_p and energy E_p), the atomic concentration, C_x , may be described as [2,3]

$$C_x = I_x S_x^{-1} / (\sum_i I_i S_i^{-1}) \quad (1)$$

where I_x is the Auger electron peak-to-peak height for a specific Auger transition, and S_x is a relative elemental sensitivity factor. The summation extends over all elements in the matrix. In Eq 1, S_x depends on the matrix through its effect on the electron escape depth, backscattering factor, and Auger peak shape. The latter effect is important when the Auger current is measured as the peak-to-peak amplitude in the conventional $dN(E)/dE$ spectrum. The accuracy of Eq 1 is best for materials in which the matrix effect is similar to those materials used to obtain the elemental sensitivity factors.

In this paper, techniques will be described for the measurement of relative elemental sensitivity factors from standard materials. The applicability of Eq 1 will be tested by determining atomic concentrations of metal alloys with known bulk composition. Finally, measurements of oxide standards will be compared to elemental standards.

Experimental Procedure

The experiments were performed in an ultrahigh vacuum system capable of reaching pressures less than 10^{-10} torr. The experimental arrangement which has been described elsewhere [4] included a scanning Auger microprobe (SAM) [5], a 2-keV ion gun for argon sputter etching, a fracture attachment, and a diamond scribe.

The Auger electron signal was measured as the derivative of the electron energy distribution [$dN(E)/dE$] [6]. Relative elemental sensitivity factors were obtained from Auger electron peak-to-peak height measurements of the prepared standards [7]. The cylindrical mirror analyzer (CMA) used in this study had the same instrumental energy resolution (approximately 0.6 percent) as the CMA used to obtain the standardized spectra published elsewhere [8]. It should be emphasized that the relative sensitivity factors reported here are appropriate only for measurements made with energy analyzers of the same design.

The metal alloy standards were homogenized at high temperatures and then quenched. The specimens were then fractured *in situ* at room temperature, and the ductile fracture surfaces were examined by SAM elemental imaging to verify the uniformity of the surface chemistry. The elemental uniformity was examined over a 200 by 200- μm area with an electron beam diameter of 25 μm or less. Once surface uniformity was

assured, Auger electron spectra at several primary beam energies were obtained at pressures of 10^{-10} torr or less. Sensitivity factors were computed from published data [8] and applied to measured Auger electron peak heights to obtain atomic concentration levels in the manner described in Eq 1. The elemental sensitivity factors were relative (that is, $S_x = I_x/I_{Ag}$) to the $M_{45}VV$ transition of pure silver with $S_{Ag} = 1.00$. The computed surface concentrations were then compared to known bulk concentrations. After the surface measurements were completed, the standards were sputtered to test for differential sputtering effects.

Similar measurements were performed on oxides after abrasion of the surface with a diamond scribe as described by Farber and Braun [9]. After scribing, the $dN(E)/dE$ peak-to-peak heights were compared to a standard silver spectrum. Sensitivity factors were then computed from Eq 1 with $S_{Ag} = 1.00$. Here it was important to make the measurements at low electron beam current densities. As an example of electron beam reduction of an oxide surface, Fig. 1 shows the Auger peak heights of aluminum and oxygen as a function of time. In the first 5 min, while sputtering, the data points were representative of stoichiometric sapphire. When the ion beam was turned off, the oxygen signal decreased relative to the aluminum. Subsequent measurements showed that by reducing current densities below 10^{-4} A/cm², oxygen and aluminum signals remained constant for periods greater than 600 s.

Results and Discussion

Figure 2 is a spectrum obtained from the ductile fracture surface of an Inconel standard. The only impurity detected on the surface was carbon. In this case, the peak-to-peak heights of LMM Auger transitions were assigned sensitivity factors from published data [8] to obtain atomic concentration values. The sensitivity factors were obtained from pure

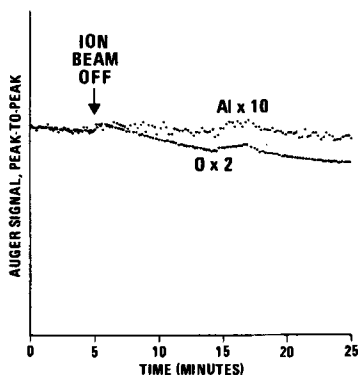


FIG. 1—Electron beam fragmentation of sapphire. (Electron beam current density $>10^{-3}$ A/cm².)

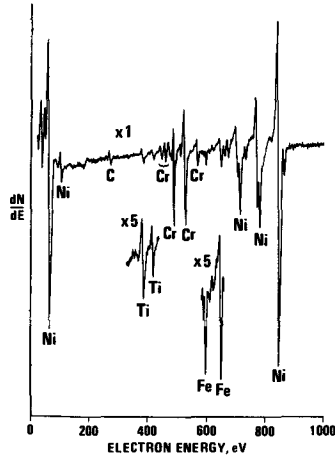


FIG. 2—Auger electron spectrum of the ductile fracture surface of Inconel.

elemental standards relative to clean silver. The calculated concentrations for Inconel and Types 304 and 316 stainless steels are listed in Table 1. As shown, surface concentrations agree well with bulk concentrations, even after sputtering. In this case, the specimens were sputtered with 1 and 2-keV argon ions until the peak-to-peak heights of all elements were constant. The results indicate that relative sensitivity factors obtained from elemental standards are appropriate for determining atomic concentrations of metal alloys.

The relative elemental sensitivity factors in Table 2 were obtained from abraded surfaces of magnesium oxide (MgO), aluminum oxide (Al_2O_3), and silicon dioxide (SiO_2). The sensitivity factors for KLL transitions were computed from Eq 1 and compared to elemental magnesium, aluminum, and silicon sensitivity factors [8]. No relative changes in the signals were observed after sputtering with 1 and 2-keV argon ions. In view of the possible electron beam charging and fragmentation effects, the variation in the oxygen sensitivity factor for the three oxides is within experimental error. These results imply that S_0 is not strongly dependent on matrix, and, thus, Eq 1 is applicable for determining oxygen concentrations in oxides of uniform composition with an uncertainty of ± 20 percent.

Table 2 also shows that the relative sensitivity factors for the magnesium, aluminum, and silicon KLL Auger transitions in the oxide state were larger than sensitivity factors for pure elemental standards. In this case, the $dN(E)/dE$ peak-to-peak height is not representative of the Auger current because these peaks broaden with oxidation. Since backscattering is not expected to affect significantly the magnitude of the Auger electron

TABLE 1—Calculated concentration levels of ductile fracture alloys.

Alloy	Element, x	S_x^a	Atomic Concentration		
			Bulk	Surface	After Sputtering
Type 304 stainless steel	Cr	0.31	0.205	0.24	0.23
	Fe	0.21	0.702	0.68	0.67
	Ni	0.26	0.093	0.09	0.10
Type 316 stainless steel	Cr	0.31	0.200	0.18	0.22
	Fe	0.21	0.656	0.71	0.67
	Ni	0.26	0.127	0.10	0.10
	Mo	0.25	0.018	0.01	0.02
600T Inconel	Cr	0.31	0.177	0.20	0.21
	Fe	0.21	0.084	0.07	0.07
	Ni	0.26	0.736	0.72	0.71
	Ti	0.44	0.003	0.01	0.01

^a Relative elemental sensitivity factors S_x obtained from Ref 8.

current for these oxides [2,10] these results suggest that the electron escape depths are larger in the oxides than in the pure elements.

Double integration of the $dN(E)/dE$ Auger electron signal has been shown to be a more accurate measurement of the Auger electron current when the Auger peak changes shape with chemical matrix [11]. A recent study by Gerlach and Hedtke³ has shown that columbium double integral amplitudes corrected for atomic density are approximately a factor of two larger in columbium pentoxide than in pure columbium. Since backscattering is expected to increase the Auger electron yield within the metal [10], this discrepancy again is explainable only in terms of larger electron escape depths within the oxide.

Summary

Metal alloy surface concentrations determined from relative elemental sensitivity factors in the manner described in Eq 1 have been shown to be in good agreement with bulk concentrations. In alloys that fracture by cleavage (for example, some body centered cubic and hexagonal close packed alloys) this technique of analysis of fracture surfaces can be used to obtain relative sensitivity factors. The surface composition of the fracture surface did not alter considerably by sputtering with 1 and 2-keV argon ions.

Elemental sensitivity factors were obtained for oxides by scribing the surface. Within experimental error (± 20 percent), relative elemental sensitivity factors obtained for oxygen indicate that Eq 1 can be used to

³ Gerlach, R. L. and Hedtke, R., Physical Electronics Industries, Inc., Eden Prairie, Minn., private communication.

TABLE 2—Elemental sensitivity factors of oxides relative to pure silver ($S_{Ag} = 1.0$).

Element, x	Standard	Peak Energy, eV	S_x		
			$E_p = 3$ keV	$E_p = 5$ keV	$E_p = 10$ keV
Magnesium	Mg0	1180	0.13	0.18	0.16
	Mg	1186	0.10
Aluminum	Al ₂ O ₃	1390	0.11	0.17	0.20
	Al	1396	0.039
Silicon	SiO ₂	1610	0.038
	Si	1619	0.011
Oxygen	Mg0	505	0.47	0.46	0.34
	Al ₂ O ₃	505	0.39	0.40	0.36
	SiO ₂	505	0.32

determine oxygen concentrations in oxides of uniform composition. The higher values of oxide sensitivity factors for magnesium, aluminum, and silicon KLL Auger transitions are believed to be due to larger escape depths of Auger electrons in the oxides compared to pure elements.

Acknowledgments

The authors gratefully acknowledge the technical assistance of J. F. Moulder, D. P. Nelson, and D. F. Paul. We also express gratitude to P. W. Palmberg, G. E. Riach, N. C. MacDonald, and R. L. Gerlach for helpful discussions and criticisms of this work. Special thanks are given to R. Hedtke and R. L. Gerlach who made unpublished results available to us.

References

- [1] MacDonald, N. C. and Riach, G. E., *Electron Packaging and Production*, April, 1973, p. 50.
- [2] Palmberg, P. W., *Analytical Chemistry*, Vol. 45, 1973, p. 549A.
- [3] Chang, C. C. in *Characterization of Solid Surfaces*, P. F. Kane and G. B. Larrabee, Eds. Plenum Press, 1974, p. 509.
- [4] Weber, R. E., *Research/Development*, Vol. 23, 1972, p. 22.
- [5] MacDonald, N. C., *Electron Microscopy: Physical Aspects*, D. Beaman and B. Siegal, Eds. Wiley, New York, 1974.
- [6] Weber, R. E. and Peria, W. T., *Journal of Applied Physics*, Vol. 38 1967, p. 4355.
- [7] Weber, R. E. and Johnson, A. L., *Journal of Applied Physics*, Vol. 40, 1969, p. 317.
- [8] Palmberg, P. W., Riach, G. E., Weber, R. E., and MacDonald, N. C., "Handbook of Auger Electron Spectroscopy," Physical Electronics Industries, Inc., 1972.
- [9] Farber, W. and Braun, P., to be published in *Vakuum Technik*.
- [10] Targ, M. L. and Wehner, G. K., *Journal of Applied Physics*, Vol. 44, 1973, p. 1534.
- [11] Grant, J. T., Haas, T. W., and Houston, J. E., *Journal of Vacuum Science and Technology*, Vol. 11, 1974, p. 227.

J. M. Walsh¹ and N. P. Anderson¹

Application of Auger Electron Spectroscopy to the Study of Embrittlement in Nickel

REFERENCE: Walsh, J. M. and Anderson, N. P., "Application of Auger Electron Spectroscopy to the Study of Embrittlement in Nickel," *Surface Analysis Techniques for Metallurgical Applications, ASTM STP 596*, American Society for Testing and Materials, 1976, pp. 58-67.

ABSTRACT: Auger electron spectroscopy (AES) was performed on a series of impurity-doped nickel specimens in order to clarify the nature of certain trace element effects that lead to a reduction in the mechanical properties of nickel and nickel-base alloys. Auger electron spectroscopy of the fully embrittled as-cast material showed grain boundary segregation of sulfur, bismuth, and tellurium in order of decreasing intensity when the bulk levels were as low as 40, 10, and 25 ppm weight, respectively. No segregation of lead, antimony, tin, arsenic, or copper could be detected at the grain boundaries. The observed segregation was confined to a very narrow zone in the vicinity of the grain boundary, and since no precipitates could be found by scanning or transmission electron microscopy, it is suggested that the embrittled condition is due to segregation in the elemental form. The data correlate with previous work on nickel alloys that shows bismuth and tellurium to have a more harmful effect on the mechanical properties than the other metallic solutes.

KEY WORDS: spectroscopy, Auger electrons, surface chemistry, sputtering, mechanical properties, fractures (materials), embrittlement, segregation, grain boundaries, impurities, solubility, solutes, nickel alloys, sulfur, bismuth, tellurium, lead, antimony, tin, arsenic, copper

Although it is well known that trace quantities of certain elements have deleterious effects on the mechanical properties of nickel and nickel-base alloys [1-3],² the mechanism by which this occurs is not well understood. It is commonly believed that embrittlement is due to a buildup of the trace elements at grain boundaries whether it be in the form of a submicroscopic

¹ Assistant materials project engineer and senior materials engineer, respectively, Pratt and Whitney Aircraft, Materials Engineering and Research Laboratory, East Hartford, Conn. 06108.

² The italic numbers in brackets refer to the list of references appended to this paper.

ically thin elemental film, a second phase precipitate, or simply an atomic segregation. Advances in the technique of Auger electron spectroscopy (AES) have made it possible to establish the nature of embrittlement in a number of systems including bismuth in copper [4,5], tin and antimony in iron [6,7], and phosphorus in tungsten [8]. This paper describes the application of the AES technique to a series of impurity doped nickel specimens in an effort to clarify the nature of certain trace element effects.

Procedure

Three nickel heats were studied that were doped with the elements lead, bismuth, tellurium, antimony, tin, arsenic, and copper up to bulk concentrations of approximately 25 ppm weight each. The alloys also contained up to 60 ppm weight sulfur and 270 ppm weight carbon. Bulk chemical analysis of the material is given in Table 1. Material was examined in the as-cast condition and after a heat treatment of 760°C/48 h. Specimens were fractured by impact in a baked ultrahigh vacuum system, and the fracture surface composition was determined by AES. Elemental concentration profiles were determined as a function of distance from the fracture by sequential and in some cases simultaneous argon ion sputtering and AES. Fracture surfaces were also characterized in a scanning electron microscope. Thin foils were prepared from the specimens and examined in a transmission electron microscope for evidence of grain boundary phases.

Results

All three alloys were fully embrittled in the as-cast condition and provided completely intergranular fracture surfaces (Fig. 1); therefore, the observations made by AES are regarded as being representative of the grain boundary condition. The AES results are summarized in Table 2 and typical spectra are shown in Fig. 2. Clear evidence was obtained for grain

TABLE 1—*Bulk chemical analysis of alloys.*

Element	Alloy 1, ppm weight	Alloy 2, ppm weight	Alloy 3, ppm weight
Bi	22	9	1
Te	26	8	1
Pb	26	8	1
Sb	21	8	1
Sn	24	9	2
As	30	10	10
Cu	15	15	15
S	50	60	40
C	65	210	270
Ni	balance	balance	balance

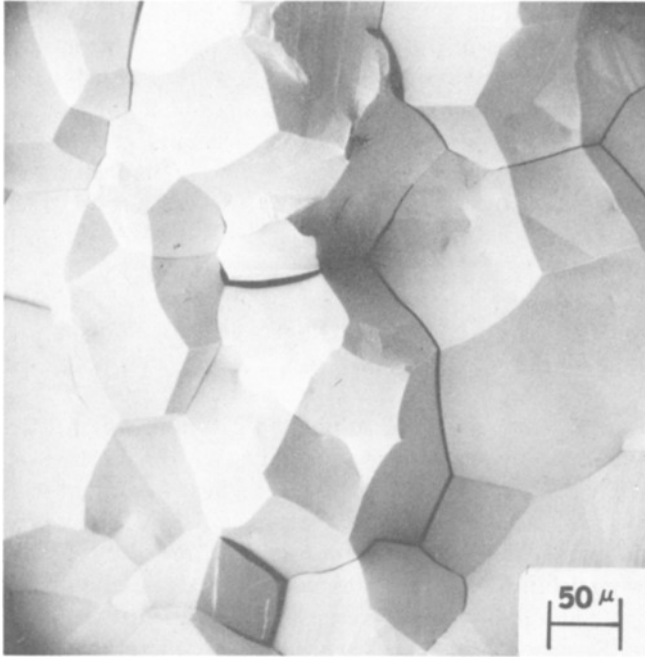


FIG. 1—Scanning electron micrograph of fracture surface of Alloy 1 in the as-cast condition showing intergranular character of fracture.

boundary segregation of bismuth, tellurium, sulfur, and in some cases carbon. The elements lead, antimony, tin, arsenic, and copper were not detected in the grain boundaries. Concentration versus depth profiles were then performed for the segregated elements and indicated that the solutes were segregated to a narrow region in the vicinity of the grain boundary. Typical sputter depth profiles are shown in Fig. 3. The sputter depth was estimated using the published sputtering yield data of Laegreid and Wehner [9] and represents only an upper limit on the thickness of the segregate as it has been shown [10] that surface active species sputter away at a slower rate than they would from their bulk. The surface topography of the fracture may affect the sputtering response in that a high point could shield a low point from the ion beam. If this effect were operative, it would also tend to overestimate the segregate thickness.

The material was then heat treated at 760°C/48 h, and although it was ductilized to some extent, predominantly intergranular fracture could still be achieved. The AES experiments were repeated and the data are summarized in Table 2. The segregation trends were similar to those observed in the as-cast material but the intensity or extent of the segregation was less.

No evidence for grain boundary precipitates or films could be found through scanning electron microscope examination of virgin fracture surfaces or transmission electron microscope examination of thin foils.

AES Composition Estimates

Two different methods were used to estimate AES compositions. The first approach was based on the peak to peak heights in the derivative spectra and the relative sensitivity of the Auger transitions for the pure elements through use of the familiar sensitivity relationship taken from Ref 11

$$C_x = \frac{I_x/S_x}{\sum_n I_n/S_n}$$

TABLE 2—Summary of AES observations.

Solute	Bulk Concentration, ppm weight	Condition	Estimated Fracture Surface Coverage, atomic percent
Bi	22	as cast	5
Bi	22	760°C/48 h	4.5
Bi	9	as cast	3
Bi	9	760°C/48 h	... ^a
Bi	1	as cast	nd
Bi	1	760°C/48 h	nd
Te	26	as cast	0.5
Te	26	760°C/48 h	nd
Te	8	as cast	nd
Te	8	760°C/48 h	... ^a
Te	1	as cast	nd
Te	1	760°C/48 h	nd
S	60	as cast	35.5
S	60	760°C/48 h	... ^a
S	50	as cast	28.5
S	50	760°C/48 h	16
S	40	as cast	21
S	40	760°C/48 h	4.5
C	270	as cast	7
C	270	760°C/48 h	16 ^b
C	210	as cast	nd
C	210	760°C/48 h	... ^a
C	65	as cast	nd
C	65	760°C/48 h	6

NOTE—nd = not detected by AES.

^a Specimen damaged.

^b Small oxygen peak observed.

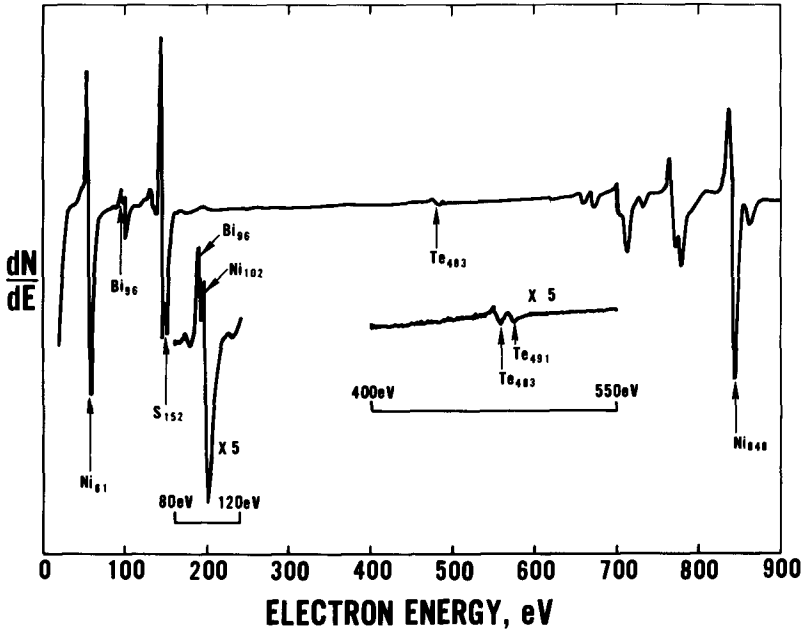


FIG. 2—Auger spectra of virgin fracture surface of Alloy 1 in the as-cast condition.

where

C_x = atomic concentration of element x ,

I_x = peak to peak Auger electron intensity of element x on the specimen,

S_x = peak to peak Auger electron intensity of element x measured on a pure element standard under identical experimental conditions,

and the summation is over one Auger transition of each of the n elements present in the surface.

This technique has been applied widely as a first approximation to composition using standard tabulated spectra measured under conditions of continuous sputtering [11]. Significant errors can result from this technique since no account is taken of: (a) change in peak shape from specimen to standard; (b) change in surface topography from specimen to standard; (c) difference in Auger electron excitation due to backscattering of primary electrons from specimen to standard; and (d) variations in sampling depth of different elements because of escape depth dependency upon Auger electron energy.

In the present study analytical lines and standards were selected that would tend to minimize these errors and are shown in Table 3. No sputtering was done while the standard spectra were being collected.

The second method, which gives the total solute concentration in the surface, is based on the attenuation of a surface sensitive Auger peak of the substrate material. The sputtering experiments indicated that the major solute buildup was within the first few atomic layers of material; therefore, the solvent atoms should be depleted in this region by a corresponding amount. Since the escape depth of Ni₆₁ Auger electrons is on the order of a few atomic layers [12], attenuation is the peak from the bulk to the virgin fracture might be used to estimate the total solute concentration in the top atomic layers as follows

total atom fraction of
all solutes in surface =

$$\frac{I_{Ni_{61}}(\text{bulk}) - I_{Ni_{61}}(\text{fracture surface})}{I_{Ni_{61}}(\text{bulk})}$$

Compositions estimated by the two methods for the three alloys in the as-cast condition (Table 4) showed good agreement. Precaution must be taken in applying the attenuation method for estimating surface solute concentration since any contamination of the surface with elements such as oxygen and carbon may have a large effect on the low energy peaks.

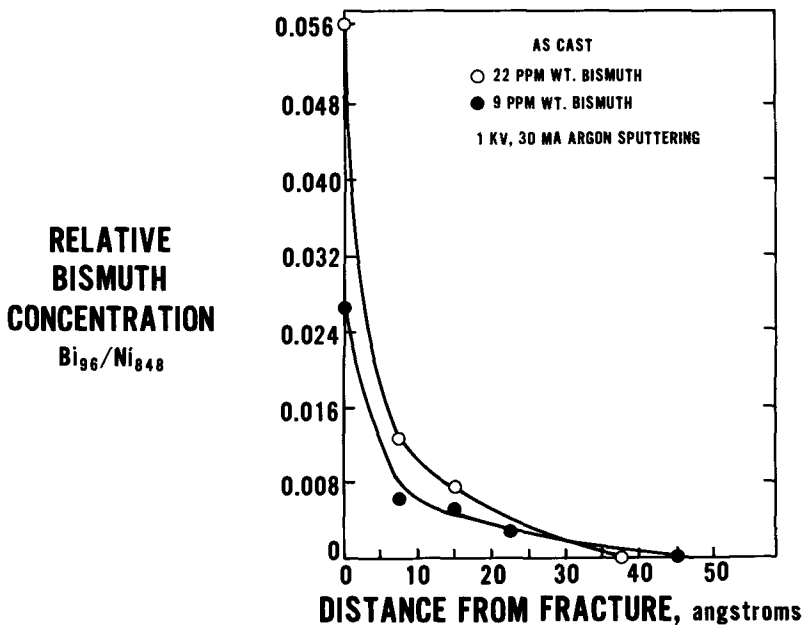


FIG. 3—Bismuth sputter-depth profiles for Alloys 1 and 2 in the as-cast condition.

TABLE 3—Auger calibration data.

Element	Auger Transition	Standard
S	152 eV	cleaved surface of FeS ₂ adjusted to 100% sulfur
Ni	61 eV	intergranular fracture surface of pure Ni (the standard used was one of the specimens after the segregated solute was sputter removed from the fracture surface)
Bi	96 eV	fractured surface of pure Bi
Te	483 eV	fractured surface of pure Te

Discussion

The segregation of sulfur to grain boundaries in nickel is well known [1,13,14] and has recently been confirmed by AES [15,16]. The results of the present investigation are in good agreement with these other studies. In nickel-base alloys it has been shown that this effect can be reduced or eliminated by the effective gettering of sulfur by elements such as manganese, hafnium, and titanium [1].

The other trace elements studied here are all known to have deleterious effects on the mechanical properties of nickel-base alloys [1-3]. In a recent study of trace element effects on creep-rupture properties of nickel-base alloys, Henricks and Gell [3] determined tolerance levels for a series of trace elements including those in the present study. They rated bismuth as the most damaging element, followed in order of decreasing harmfulness by tellurium and lead. A rather abrupt drop in the damage effect was noted between tellurium and lead while the elements antimony, tin, arsenic, and copper were far less damaging. The present AES result showing bismuth as the most strongly segregated metallic solute in the grain boundary followed by tellurium which had measurable but lower coverage tends to correlate with this observation. The elements lead, antimony, tin, arsenic, and copper could not be found at the grain boundaries indicating that they were below the Auger minimum detectability limit of ~0.5 to 1 atomic percent.

The fact that lead, antimony, tin, arsenic, and copper were not found at the grain boundaries might be explained on the basis of the fracture surface enrichment ratio which is simply the ratio of the fracture surface solute coverage to bulk solute concentration. This is similar to the grain boundary enrichment factor, β , defined by Hondros and Seah [6,17,18] as the ratio of grain boundary coverage to bulk solute concentration and used as a measure of interfacial activity. The fracture enrichment ratio

required for the fracture coverage to reach the AES detectability limit of ~ 0.5 to 1 atomic percent was calculated for these five elements from the bulk alloy composition of Alloy 1 (Table 5). The table shows that in order to get measurable AES signals for these elements when present at the bulk concentrations indicated it is necessary to have enrichment ratio values in the range of 200 to 1400. These values are near or greater than the very few experimental values of the same solutes in similar systems that we could find. So even though some of these elements may and probably do segregate, the bulk solute concentrations and actual enrichment ratios may not be sufficient to produce a grain boundary concentration measurable by AES.

In most cases the virgin fractures were free of the contaminants oxygen and carbon. Of the as-cast specimens, the only fracture showing carbon was the 270 ppm weight bulk carbon specimen (Alloy 3), and since it did not also show oxygen, it was felt that the carbon was present as a genuine segregation within the alloy.

The concentration of each of the metallic trace elements in the three alloys ranged from ~ 1 to 25 ppm weight while the sulfur concentration remained relatively constant (~ 40 to 60 ppm weight), and yet all three alloys were fully embrittled. Therefore, there is little doubt that the embrittlement in this experiment is due almost entirely to sulfur. The kind of embrittlement observed would imply grain boundary saturation. While the total estimated fracture surface solute coverage was 30 to 34 atomic percent, the actual grain boundary concentration may be much higher. The AES measurement represents an average analysis over the escape depth of the Auger electrons; however, the sputter-depth profiles suggest that only the top atomic layer is highly enriched in solute. Therefore, if the measured fracture surface concentration is adjusted to the top atomic layer and is then doubled to take into account the two halves of the

TABLE 4—Comparison of fracture surface solute concentration of as cast alloys determined by sensitivity method and substrate attenuation method.

Element	AES Fracture Surface Coverage, atomic percent		
	Alloy 1	Alloy 2	Alloy 3
Bi	5	3	...
Te	0.5
S	28.5	35.5	21
C	7
Total based on sensitivity method	34	38.5	28
Total based on Ni_{61} attenuation method	34	34	30

TABLE 5—Calculated fracture enrichment ratio for Alloy 1 required to give detectable AES indication.

Solute	Bulk Concentration, ppm weight	Enrichment Ratio ^a Required for Fracture Coverage to Reach AES Detectability Level of 0.5 to 1 atomic percent	Enrichment Ratio from Literature
Pb	26	700 to 1400	
Sb	21	500 to 1000	Sb in Fe, ~100 to 300 [19,20]
Sn	24	400 to 800	Sn in Fe, ~50 [17]
As	30	200 to 400	
Cu	15	350 to 700	

^a Enrichment ratio = fracture surface coverage/bulk solute concentration.

fracture, a coverage of roughly 1.3 monolayers is deduced at the common boundary between grains which is consistent with saturation.

Because of the large amount of sulfur measured on the fracture surfaces, consideration was given to the possibility of competition among solutes for surface sites. McLean [21] has discussed restriction in the grain boundary segregation of a solute due to prior occupancy of a given grain boundary site by a second species of solute. Aust et al [22] have also suggested that under certain conditions one solute may restrict the segregation of a second solute if it can reduce the binding energy of the segregating solute with a vacancy. Seah and Hondros [6] have recently demonstrated in a sulfur and tin doped iron alloy showing strong grain boundary segregation for both tin and sulfur that site competition between solutes does not occur but that, rather, each solute behaves as if the other were not present. A comparison of the segregation levels for sulfur and bismuth in the present study with previous studies suggests that site competition between sulfur and bismuth is not very strong. For example, Alloy 1 showed a fracture enrichment ratio for bismuth of ~8000, whereas Joshi [4] has shown in copper alloyed with only bismuth enrichment ratios of ~7000 to 15000. The observed sulfur enrichment for Alloy 1 was ~3100 while Johnson et al [16] showed values of ~1700 to 2500 for sulfur in a nickel-base alloy.

No evidence for a second phase precipitate could be found in the grain boundaries by SEM examination of virgin fractures or transmission electron microscopy and selected area electron diffraction of thin foils; therefore, the segregated solutes may be present in the grain boundary in the elemental form.

Conclusions

Bismuth, tellurium, and sulfur show strong segregation to grain boundaries in nickel when the bulk concentrations are as low as 10, 25, and 40

ppm weight, respectively. The solutes are confined to a narrow region in the vicinity of the grain boundary, probably in the elemental form. The sulfur segregation effects observed are in agreement with previous investigations. The extent of bismuth and tellurium segregation correlates with the damaging effects these elements have on the mechanical properties of nickel-base alloys. Evidence for grain boundary site competition between sulfur and bismuth was not found.

References

- [1] Bieber, C. G. and Decker, R. F., *Transactions, Metallurgical Society of American Institute of Mining, Metallurgical, and Petroleum Engineers*, Vol. 221, 1961, pp. 629-636.
- [2] Wood, D. R. and Cook, R. M., *Metallurgia*, March 1963, pp. 109-117.
- [3] Henricks, R. J. and Gell, M. L., "Trace Element Effects in Cast Nickel-Base Superalloys," American Society for Metals, Materials Engineering Congress, Chicago, Ill., 3 Oct. 1973.
- [4] Joshi, A. and Stein, D. F., *Journal, Institute of Metals*, Vol. 99, 1971, pp. 178-181.
- [5] Powell, B. D. and Mykura, H., *Acta Metallurgica*, Vol. 21, 1973, p. 1151-1156.
- [6] Seah, M. P. and Hondros, E. D., *Proceedings, Royal Society of London*, Vol. A-335, 1973, pp. 191-212.
- [7] Stein, D. F., Joshi, A., and Laforce, R. P., *Transactions, American Society for Metals*, Vol. 62, 1969, pp. 776-783.
- [8] Joshi, A. and Stein, D. F., *Metallurgical Transactions*, Vol. 1, 1970, pp. 2543-2546.
- [9] Laegreid, N. and Wehner, G. K., *Journal of Applied Physics*, Vol. 32, 1961, pp. 365-369.
- [10] Seah, M. P., *Journal of Physics, F, Metal Physics*, Vol. 3, 1973, pp. 1538-1547.
- [11] Palmberg, P. W., Riach, G. E., Weber, R. E., and MacDonald, N. C., *Handbook of Auger Electron Spectroscopy*, Physical Electronics Industries, Inc., 1972.
- [12] Palmberg, P. W., *Analytical Chemistry*, Vol. 45, 1973, pp. 549A-556A.
- [13] Merica, P. D. and Waltenberg, R. G., "Malleability and Metallography of Nickel," Technologic Papers of the National Bureau of Standards, Vol. 19, Paper 281, 2 April 1925, pp. 155-182.
- [14] Olsen, K. M., Larkin, C. F., and Schmitt, P. H., *Transactions, American Society for Metals*, Vol. 53, 1961, pp. 349-358.
- [15] Thompson, A. W. in *Grain Boundaries in Engineering Materials*, J. L. Walter, J. H. Westbrook, and D. A. Woodford, Eds., Claitor's Publishing Division, Baton Rouge, 1975, pp. 607-618.
- [16] Johnson, W. C., Doherty, J. E., Kear, B. H., and Giamei, A. F., *Scripta Metallurgica*, Vol. 8, 1974, pp. 971-974.
- [17] Hondros, E. D. and Seah, M. P., *Scripta Metallurgica*, Vol. 6, 1972, pp. 1007-1012.
- [18] Seah, M. P. and Hondros, E. D., *Scripta Metallurgica*, Vol. 7, 1973, pp. 735-738.
- [19] Smith, C. L. and Low, J. R., *Metallurgical Transactions*, Vol. 5, 1974, pp. 279-287.
- [20] Marcus, H. L. and Palmberg, P. W., *Transactions, Metallurgical Society of American Institute of Mining, Metallurgical, and Petroleum Engineers*, Vol. 245, 1969, pp. 1664-1666.
- [21] McLean, D. in *Grain Boundaries in Metals*, Clarendon Press, London, 1957, Chapter 5.
- [22] Aust, K. T., Hanneman, R. E., Niessen, P., and Westbrook, J. H., *Acta Metallurgica*, Vol. 16, 1968, pp. 291-302.

G. C. Nelson¹ and P. H. Holloway¹

Determination of the Low Temperature Diffusion of Chromium Through Gold Films by Ion Scattering Spectroscopy and Auger Electron Spectroscopy

REFERENCE: Nelson, G. C. and Holloway, P. H., "Determination of the Low Temperature Diffusion of Chromium Through Gold Films by Ion Scattering Spectroscopy and Auger Electron Spectroscopy," *Surface Analysis Techniques for Metallurgical Applications, ASTM STP 596*, American Society for Testing and Materials, 1976, pp. 68-78.

ABSTRACT: The transport of chromium through thin gold films has been characterized by ion scattering spectroscopy and Auger electron spectroscopy. The dominant transport path was shown to be grain boundaries in the gold films. The driving forces for transport were shown to be the reduction in the systems free energy associated both with the free energy of mixing and the free energy of formation of chromium oxide (Cr_2O_3). The kinetics of grain boundary diffusion were determined as a function of time and temperature. The grain boundary diffusion coefficient preexponential was determined to be $3.8 \times 10^{-3} \text{ cm}^2/\text{s}$ and the activation energy to be 26 kcal/mol.

KEY WORDS: spectroscopy, diffusion, chromium, gold, Auger electron spectroscopy, ion scattering spectroscopy

Due to the high reliability and long shelf life required by the microelectronics industry, it has become increasingly important to make diffusion measurements on thin film couples. These measurements have been carried out by a variety of techniques [1-6].² However, only recently have the surface sensitive analytical techniques such as ion scattering spectroscopy (ISS) [7], Auger electron spectroscopy (AES) [8], and photoelectron spectroscopy (ESCA) [9] been applied to this problem [10-12]. These techniques offer two methods for studying thin film diffusion. First,

¹ Members of the technical staff, Sandia Laboratories, Albuquerque, N. Mex. 87115.

² The italic numbers in brackets refer to the list of references appended to this paper.

by combining sputter profiling with these techniques, composition versus depth information can be obtained over very short distances. This can be particularly useful in obtaining bulk diffusion data in low temperature regions where device lifetime projections are required. Second, the surface sensitive techniques can be used to determine the surface composition of specimens which are heated *in situ* or have been externally heat treated. By measuring changes in the surface chemical composition as a function of time and temperature of heat treatment, the diffusion coefficient can be determined. This method eliminates the possible problems associated with sputtering over very long distances ($\approx 300 \text{ \AA}$) and is the method used for the present experiments.

The purpose of the present experiments was to demonstrate that ISS and AES can be applied in this manner to the analysis of thin film diffusion. In addition, the study relates to an important problem associated with Sandia Laboratories' hybrid microcircuit (HMC) technology, namely, the diffusion of chromium through gold films. Sandia's HMC technology is based on a polycrystalline alumina (Al_2O_3) substrate, a 500 \AA tantalum nitride thin film resistor layer, a 300 \AA chromium adhesion layer, and a 30 000 \AA gold conductor layer. This is shown schematically in Fig. 1. During processing the HMCs are heat treated at 300°C for 2 h in air. This heat treatment causes chromium to leave the adhesion layer, migrate through the gold film, and form sufficient chromium oxide (Cr_2O_3) on the gold surface to interfere with thermocompression bonding. Therefore, the kinetics of the transport of chromium to the surface of the gold films are important for the processing of these HMCs.

The present experiments sought to answer these questions. 1. What is the driving force for the chromium transport? 2. What are the diffusion paths? 3. What are the diffusion kinetics?

Experimental

Due to the high ($\sim 350^\circ\text{C}$) substrate temperature used during "production" deposition of the chromium and gold films, an initial unknown chromium distribution is present in the gold. This initial chromium distribution complicates the analysis of the experimental data. Therefore, the analysis of diffusion described in this paper was carried out on data obtained from specimens which were evaporated on glass microscope slides with particular care being taken to maintain a low substrate temperature ($< 50^\circ\text{C}$) during deposition to minimize diffusion. For these specimens the 475 \AA chromium layer and 3400 \AA gold layer were deposited at 100 $\text{\AA}/\text{min}$ from a resistively heated boat and 500 $\text{\AA}/\text{min}$ for an electron beam source, respectively. The system pressure was 2×10^{-7} torr before and 5×10^{-5} torr during deposition.

Auger electron spectroscopy was performed with a commercial spec-

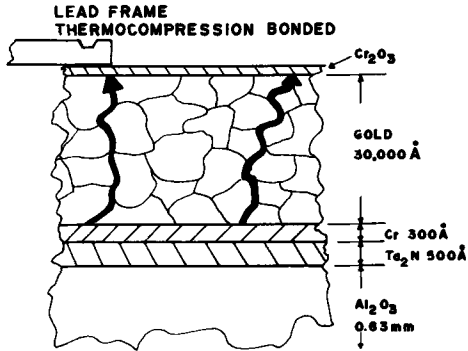


FIG. 1—Hybrid microcircuit geometry with Cr_2O_3 layer on the surface. The arrows indicate possible diffusion paths.

trometer using a cylindrical mirror analyzer and a coaxial electron gun. A 5 keV, 10 μA primary beam of electrons was used with a modulation of 4 V peak to peak. Specimens were mounted with their mean normal 60 deg off the analyzer axis. The chromium concentration was characterized by the area under a plot of the 529-eV peak height versus sputter time.

Ion scattering spectroscopy was performed in a modified commercial spectrometer. The primary beam was approximately 0.2 μA of 2500-eV neon ions. As with the AES, the surface chromium concentration was characterized by the area under a plot of the chromium signal intensity versus sputter time.

Film thicknesses were measured by etching steps and using a stylus profilometer. A muffle furnace was used to carry out the heat treatments in air. The furnace temperature was determined with a thermocouple spot welded to a typical substrate. Temperature variations during heat treatment were measured to be less than 1°C. The specimens used for the diffusion analysis were heat treated in air for times up to 24 h and at temperatures between 160 and 293°C.

The driving forces for the chromium transport were investigated by measuring the surface chromium concentration as a function of time for specimens heated either in a vacuum of 10^{-9} torr or in an oxygen partial pressure of 10^{-5} torr.

Transmission electron microscopy (TEM) was used to determine the gold grain size and film porosity of ion-thinned specimens.

Results and Discussion

Nature of the Driving Forces

It was found that the data obtained by ISS and AES were equivalent, that is, the same information could be obtained by either technique.

Therefore, data obtained with these techniques will not be compared. Typical experimental data from both techniques will be presented.

To investigate the driving forces causing the chromium transport to the gold surface, the chromium surface concentration was determined as a function of time for a fixed temperature in a nonoxidizing and an oxidizing environment. As shown in Fig. 2, at 600°C in a nonoxidizing atmosphere the surface chromium reaches a low saturation value in a short time. When the vacuum chamber is filled with 10^{-5} torr of oxygen, the surface chromium concentration rapidly rises and does not exhibit the surface saturation.

These data are interpreted in terms of two driving forces for chromium transport. The first of these, important at low surface concentrations of chromium, is the free energy of mixing [13]. The dominant driving force in an oxidizing environment with higher concentrations of Cr_2O_3 on the surface is the oxidation of chromium at the gold/air interface. The formation of Cr_2O_3 continually depletes the chromium in solid solution at this interface. Thus, a concentration gradient is maintained through the gold film. The Cr_2O_3 will continue to accumulate until the supply of chromium in the adhesion layer is exhausted [14].

Diffusion Path

The dominant diffusion process (bulk, grain boundary, dislocation, or surface) was determined by sputter profiling the chromium concentration in a gold film heat treated for 2 h at 300°C.

Figure 3 is a plot of the 70-eV gold and 529-eV chromium Auger electron peak heights as a function of material removed. The chromium signal quickly drops below the detection limit (~ 0.1 atomic percent) upon

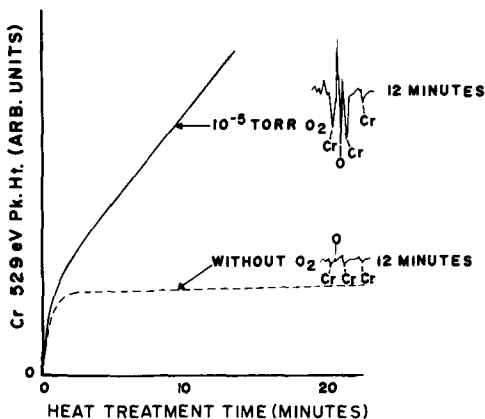


FIG. 2—Chromium surface concentration versus heat treatment time at 600°C in an oxidizing and nonoxidizing atmosphere.

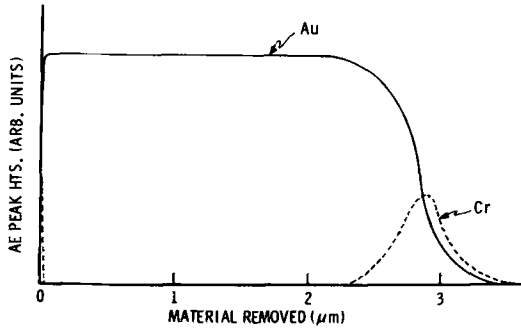


FIG. 3—Sputter profile of chromium and gold concentrations as a function of material removed. The specimen was heat treated in air at 300°C for 2 h.

sputter removing the top few layers of atoms. When the adhesion layer is reached it again rises. If bulk diffusion were responsible for the surface chromium, a concentration gradient should be observed in the gold film. Such a gradient was not observed; therefore, bulk diffusion is discounted as the transport mechanism. This is also consistent with the calculated bulk diffusion rate. For a 30 000 Å film held at 300°C, it would take 4×10^5 h to reach a surface chromium concentration of 0.1 atomic percent based on the bulk diffusion coefficient reported by Pranatis [15]. Chromium transport by surface or dislocation diffusion was discounted, since TEM determined that the films were continuous and pore free and the grains were free of dislocations. Therefore, it seems that grain boundaries are the dominant transport path. This is consistent with the data shown in Fig. 3, since chromium in the grain boundaries would not be detectable by ISS or AES because of the low grain boundary cross-section area. The TEM measurements indicate that the grain size of specimens heat treated at 211°C is not uniform, but the average is 1600 Å. As we shall see, chromium transport dominated by grain boundary diffusion is also consistent with calculations of the surface Cr_2O_3 concentration versus time and temperature.

Diffusion Kinetics

The kinetics of the chromium grain boundary diffusion were determined as a function of the heat treatment temperature. The temperature effect is shown in Fig. 4 where the surface chromium concentration determined by ISS is plotted in arbitrary units as a function of time for heat treatments as 211, 221, 229, and 293°C.

The activation energy and diffusion coefficient can be extracted from these data by considering diffusion along a single grain boundary of length l with unit area. We assume that the initial concentration of chromium in the grain boundary at the adhesion layer interface remains constant at C .

The flux into the gold grain by bulk diffusion with the grain boundaries acting as chromium sources is assumed to be negligible at these temperatures. Based on the free energy of formation of Cr_2O_3 given by Swalin [13], it is assumed that the concentration of chromium in solid solution at the gold/air interface will be essentially zero. With these assumptions, the diffusion along the grain boundary is analogous to gas permeating through a planar sheet of unit area and finite thickness l . For these conditions, Crank [16] gives the total amount of diffusing substance, I_t , which has passed through the sheet (film) in time t as

$$\frac{I_t}{lC} = \frac{Dt}{l^2} - \frac{1}{6} - \frac{2}{\pi^2} \sum_{n=1}^{\infty} \frac{(-1)^n}{n^2} e^{-Dn^2\pi^2/l^2} \quad (1)$$

where D is the diffusion coefficient of the diffusing substance in the film. With the present assumptions, this expression should be applicable to the diffusion along a single grain boundary. An expression which is applicable to films used in the present experiments can be obtained by multiplying the right hand side of Eq 1 by a factor $K(d)$ which is a function of the grain size, d . It is assumed that l is given by the film thickness. This constant accounts for the fact that the film is not a uniform diffusing media but rather that chromium diffuses only through grain boundaries in the film. If

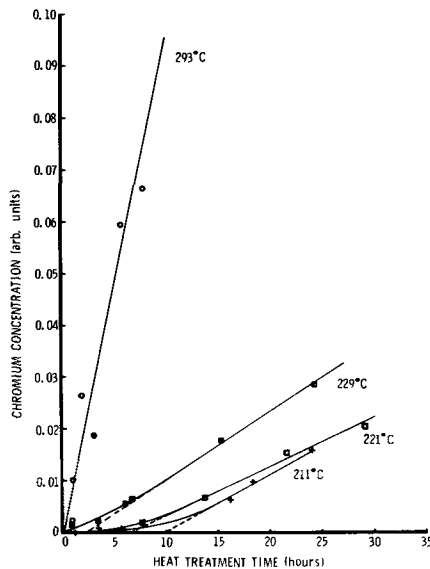


FIG. 4—Surface chromium (as Cr_2O_3) concentration as a function of heat treatment time and temperature experimentally determined by ISS.

the grains are approximated by circles, $K(d)$ is given by $2\delta d$ where δ is the grain boundary width. For $t \gg l^2/D\pi^2$, this expression reduces to

$$I_t = K(d) \left[\frac{D_b}{l} C \left(t - \frac{l^2}{6D_b} \right) \right] \quad (2)$$

which has an intercept, t_o , given by

$$t_o = \frac{l^2}{6D_b} \quad (3)$$

where D_b is the grain boundary diffusion coefficient. Since we have neglected lattice diffusion from the grain boundary into the grain, the grain boundary width, δ , only enters this expression through the factor $K(d)$. Thus, under the present assumptions the grain boundary diffusion coefficient, D_b , can be obtained without assuming a value for δ . It should be pointed up that D_b is an effective diffusion coefficient since films which are several grains thick are used in the measurements and therefore l is an effective thickness.

A plot of Eq 1 and 2 is shown in Fig. 5. As can be seen, the shape is similar to our experimental data plotted in Fig. 4. The transitory period is due to the initial transport of chromium along the grain boundaries. The experimental observation of the transitory period is confirming evidence of little diffusion occurring during deposition.

The activation energy, Q_b , and the preexponential factor, D_{ob} , can be extracted from the time axis intercept, t_o , of projections from the linear portions of the experimental curves by using $D_b = D_{ob} e^{-(Q_b/RT)}$ to rewrite Eq 3 in the form

$$\ln \left(\frac{6t_o}{l^2} \right) = -\ln D_{ob} + \frac{Q_b}{RT} \quad (4)$$

By plotting the natural logarithm of $6t_o/l^2$ versus $1/T$, one can obtain Q_b/R from the slope and $\ln(D_{ob})$ from the intercept.

The same information can, in principle, be obtained by plotting the slope of the linear portions of the curves shown in Fig. 4 versus $1/T$. However, this can only be done if $K(d)$ remains constant. Grain size measurements made by TEM on specimens annealed at temperatures between 211 and 293°C show that the grain size, d , increased with temperature but stabilized in short times at a given temperature. There-

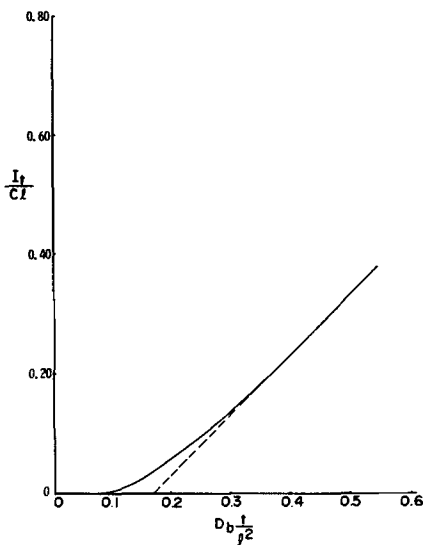


FIG. 5—Plot of the theoretical surface chromium concentration versus time obtained from Eq 1. The dashed line is an extrapolation of the linear portion of the curve (Eq 2).

fore, for the present analysis, only the intercepts, which are independent of $K(d)$, were used in the analysis. A plot of $\ln(6t_0/l^2)$ versus $1/T$ obtained from the experimental data is shown in Fig. 6. An activation energy of 26 kcal/mol and a D_{ob} value of $3.8 \times 10^{-3} \text{cm}^2/\text{s}$ were obtained from the slope and intercept of this curve.

The values of Q_b and D_{ob} determined in the present study are compared to literature data in Table 1. All of the activation energies listed in Table 1 are in reasonable agreement with the present results of 26 kcal/mol except the 43 kcal/mol reported by Pranatis [13]. The reason for this difference is that bulk diffusion controlled the transport in Pranatis' experiment. As we have demonstrated in Fig. 3, grain boundary diffusion is dominant in our experiment. All of the other authors [2-4] have reached the conclusion that defect diffusion was observed in their study, but their conclusion was based only on their measured values of activation energy.

The discrepancy between the present value of D_{ob} and those reported by Rairden et al [2] and Thomas and Haas [4] is due to the type of analysis used in the calculation of D_{ob} . These authors used an expression which is more appropriate for bulk diffusion to obtain D_{ob} while the present result was obtained from an expression which is applicable to grain boundary diffusion. The validity of the present values of D_{ob} and Q_b is supported by the favorable comparison with the grain boundary self diffusion coefficient parameters for gold reported by Gupta and Asai [1].

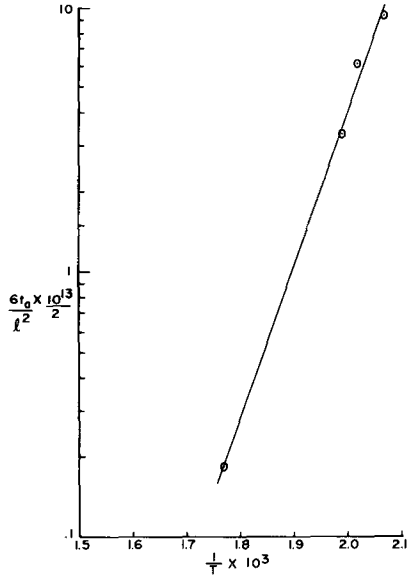


FIG. 6—Plot of the time axis intercepts obtained from Fig. 4 versus $1/T$. The slope of this curve is Q_b/R and the intercept is $-\ln D_{ob}$.

TABLE 1—Comparison of the present value of the activation energy and preexponential factor for chromium diffusion in gold with the literature values.

Investigator	Q , kcal/mol	D_0 , cm^2/s	Remark
Rairden et al [2]	25	1.1×10^{-5}	Au/Cr thin films (resistivity)
Schnable and Keen [3]	25	...	Au/Cr thin films (resistivity)
Thomas and Haas [4]	27.6	3.5×10^{-6} 3.2×10^{-7}	Au/Cr single crystal thin films (work function)
Hirvonen et al [6]	Au/Cr thin films (Rutherford backscattering)
Pranatis [14]	43	9.5×10^{-2}	bulk diffusion couples (electron microprobe)
Gupta and Asai [1] ^a	23	1.8×10^{-2}	self diffusion of Au in grain boundaries (radioactive tracer)
This work	26	3.8×10^{-3}	Au/Cr thin films (ISS/AES)

^aConverting with $\delta = 5 \text{ \AA}$.

Summary

It has been shown that ion scattering spectroscopy and Auger electron spectroscopy can be successfully applied to the determination of grain boundary diffusion in these films by analyzing the amount of material transported, rather than sputter profiling material concentrations.

Experimental data were obtained which clearly shows (a) that the transport of chromium through gold films heat treated in air is predominantly the result (at higher surface concentrations) of the free energy of formation of Cr_2O_3 ; (b) grain boundaries are the major transport paths; and (c) the grain boundary diffusion coefficient preexponential factor, D_{ob} , and the activation energy, Q_b , are given by $3.8 \times 10^{-3} \text{cm}^2/\text{s}$ and 26 kcal/mol, respectively, for chromium in gold grain boundaries.

Acknowledgments

The authors wish to thank G. J. Kominiak and B. S. Gardner for producing the diffusion couples, T. J. Headley for the TEM data, and D. M. Heinze for his able experimental assistance. This work was supported by the U.S. Energy Research and Development Administration.

References

- [1] Gupta, D. G. and Asai, K. W., *Thin Solid Films*, Vol. 22, 1974, p. 121.
- [2] Rairden, J. R., Neugebauer, C. A., and Sigsbee, R. A., *Metallurgical Transactions*, Vol. 2, 1971, p. 179.
- [3] Schnable, G. L. and Keen, R. S., "Study of Contact Failures in Semiconductor Devices," Technical Report RADC-TR-66-165, Rome Air Development Center Research and Technology Division Air Force Systems Command, Griffiss Air Force Base, N.Y., 1966.
- [4] Thomas, R. E. and Haas, G. A., *Journal of Applied Physics*, Vol. 43, 1972, p. 4900.
- [5] Kendrick, P. S., *Nature*, Vol. 217, 1968, p. 1249.
- [6] Hirvonen, J. K., Weisenberger, W. H., Westmoreland, J. E., and Meussner, R. A., *Applied Physics Letters*, Vol. 21, 1972, p. 37.
- [7] Smith, D. P., *Surface Science*, Vol. 25, 1971, p. 171.
- [8] Chang, C. C. in *Characterization of Solid Surfaces*, P. F. Kane and G. R. Larabee, Eds., Plenum, New York, 1974, Chapter 20.
- [9] Siegbahn, K., Nordling, C., Fahlman, A., Nordberg, R., Hamrin, K., Hedman, J., Johansson, G., Bergmark, T., Karlsson, S. E., Lindgren, I., and Lindberg, B., *ESCA-Atomic, Molecular, and Solid State Structure Studies by Means of Electron Spectroscopy*, Almquist and Wiksells, Uppsala, 1967.
- [10] Wood, J. K., Alvarez, J. L., and Maughan, R. Y., *Thin Solid Films*, Vol. 29, 1975, p. 359.
- [11] Danyluk, S., McGuire, G. E., Koliwad, K. M., and Yang, M. G., *Thin Solid Films*, Vol. 25, 1975, p. 483.
- [12] Wildman, H. S. and Howard, J. K., *Journal of Vacuum Science and Technology*, Vol. 12, 1975, p. 75.
- [13] Swalin, R. A. in *Thermodynamics of Solids*, Wiley, New York, 1962, p. 84.

- [14] Holloway, P. H. and Nelson, G. C., "Kinetics of the Transport of Chromium Through Gold Films on Hybrid Microcircuits," SAND75-0216, Sandia Laboratories, Albuquerque, N. Mex.
- [15] Pranatis, A. L., "Diffusion Studies for Microcircuit Metallizations," Report of NRL Progress, Naval Research Laboratory, Washington, D.C., May 1971, p. 21.
- [16] Crank, J., *Mathematics of Diffusion*, Oxford University Press, Fair Lawn, N. J., 1956.

W. D. Bingle¹

Comparison of Evaporated Surface Coatings Using the Ion Scattering Spectrometer and the Auger Electron Spectrometer

REFERENCE: Bingle, W. D., "Comparison of Evaporated Surface Coatings Using the Ion Scattering Spectrometer and the Auger Electron Spectrometer," *Surface Analysis Techniques for Metallurgical Applications, ASTM STP 596*, American Society for Testing and Materials, 1976, pp. 79-85.

ABSTRACT: Ion scattering and Auger spectrometry have proven to be useful analytical techniques for elemental analysis of surface composition. However, few, if any, previous studies have been made to show the variations that exist between the two analytical techniques. To better illustrate the difference in results between the two analytical techniques, a series of thin film evaporated coatings were prepared on different substrates for examination and analysis on both the ion scattering spectrometer (ISS) and Auger electron spectrometer (AES). Some basic agreement between the two techniques is noted; however, the variation with substrate and extraneous element concentrations shows that the characterization of material surfaces using ISS and AES demands further investigation and development before quantitative analyses can be attempted.

KEY WORDS: spectroscopy, surface analysis, ion scattering, evaporated thin film, quantitative analysis, materials tests

To better understand the results obtained from two different surface analytical techniques (ion scattering and Auger analysis), thin film coatings were evaporated onto different substrate materials for comparative analyses. This comparison was also made to determine which instrument would be best suited for examination of materials that are of concern to this laboratory. Thin films of carbon, aluminum, and copper were evaporated onto glass, aluminum, iron, and platinum to produce a wide mass range in both the coating and the substrate to show the capabilities

¹ Senior research physicist, National Steel Corporation, Research Center, Weirton, W. Va. 26062.

of each instrument. Similar specimens were then analyzed in both the ion scattering spectrometer (ISS) and the Auger electron spectrometer (AES). The raw intensity data from each technique were then converted to atomic percent using the standard method for each process. Both instruments have been described elsewhere,^{2,3,4} and only a brief description will be given here.

Ion Scattering

In ISS the surface to be analyzed is bombarded with noble gas ions which undergo elastic collisions with the surface atoms with a resultant loss in energy. The distribution of scattered ion energy is presented as a ratio of final energy to incident energy. Due to the short interaction time of the ion with the surface atom, the chemical status and matrix dependencies do not enter into the analysis on a first order basis. The limited resolving power of ISS is such that some elements can go undetected if a neighboring element's peak is of much larger magnitude. The same low energy ion beam which is doing the analysis is also simultaneously removing the surface atoms to produce a depth profile analysis. The energy of the recoil ion is a function of the mass of the atom it encountered, and for a 90-deg scattering angle the relationship is quite simple. If E_0 is the kinetic energy of the primary ion of mass M_0 and E_1 is the energy after being scattered during an elastic collision with a surface atom of mass M_s , the mass of the surface atom is determined from the relation

$$E_1/E_0 = \frac{M_s - M_0}{M_s + M_0}$$

Thus, by selection of the mass primary ion, M_0 , and measuring the energy ratio E_1/E_0 , M_s is calculated. There is a single peak for each element on the surface, and the height of the peak is related to the concentration of this element in the outer monolayer. Analysis of insulators requires the use of charge neutralization, a flow of electrons from a heated wire onto the specimen. This returns the specimen to its proper potential and allows the peaks to appear at their proper position.

Auger Analysis

Auger electron spectroscopy is accomplished by bombarding the specimen surface with a primary electron beam while energy analysis is performed on the resultant secondary electrons. The primary beam

² Carbonara, R. S., *Microstructural Analysis Tools and Techniques*, Plenum, New York.

³ Smith, D. P., *Surface Science*, Vol. 25, 1971, p. 171.

⁴ Harris, L. A., *Journal of Applied Physics*, Vol. 39, 1968, p. 1419.

ionizes one of the surface atoms under bombardment and leaves it in an excited, higher energy state. The atom may return to its equilibrium lower energy state by either of two processes: (1) the system can give rise to an X-ray photon which is what takes place and is measured in microprobe analysis, or (2) the system can go through an Auger radiationless transition in which the available energy is transferred to a third electron which, if it possesses enough energy, can escape from the surface and be detected. For the light elements, the Auger process dominates while the X-ray process dominates for the higher atomic number elements. The Auger electron energy is related to the various energy levels of the bombarded atom, and, with an energy plot for the ejected electrons, a method of identifying the elements is possible. The energy distribution Auger curve has a large, rapidly changing background associated with small Auger peaks, and, to reduce the background and make the small peaks more pronounced, the derivative of the energy distribution curve is taken. The sampling depth of AES is determined by the escape depth of the Auger electrons. Low energy electrons have only sufficient energy to escape from the near outer surface, while high energy electrons have sufficient energy to escape from further beneath the surface and be detected. Most elements exhibit both high and low energy Auger transition peaks, and, with proper selection of peaks, the uncertainty in escape depth can be kept to a minimum.

Procedures and Results

Measured amounts of carbon, aluminum, and copper were placed in a tungsten basket and evaporated to form a coating on a series of cleaned glass, aluminum, iron, and platinum disks. The substrates were placed at such a distance to make the coating 30 Å thick as determined by the amount of material available for evaporation and its density. The various factors that influence the ability to form a uniform and complete surface covering were not considered, as both the ISS and the AES would analyze specimens with identical coatings within the limitation imposed by the difference in beam diameter of 1/10 mm for AES compared to 1 mm for ISS.

After obtaining ISS and AES spectra from each specimen, the peak intensities for each element were converted to atomic percent using the following equations.

$$\text{AES} \quad C_x = I_x / S_x \cdot \text{Ag} / \sum I_a / S_a \cdot \text{Ag} \times 100$$

$$\text{ISS} \quad C_x = I_x / \sigma_x / \sum I_a / \sigma_a \times 100$$

where

$$C_x = \text{concentration in atom percent of element } x,$$

$$I_q = \text{measured signal intensity of element } q,$$

$$S_{q, \text{Ag}} = \text{relative sensitivity of element } q \text{ to silver, and}$$

$$\sigma_q = \text{atomic scattering cross section of element } q$$

and where $\sum I_q/S_{q, \text{Ag}}$ and $\sum I_q/\sigma_q$ are taken over all the elements detected, including element x .

Tables 1, 2, and 3 show the atomic percent of elements detected by ISS and AES for substrates of glass, aluminum, iron, and platinum that were coated with 30 Å of evaporated carbon, aluminum, and copper. The relative variation between the ISS and AES data should only be compared, as the thickness and completeness of the coating cannot be determined for absolute comparison. Also, the sputtering rate for all ISS analyses was 1 Å/min with a 5-min analysis time which means that the ISS data were accumulated over a depth of 5 Å. Carbon is relatively equally detected by ISS and AES on the aluminum, iron, and platinum substrates. The variation between the two techniques for detecting carbon on glass may be the result of specimen handling or the fact that the substrate is nonconductive. In all of the examples of Table 1 except for iron, AES has detected more of the base metal than ISS. For all of the specimens, except for carbon on glass which has oxygen in the base material, the ISS data seem to indicate that oxygen is adsorbed or forms an oxide on the

TABLE 1—Surface analysis of carbon film on various substrates using two analytical techniques.

30 Å Carbon		Atomic Percent Detected						
On glass	C	Si	O	Na	Mg	Fe	Ni	
ISS ^a	56	12	15	17	
AES	25	50	20	4	2	<1	<1	
On aluminum	C	Al	O	Na	Mg	S	Ni	Cl
ISS	70	11	20
AES	73	17	1	3	5	<1	<1	<1
On iron	C	Fe	O	Na	S	Cl	Ni	
ISS	86	4	10					
AES	93	2	1	2	<1	<1	<1	
On platinum	C	Pt	O	Fe	Zn	S	Ni	Cl
ISS	82	7	11
AES	71	24	1	1	1	<1	1	1

NOTE—All ISS analyses performed with ³He ions at 2500 eV.

^a Charge neutralization used.

TABLE 2—*Surface analysis of aluminum film on various substrates using two analytical techniques.*

30 Å Aluminum		Atomic Percent Detected					
On glass	A1	O	Si	C	Au		
ISS ^a	35	65	1		
AES	60	11	12	16	...		
On aluminum	A1	O	Mg	C	Au	S	Cl
ISS	40	58	2
AES	57	10	4	28	...	<1	<1
On iron	A1	Fe	O	C	Au		
ISS	38	4	55	...	3		
AES	56	2	10	32	...		
On platinum	A1	Pt	O	C			
ISS	50	4	46	...			
AES	52	15	9	24			

NOTE—All ISS analyses performed with ⁴He ions at 1500 eV.

^a Charge neutralization used.

evaporated layer, while the AES data show only a trace of oxygen. The other trace elements not detected by ISS could be the result of the greater sensitivity of AES for the light elements compared to ISS.

Table 2, which has the ISS and AES data for 30 Å of aluminum, shows that some spread is noted between the two techniques for aluminum, especially on the glass substrate. The ISS data show a large oxygen signal with no detection of carbon as compared to the Auger data. The ISS data show a trace of gold on the aluminum-coated specimens which is contamination from the vacuum evaporator that was used previously to evaporate a gold coating. The gold peak was not detected on the platinum specimen due to the poor resolution of the ISS for the heavy mass elements. The carbon detected by AES could also have been contamination from a previous use of the evaporator. The poor sensitivity of ISS for the light elements, coupled with the poor sensitivity of AES for the heavy mass elements, must be taken into account when studying the data.

Table 3, which shows the data for the copper coating, also shows wide variations between ISS and AES results, especially for carbon and oxygen.

On all three evaporated films the substrate material was detected by both the ISS and AES, but in varying amounts. This could be a result of nonuniform application of the evaporated film which results in individual islands of coating material, a result of variations in coating thickness, or the result of the fact that the depth of analysis for the two techniques is greater than the coating thickness.

TABLE 3—Surface analysis of copper film on various substrates using two analytical techniques.

30 Å Copper		Atomic Percent Detected					
On Glass	Cu	O	Na	C1			
ISS ^a	53	29	13	5			
AES		not available					
On aluminum	Cu	Al	O	Mg	C	S	C1
ISS	53	17	30
AES	24	18	5	6	43	1	3
On iron	Cu	Fe	O	Na	C	Au	C1
ISS	55	2	27	14	...	4	...
AES	25	1	3	...	65	...	6
On platinum	Cu	Pt	O	Na	C	S	C1
ISS	54	13	19	9	6
AES	24	24	4	...	42	1	6

NOTE—All ISS analyses performed with ⁴He ions at 1500 eV.

^a Charge neutralization used.

Discussion

This study has shown that differences exist between ISS and AES analytical results obtained from analyzing similar thin film evaporated specimens. The basic differences between ISS and AES with regard to the type of analyzing probe, its depth of penetration, the power input, the method of signal formation, and the depth of analysis make it unrealistic to expect identical results from analysis of similar specimens. The large carbon and oxygen variations, as well as the difference in amount detected between the two instruments, have been described. This large variation in carbon and oxygen concentration as determined by ISS and AES could be a result of a difference in depth of analysis. A monolayer of oxygen on the specimen surface would give a higher concentration when analyzed with the ISS which is more sensitive to the outer monolayer than AES. The carbon that is most evident in AES could actually be forming on the surface under the influence of the high energy electron beam, or it could be on the surface and the poor sensitivity of ISS for carbon would result in low amounts detected. The equations used to convert intensity to atomic percent do not produce accurate quantitative results as the total is normalized to 100 percent, which means detection of an excessive subsurface signal or the lack of detection of a surface monolayer constituent could greatly influence the calculated concentration. The sensitivity factors that are used to convert intensity to atomic percent

need to be modified, and additional terms will have to be developed to reduce this problem.

Both ISS and AES give useful information which when combined with the basic knowledge of each analytical process can provide worthwhile surface analytical information. However, additional development and study are necessary to provide quantitative analytical surface analysis.

W. L. Baun,¹ N. T. McDevitt,¹ and J. S. Solomon²

Chemistry of Metal and Alloy Adherends by Secondary Ion Mass Spectroscopy, Ion Scattering Spectroscopy, and Auger Electron Spectroscopy

REFERENCE: Baun, W. L., McDevitt, N. T., and Solomon, J. S., "Chemistry of Metal and Alloy Adherends by Secondary Ion Mass Spectroscopy, Ion Scattering Spectroscopy, and Auger Electron Spectroscopy," *Surface Analysis Techniques for Metallurgical Applications, ASTM STP 596*, American Society for Testing and Materials, 1976, pp. 86–100.

ABSTRACT: In order to reduce empiricism in the design of adhesive bonded systems, one parameter, among many which must be determined, is the chemical composition just at the surface of the metal or alloy adherend surface. Numerous surface chemistry techniques to deduce surface composition have been developed such as secondary ion mass spectroscopy (SIMS), ion scattering spectroscopy (ISS), and Auger electron spectroscopy (AES). Each of these (as well as other) techniques when used alone can be a useful profiling tool but become far more powerful when combined with another method. The complementary nature of SIMS/ISS and SIMS/AES make them especially useful combinations. The weakness of one is generally the strength of the other. Specific examples of this strength-weakness relationship are shown for materials studied in research on adhesive bonding. Nearly every chemical and thermal treatment results in changes in surface composition. Even different treatments to pure metals can result in stoichiometry differences between anion and cation or apparent formation of various compounds on the surface. Certainly, it is necessary to know what the composition actually is at the surface in order to properly design an adhesive bonded system. The nominal composition of an alloy bears little resemblance to the surface composition, in most cases.

KEY WORDS: spectroscopy, adhesive bonding, adhesives, adherends, surface characterization, surface chemistry, chemical pretreatment, thermal pretreatment adhesive failure, cohesive failure

¹ Research chemists, Air Force Materials Laboratory (MBM), Wright-Patterson Air Force Base, Ohio 45433.

² Research scientist, University of Dayton Research Institute, Dayton, Ohio 45409.

Adhesive bonded structures are being used increasingly in the aerospace and other industries for primary and secondary load bearing members. Adhesive bonding offers many advantages over conventional joining techniques. Generally, adhesive bonded structures are lighter, less expensive, and more corrosion resistant compared to riveted or bolted assemblies. In order to reduce empiricism in the design of adhesive bonded joints, we must determine the effect on bond strength and durability of many parameters, as shown in Fig. 1, where a complete design and testing program is outlined. One of these parameters, the chemistry of the adherend surface, may be determined by several recently developed spectrochemical techniques such as Auger electron spectroscopy (AES), ion scattering spectroscopy (ISS), and secondary ion mass spectroscopy (SIMS). This paper presents results of surface characterization experiments using these techniques on adhesive bonded materials to determine the effect of surface chemistry on bond characteristics.

Experimental

Secondary ion mass spectroscopy used alone has been shown to be a powerful tool for elemental surface characterization [1,2].³ However, because of uncertain or rapidly changing secondary ion yields [3,4] (due to changes in chemical bonding), quantitative analysis is virtually impossible using only SIMS. Nevertheless, the extremely high sensitivity of SIMS coupled with the fact that it is a simple inexpensive technique makes SIMS useful to determine surface chemistry. It is suited ideally for use with other depth profiling methods since these techniques already use, for depth profiling, a beam of ions of the correct energy to use for SIMS. Further, SIMS is complementary to other methods such as ISS and AES as shown in Table 1 where features of the three techniques are reviewed.

Equipment

The SIMS was added to two commercial instruments, the 3M ISS system⁴ and the Physical Electronics Industries Model 540 thin film analyzer (AES).⁵ In the ISS instrument, a UTI 100C quadrupole mass spectrometer⁶ was equipped with a simple three-element cylindrical energy analyzer in front of the quadrupole mass filter, as illustrated in Fig. 2. Since the gas ionizer had been removed to provide space for the energy analyzer, an auxiliary filament assembly outside the energy analyzer, as shown in Fig. 2, allowed switching to residual gas analysis (RGA) mode. In the AES instrument, a Model 1100 EAI mass spectrom-

³ The italic numbers in brackets refer to the list of references appended to this paper.

⁴ 3M Company, 3M Center, St. Paul, Minn.

⁵ Physical Electronics Industries, Eden Prairie Minn.

⁶ Uthe Technology International, Sunnysvale, Calif.

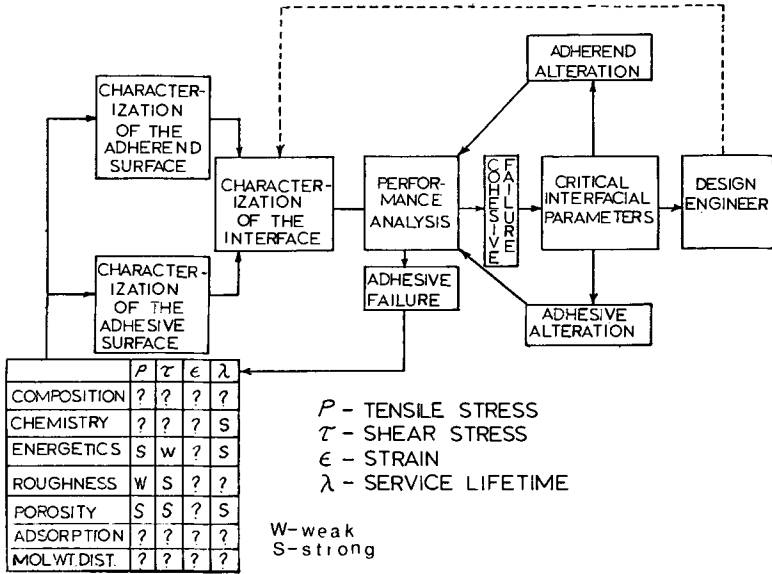


FIG. 1—Interactive matrix showing relation of surface parameter to design and performance of the adhesive bond.

ter⁷ was equipped with a three element energy filter which extends into one of the ports whose centerline extends to the specimen. Such a port is the microscope port. The modifications on this analyzer did not require removal of the ionizer section, allowing easy switching to RGA mode.

Results and Discussion

Chemical Treatments

Many chemical etching and oxidizing treatments are used on metals and alloys to enhance adhesive bonding of the surface. Numerous thermal pretreatments following fabrication improve strength, ductility, toughness, or other property. Each of these chemical or thermal treatments affect the composition of the surface either by introducing impurities or by increasing or decreasing the concentration of alloying elements at the surface.

An example of changing surface chemistry is seen in Fig. 3 where ISS and + SIMS data are shown for the aluminum alloy 7050 (nominal zinc 6.2 percent, copper 2.3 percent, magnesium 2.2 percent, and zirconium 0.12 percent) treated using an acid (nitric acid/hydrofluoric acid (HNO₃/HF)) etch at the bottom and for the same surface anodized at the top of the figure. The etch leaves the surface fluorine rich. The fluorine remains

⁷ Electronic Associates, Inc., Palo Alto, Calif.

TABLE 1—Comparison of surface analytical techniques.

Parameter	ISS	SIMS	AES
Principle	elastic binary collision with surface ion	sputtering of surface atoms by ion beam	ejection of Auger electron upon recombination
Probe	~ 1 to 3 keV ions	~ 1 to 3 KeV ions	~ 1 to 3 KeV electrons
Signal	ion current versus energy	ion current versus mass	derivative e' emission versus energy
Applicable elements	$Z > 3$	nearly all (if positive and negative SIMS)	$Z > 3$
Sensitivity, general	high	variable	variable
Sensitivity, low Z	low	high	high
Resolution (spectral)	low	high	moderate
Spectral shift	possible, but generally no	no	yes
Information on chemical combination	no, only by inference	in some cases, usually no	yes
Quantitative analysis	yes	probably no, maybe with similar standards	yes, in principle but difficult
Influence of operating conditions and matrix	no	yes	yes
Isotopic analysis	yes, in principle but generally no because of resolution limits	yes	no
Beam induced surface changes	slight	slight	yes, on heat sensitive materials

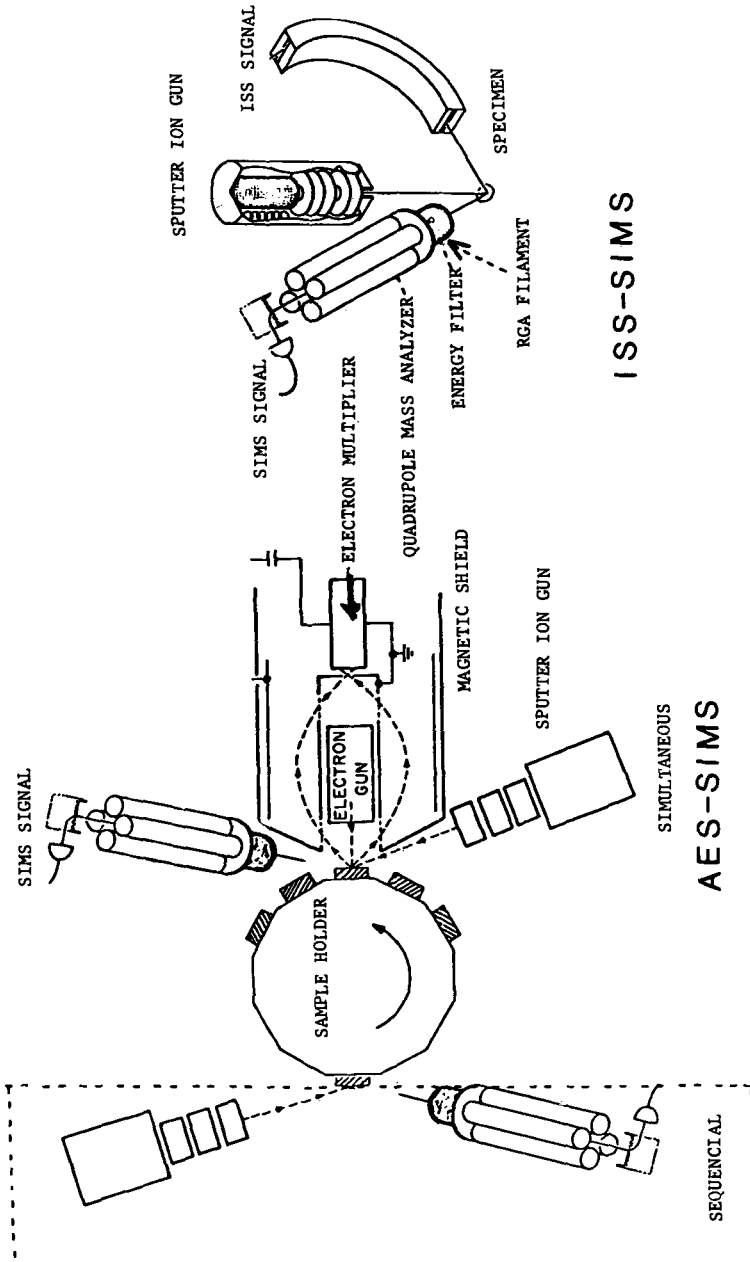


FIG. 2—Essential components in ultrahigh vacuum for combination AES/SIMS and ISS/SIMS characterization of surfaces.

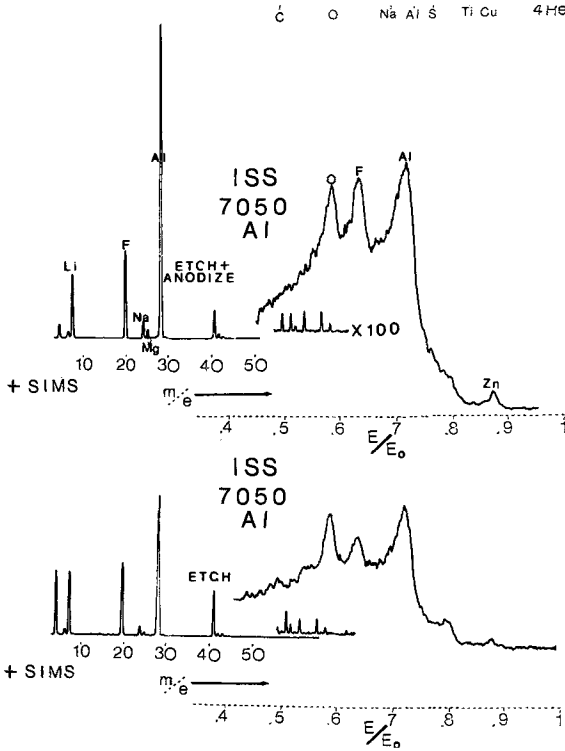


FIG. 3—ISS/+SIMS data from 7050 aluminum alloy etched with dilute HNO_3/HF and then anodized (top).

on the surface during anodic oxide growth to produce not aluminum oxide as expected but rather an apparent aluminum oxyfluoride of unknown structure. Forest Products Laboratory (FPL) etch applied to this same alloy results in the surface becoming very zirconium rich even though the bulk concentration of zirconium is only 0.12 percent.

Often various processing steps on aluminum alloys result in the formation of "smut," a loosely adhering powdery dark-colored material on the surface which makes it unsuitable for bonding. One such smut was formed on 2024 aluminum alloy (nominal copper 4.5 percent, manganese 0.6 percent, magnesium 1.5 percent) with a standard chromate stripping solution. Figure 4 shows ISS and SIMS data from the smutted surface compared to an area which had been above the solution and had not become smutted. The ISS spectrum of the smut shows it to be virtually all copper. Similarly, SIMS shows a high concentration of copper even though the positive ion yield for copper is low. Because of this low yield and the corresponding high yield of chromium, the SIMS spectrum from the smut appears to show a high concentration of chromium. Such spectra

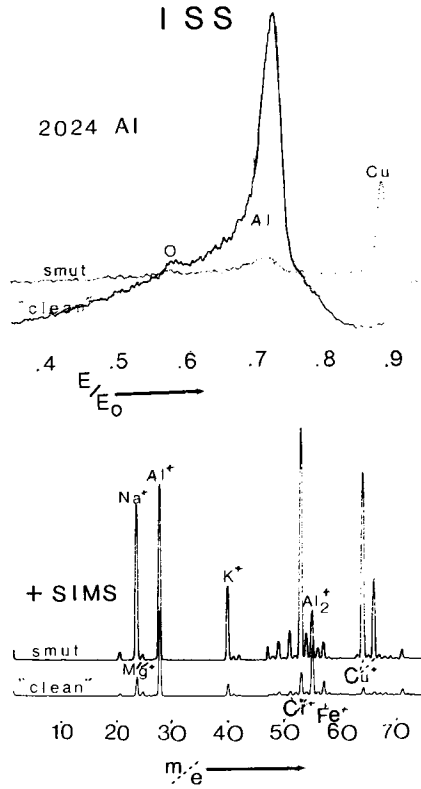


FIG. 4—ISS and +SIMS spectra from smut formed on 2024 aluminum alloy along with spectra obtained from the clean alloy.

must be carefully interpreted in order to estimate concentrations at the surface. Neither ISS nor +SIMS is sensitive to carbon, especially in finely divided form on the surface. Auger electron spectroscopy, however, has extreme sensitivity as shown in Fig. 5 where AES data are shown for the same smutted and "clean" surfaces as seen in Fig. 4. In these spectra one sees, in addition to an increase in copper concentration, a very high concentration of carbon, the origin of which is not clear.

Many other changes and abnormalities in surface composition have been observed. Even "as received" materials show surprising surface composition as seen in Fig. 6 where SIMS and ISS data on 2024 aluminum alloy (degreased) indicate high magnesium concentration at the surface. Conventional alkaline cleaning treatments do not etch the surface appreciably, leaving the surface magnesium rich. Such a surface when adhesively bonded may exhibit long time durability anomalies when compared with bonded structures in which formation of aluminum oxide has been ensured. A comprehensive report showing changes in surface composi-

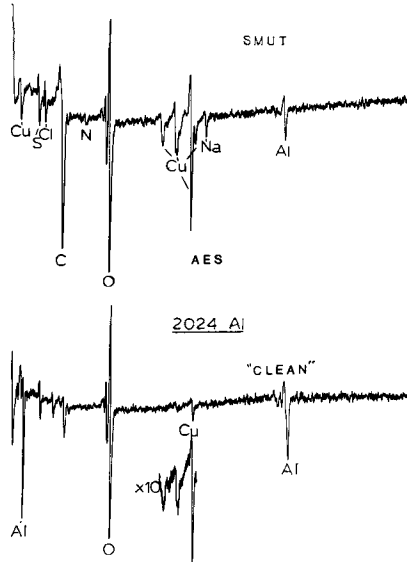


FIG. 5—AES data from the same smut and clean surfaces as shown in Fig. 4.

tion with various chemical treatments for 2024 and 7075 aluminum alloys has been prepared [5]. Data from AES, ISS, and SIMS have been included.

Compositional changes with depth on adherends are common and can seriously affect initial bonding and long term stability of the adhesive bond. The thin film analyzer using AES provides excellent elemental profiles. The other techniques used here (ISS and SIMS) display serious cratering problems which smear the profiles unless special beam rastering

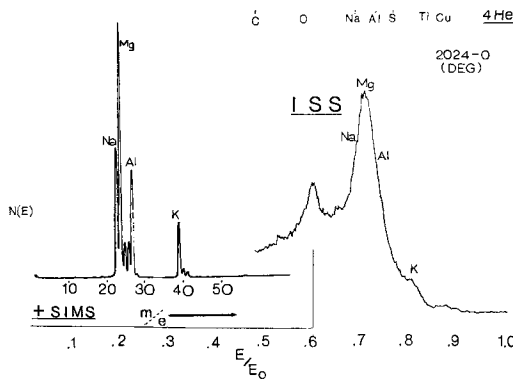


FIG. 6—ISS and SIMS data from 2024 aluminum alloy. No treatment except for degreasing (data from Ref 5).

and gating techniques are employed. Because AES uses a small electron beam centered on a much larger ion beam which slowly erodes the surface, it is not troubled by cratering anomalies. An example of a typical elemental profile obtained by AES is shown in Fig. 7 where normalized curves are shown for copper, oxygen, and aluminum from a 2024 aluminum alloy treated with FPL etch. As can be seen, the copper is concentrated at the interface between the oxide and metal. Changes in the FPL treatment, such as temperature and rinse times, change the width and shape of this copper distribution at the interface.

Thermal Effects

Many striking effects occur at the surface with thermal treatment. Such effects are seen on stainless steels. The chemistry of stainless steels is very interesting. Historically, one is told [6] that stainless steel is protected from reaction by a tenacious layer of chromium oxide which produces a passive surface. We have found in this work that such a general assumption of the presence of an inert layer of chromium oxide cannot be made.

The surface of Types 301 and 302 and probably all stainless steels may be either chromium rich or iron rich depending on previous surface history. A surface which has had no treatment except degreasing following rolling shows a thin iron rich region at the surface followed by a slight thicker layer which is chromium rich. Heating these surfaces to less than incandescence in air results in a golden film showing the same relationships, except both layers are thicker than in the untreated surface. When either the original or heated surfaces are sputtered clean, that is, until a constant iron/chromium ratio is obtained by ISS and SIMS, and allowed to stand in ultrahigh vacuum (UHV), the surface becomes markedly chromium rich.

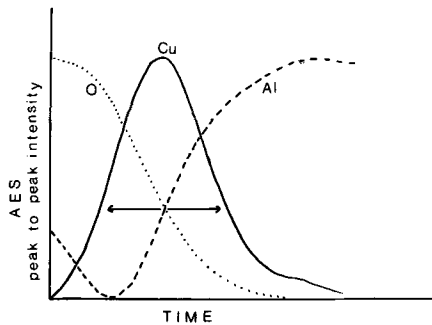


FIG. 7—Normalized elemental profiles for aluminum, oxygen, and copper from 2024 aluminum alloy treated with FPL etch.

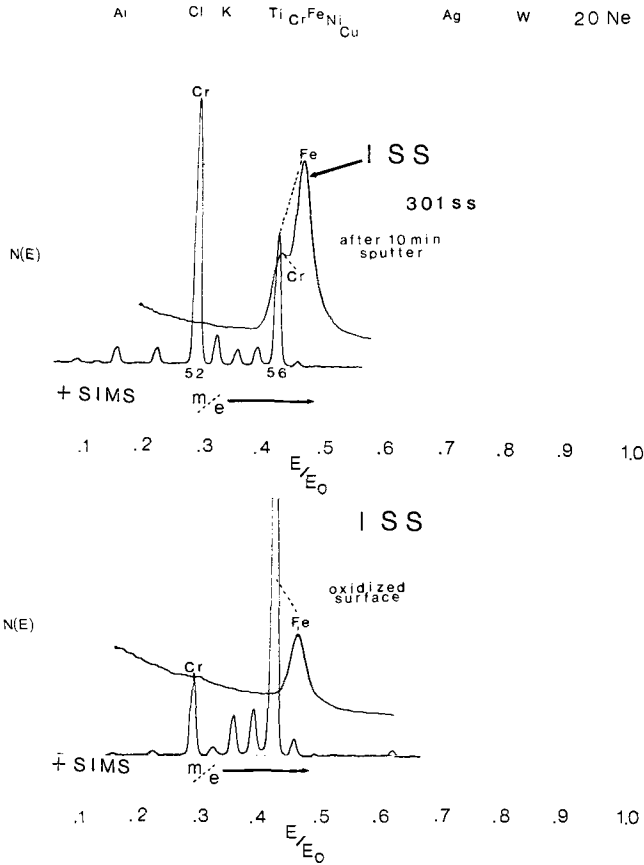


FIG. 8—ISS and +SIMS data from Type 301 stainless steel heated to less than incandescence in heat gun (oxidized surface) and after 10-min sputter with ^{20}Ne at 2500 V.

The iron rich layer produced when the stainless steel is heated only in the same region that it reaches during processing or heat treating gives the ISS and SIMS spectra shown in Fig. 8 at the bottom of the figure. After 10 min sputtering with ^{20}Ne at 2500 V, the spectra at the top of the figure were obtained. The iron/chromium ratio has not yet reached the bulk value but uncertain ion yields and cratering effects make it very difficult to determine the exact concentration of iron and chromium using either ISS or SIMS.

Determining Locus of Failure

The strength of an adhesive joint is assessed by means of physical tests such as single lap shear, double lap shear, peel, etc., in which an increasing load is placed in the joint until failure occurs. Following failure, visual (or sometimes microscopic) examination of the surfaces is made to

determine the mode of failure. If adhesive remains on each adherend and the joint appears to have failed in the adhesive itself, the failure is termed "cohesive" failure. If the failure appears to have occurred at the interface between the adhesive and adherend, the failure is termed "adhesive."

Bikerman [7] says that rupture so rarely proceeds exactly between the adhesive and adherend that these events (that is, "failure in adhesion") need not be treated in any theory of adhesive joints. He points up that apparent failures in adhesion are quite common, but they take place so near the interface that the adhesive remaining on the adherend after the rupture is not visible. Good [8] has analyzed adhesive joint failure and reports that interfacial separation is highly improbable when true wetting of the surface has taken place.

Frequently, it is not simple using visual or even microscopic examination to determine after testing whether an apparent adhesive failure occurred at the interface due to improper wetting or at some new interface leaving behind a thin layer of adhesive. Even scanning electron micrographs are not definitive for very thin layers of adhesive. Often surface features of the original adherend are closely reproduced by a surface covered by a thin film of adhesive. Further, there is a resolution limitation of about 100 Å for most scanning electron microscopes which makes very thin films difficult to detect, especially when the adhesive is a pure polymer containing no filters of a higher atomic number than the polymer. Optical and staining methods have been reported [9] to determine the presence of adhesive films. However, the optical technique uses the interference phenomenon which is only applicable to fairly thick films, certainly not films only a few angstroms thick. Staining techniques are sensitive only to specific compounds present in the usually complex adhesive systems.

Ion scattering spectrometry and secondary ion mass spectrometry provide useful information on the locus of failure in an adhesive joint even when the film is only on the order of atomic dimensions or when the failure occurs near the original interface and includes parts of both the adhesive and adherend. Auger electron spectroscopy has been found to be less useful primarily because of heating effects of the electron beam which causes decomposition of adhesive surfaces.

An example of the use of ISS/SIMS for analysis of adhesive bonded surfaces is shown in Figs. 9 and 10. Data here are from a titanium, commercially pure adherend which was anodized, bonded, subjected to lap shear testing, and appeared to fail in an adhesive mode. That is, there appeared to be failure at the interface of the oxide and adhesive. The adhesive was a modified epoxy with a magnesium silicate filler. Therefore, there are several elements such as carbon, nitrogen, magnesium, and silicon to search for to determine whether failure was truly adhesive or whether, in fact, failure occurred along a new interface. As can be seen by

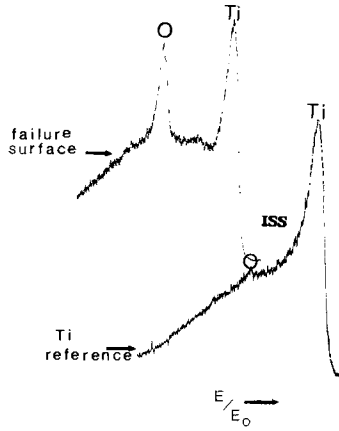


FIG. 9—ISS spectra from titanium adherend following testing from anodized failure surface and from reference point on end of adherend.

the ISS spectra in Fig. 9, the titanium scattered peak exhibits long tailing to low energy which obscures carbon and nitrogen to low E/E_0 of the oxygen peak and both magnesium and silicon between the oxygen and titanium peaks. In this figure, the ISS spectrum is shown for the anodized failure surface and for a reference area on the end of the adherend which had not been anodized. Note the change in oxygen to titanium peaks when going from a metallic surface to the anodized oxide surface. Because of the high solid solubility of oxygen in titanium, some oxygen is nearly always visible, even in pure vacuum evaporated films which have been

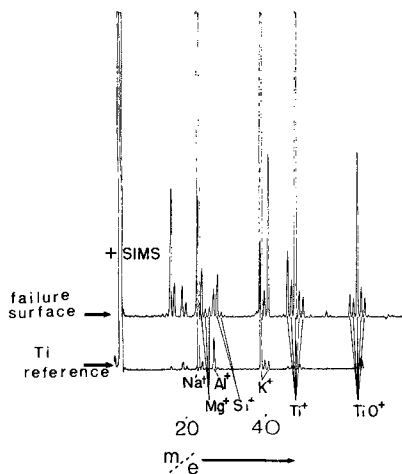


FIG. 10—Plus SIMS spectra from same surfaces as in Fig. 9.

sputtered to remove surface oxide. Even though in this case little information is gained on the locus of failure, the data may be used to determine oxide thickness and homogeneity, if the capability exists to raster and gate the ion beam to reduce cratering effects.

The SIMS spectra in Fig. 10 taken simultaneously with the ISS spectra of Fig. 9 do not suffer the limitations of ion scattering. Each of the elements of interest along with titanium is observed on the failure surface, indicating breakage on a new interface. Note the increase in plus ion efficiency from the oxide failure surface compared to the unbonded surface shown for reference. Note also the great increase in sodium and potassium on the failure surface compared to the unbonded surface. Migration of these mobile monovalent ions to the interface is commonly seen especially in adherend-adhesive systems requiring a heat cure to effect a bond. In this adhesive joint failure, the first SIMS traces before erosion into the surface took place showed elements from both adhesive and adherend. Failure probably occurred near the original interface. If the interface is considered to be an interlocking of "mountains and valleys" on the adherend with the adhesive, then we must be seeing cohesive failure of the adherend in the mountains as well as cohesive failure of the adhesive filling the valleys, although these results do not rule out also some possible adhesive failure.

Figure 11 shows ISS and SIMS data from an aluminum adherend which had been bonded with epoxy containing a titanium dioxide (TiO_2) filler.

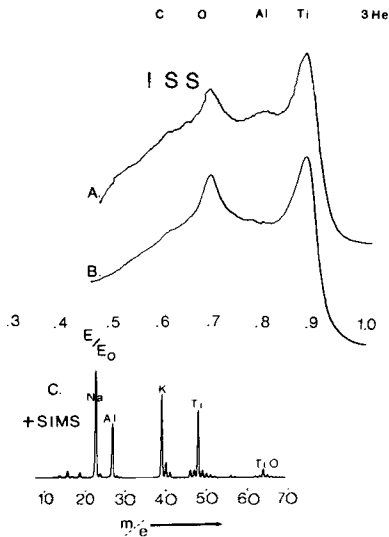


FIG. 11—ISS and +SIMS from failure surface of anodized aluminum; adherend bonded with TiO_2 filled epoxy; (a) ISS, failure surface; (b) ISS, TiO_2 reference; and (c) +SIMS, failure surface.

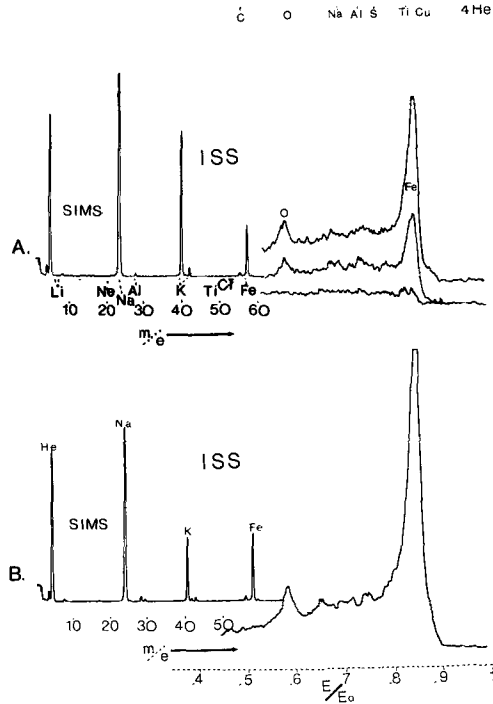


FIG. 12—ISS and +SIMS data from low carbon steel adherend which was debonded from Nylon 12; top spectra from surface, bottom after 10-min sputter with ^4He at 2500 V.

The ISS Spectrum A of the failure surface shows carbon, oxygen, aluminum, and titanium. Spectrum B is from TiO_2 and is shown for reference purposes. Such a reference spectrum may be subtracted from an “unknown” spectrum to enhance features which are normally obscured. The SIMS spectrum at the bottom of the figure corroborate the ISS results, indicating as in the earlier titanium illustration that failure did not occur cleanly at the aluminum oxide (Al_2O_3) surface, but rather in a complex region containing both adhesive and adherend.

The majority of failure surface examined which appeared to be adhesive failure have been of the type shown in the examples where cohesive failure in both materials appear to have occurred. It is necessary to be able to determine by ISS, SIMS, AES, or some other elemental analysis method whether the surface contains both adhesive and adherend, since a test only for the adhesive on the adherend might cause an incorrect deduction of failure mode and location. For instance, a test for adhesive such as differential scanning calorimetry as performed by Bair and co-workers [10] to determine the amount of branched polyethylene adhering to a copper oxide surface does not in itself prove that the mode of failure was only cohesive in the polymer.

Some failures which could be classed as pure adhesive or cohesive have been examined by ISS/SIMS. Adherend surfaces which were obviously not wet by the adhesive showed no trace of the adhesive or the adherend. Often these surfaces were "dirty" and showed a thin layer of contaminating elements on the adherend. This kind of failure probably should not be considered adhesive if proper bonding between the two surfaces never occurred. An example of this phenomenon is seen in Fig. 12. At the top of the figure, ISS and SIMS spectra are shown for a low carbon steel surface following debonding of the thermoplastic Nylon 12 from the surface. The first ISS spectra show only weak peaks near potassium and iron. The corresponding SIMS data show strong sodium and potassium peaks compared to iron. As sputtering continues, sodium and potassium decrease and iron increases as shown at the bottom of the figure where ISS and SIMS data are shown after 10 min sputter time with ^4He at 2500 V. As was indicated earlier, this segregation of monovalent ions to the surface of adherends which have been heated is a common occurrence.

Conclusions

The chemistry of adherend surfaces may be markedly changed by chemical and thermal treatment. The chemistry of such surfaces is important to the overall performance and durability of the adhesive joint. The combination of SIMS and ISS and AES provides a useful tool to determine surface composition and locus of failure in adhesive bonds.

References

- [1] Benninghoven, A., *Surface Science*, Vol. 28, 1971, p. 541.
- [2] Schubert, R. and Tracy, J. C., *Review of Scientific Instruments*, Vol. 44, 1973, p. 487.
- [3] Schubert, R., *Journal of Vacuum Science and Technology*, to be published.
- [4] Werner, R., *Developments in Applied Spectroscopy*, Vol. 7A, 1969, p. 297.
- [5] McDevitt, N. T. and Baun, W. L., AFML TR 75-122, Air Force Materials Laboratory, Wright-Patterson Air Force Base, Ohio.
- [6] Kohl, W. H. in *Handbook of Materials and Techniques for Vacuum Devices*, Reinhold, New York, 1967, p. 170.
- [7] Bikerman, J. in *Recent Advances in Adhesion*, Lieng-Huang Lee, Ed., Gordon and Breach, New York, 1973.
- [8] Good, R. J. in *Recent Advances in Adhesion*, Lieng-Huang Lee, Ed., Gordon and Breach, New York, 1973, pp. 357-377.
- [9] Brett, C. L., *Journal of Applied Polymer Science*, Vol. 18, 1974, p. 315.
- [10] Blair, H. E., Matsuoaka, S., Vadimsky, R. G., and Wang, T. T., *Journal of Adhesion*, Vol. 3, 1971, p. 89.

D. E. Newbury,¹ K. F. J. Heinrich,¹ and R. L. Myklebust¹

Errors Observed in Quantitative Ion Microprobe Analysis*

REFERENCE: Newbury, D. E., Heinrich, K. F. J., and Myklebust, R. L., "Errors Observed in Quantitative Ion Microprobe Analysis," *Surface Analysis Techniques for Metallurgical Applications, ASTM STP 596*, American Society for Testing and Materials, 1976, pp. 101-113.

ABSTRACT: Quantitative reduction of ion microprobe mass analyzer data has been performed with an empirical technique involving relative elemental sensitivity factors and with a physical model, the local thermodynamic equilibrium (LTE) model. A series of macroscopically well-characterized low alloy steels (National Bureau of Standards (NBS) Standard Reference Material 660 series) was analyzed with empirical relative sensitivity factors derived from one arbitrarily chosen alloy from the series. Relative errors of less than 50 percent were obtained in most cases, but several results were in error by 100 percent or more. The LTE model was used to analyze two multicomponent glasses. Relative errors of 200 percent were observed frequently, with some components consistently in error by an order of magnitude or more. The effect of differing reference data on LTE model calculations was tested. Different combinations of internal concentration standards and different metal/metal oxide ion ratios were employed. The calculated concentrations showed considerable dependence on the choice of reference data.

KEY WORDS: spectroscopy, ion microprobe mass analysis, local thermodynamic equilibrium model, quantitative analysis, secondary ion mass spectrometry, surface analysis, low alloy steels, errors

Quantitative analysis with the technique of secondary ion mass spectrometry (SIMS)/ion microprobe mass analysis (IMMA) is greatly complicated by the enormous range of relative sensitivity of the secondary ion signals (secondary ions per incident primary ion) for various elements. From pure elements bombarded with oxygen ions, the range of relative

* Certain copyrighted computer procedures are identified in this paper in order to adequately specify the experimental procedure. In no case does such identification imply recommendation or endorsement by the National Bureau of Standards.

¹ Metallurgist, section chief, and chemist, respectively, Analytical Chemistry Division, National Bureau of Standards, Washington, D. C. 20234.

sensitivity is approximately seven orders of magnitude from gold to aluminum.² A number of schemes based on physical principles for the quantitation of SIMS data have been proposed;³ of these, the local thermodynamic equilibrium (LTE) model has been most highly developed, and a computer program based on it has been distributed to at least 15 laboratories for analytical purposes.⁴ The LTE model makes the assumption that in the region of interaction, the primary ions and the atoms of the specimen material produce a dense plasma in thermal equilibrium. Analysis is performed with this model by deriving the thermodynamic parameters of the plasma, that is, the temperature and electron density (the internal standards) from certain known values of the specimen elemental composition, and the corresponding ion intensities, ionization potentials and the partition functions for those elements (see footnote 2). These parameters are then used to relate the ion intensities of the other observed species to composition. The data reduction program CARISMA (see footnote 4) employing the LTE model was employed in the present work.

A purely empirical approach to SIMS quantitation is possible through the use of relative elemental sensitivity factors,⁵ $S_{A/M}$,

$$S_{A/M} \equiv \frac{i_A/C_A F_A}{i_M/C_M F_M} \quad (1)$$

where

- i = signal intensity (photomultiplier current, scaler counts, etc.),
- C = atomic concentration,
- F = isotopic abundance of the species measured,
- A = element of interest, and
- M = matrix element.

A set of such factors for a particular matrix, such as an iron-based alloy, can be used to analyze a material with the same matrix. When the matrix is changed significantly, for example, from a semiconductor like silicon to an insulator such as silicon dioxide, a new set of sensitivity factors may be necessary. McHugh (see footnote 5) has described a procedure by which sensitivity factors can be adjusted for a change in the chemical state of the matrix.

² Anderson, C. A. in *Microprobe Analysis*, C. A. Anderson, Ed., Wiley, New York, 1973, pp. 531-553.

³ Schroerer, J. M. in *Secondary Ion Mass Spectrometry*, K. F. J. Heinrich and D. E. Newbury, Eds., NBS Special Publication 427, National Bureau of Standards, 1975.

⁴ Copyright of Applied Research Laboratories, Sunland, Calif.

⁵ McHugh, J. in *Secondary Ion Mass Spectrometry*, K. F. J. Heinrich and D. E. Newbury, Eds., NBS Special Publication 427, National Bureau of Standards, 1975.

To obtain an estimate of the accuracy which might be obtained from a given specimen with the application of these two approaches to quantitation, the empirical sensitivity factors and the LTE model, each technique was applied to the analysis of materials which had been well characterized by independent techniques. It is not the purpose of this work to compare the quantitation techniques against one another, since a meaningful comparison would necessitate a large number of tests on different materials. Rather, each technique has been applied to the analysis of a particular well-characterized material to determine the magnitude of errors which must be expected when poorly characterized materials are to be analyzed.

Analysis of Low Alloy Steels with Relative Sensitivity Factors

The low alloy steel series of Standard Reference Materials (SRM 661, 662, 663, 664, 665) offered by the National Bureau of Standards (NBS),⁶ was chosen to test the analysis approach of relative sensitivity factors. These steels contain approximately 94 atomic percent of iron, with the balance consisting of carbon, manganese, silicon, copper, nickel, chromium, vanadium, molybdenum, tungsten, cobalt, titanium, aluminum, niobium, tantalum, and zirconium (Table 1). The alloying elements range in concentration from less than 0.01 atomic percent to as high as 1.87 atomic percent. The macroscopic composition is certified on the basis of a variety of chemical analysis techniques, but it should be noted that these alloys are not certified for microhomogeneity. Preliminary studies with the electron probe microanalyzer (EPMA) indicated inhomogeneity on the micrometre scale for certain elements. Specimens were prepared by metallographic polishing. Prior to analysis, the area of interest was ion bombarded to remove any preparation artifacts. To minimize problems due to local inhomogeneity, the ion microprobe analyses were made with the ion beam scanning an area 250 μm square.

Analyses were carried out with a primary ion beam of $^{16}\text{O}_2^+$ at 18.5 keV (equivalent to $^{16}\text{O}^+$ at 9.25 keV) and a beam current of 5 nA. The chamber pressure was of the order of 10^{-4} Pa during analysis. In an initial study, the secondary ion signal was plotted as a function of certified concentrations for several elements (Figs. 1 to 8). For many elements, the secondary ion signal was found to be a simple linear function of composition over the range of compositions tested, for example, nickel, cobalt, chromium, silicon, and aluminum. These elements are expected to be contained in a single phase, either as a solute element in the iron matrix or as a precipitate. When the element is partitioned in two or more phases, deviation from a linear function is noted. For example, the curve for

⁶ *Catalog of Standard Reference Materials*, NBS Special Publication 260, National Bureau of Standards, available from the Office of Standard Reference Materials, Institute for Materials Research, Washington, D. C. 20234.

TABLE 1—Compositions in atomic percent of NBS SRM 660 series low alloy steels (derived from footnote 6) (selected elements used in present study).

Element	661	662	663	664	665
B	0.0025	0.013	0.0046	0.057	0.0007
Al	0.04	0.185	0.48	0.016	0.0014
Si	0.44	0.77	1.43	0.13	0.015
Ti	0.023	0.097	0.057	0.27	0.0007
V	0.012	0.044	0.33	0.11	0.0006
Cr	0.73	0.32	1.36	0.063	0.007
Mn	0.66	1.05	1.48	0.25	0.006
Co	0.028	0.28	0.044	0.14	0.006
Ni	1.87	0.56	0.30	0.13	0.038
Cu	0.036	0.44	0.08	0.21	0.004
Nb	0.013	0.17	0.029	0.088	...
Zr	0.005	0.12	0.029	0.04	...
Mo	0.11	0.035	0.017	0.28	0.003

NOTE—These steels also contain the following elements not considered in the present study: carbon, phosphorus, sulfur, tungsten, arsenic, tin, and tantalum. Additional species exist at the trace level.

manganese deviates at the highest concentration, probably due to the presence of manganese sulfide. For titanium and zirconium, large deviations from a linear function were observed throughout the composition range. Electron probe microanalysis shows that these elements are highly concentrated at discrete sites.

These steels were reanalyzed with data collection appropriate for analysis with relative sensitivity factors. For each specimen, the signals for the element of interest and the matrix element, iron, were measured in pairs to eliminate problems of drift in the primary beam current. Problems of mass peak interferences were considered for all peaks studied and

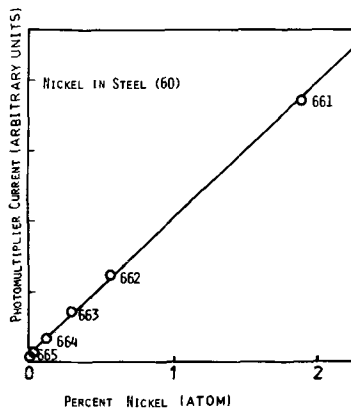


FIG. 1—Analytical working curve determined from SRM 660 series nickel in steel (60). Primary beam $^{16}\text{O}_2^+$ at 18.5 keV. Ordinate: photomultiplier current, arbitrary units.

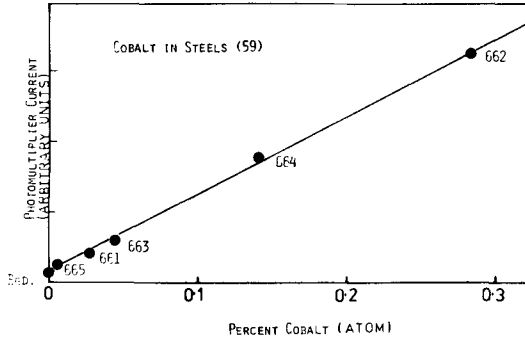


FIG. 2—Analytical working curve determined from SRM 660 series cobalt in steels (59). Primary beam $^{16}\text{O}_2^+$ at 18.5 keV. Ordinate: photomultiplier current, arbitrary units.

corrected as much as possible. For example, the ^{60}Ni peak was chosen in preference to ^{58}Ni since interference from ^{58}Fe occurs.

Steel SRM 662 was selected to serve as the reference material for the analysis of the other three materials (661, 663, and 664) since the elemental concentrations for SRM 662 fell in the middle of the range studied for most elements. The relative elemental sensitivity factors derived from SRM 662 are given in Table 2. These factors were used to reduce the ion intensity data for the other steels to concentration values.

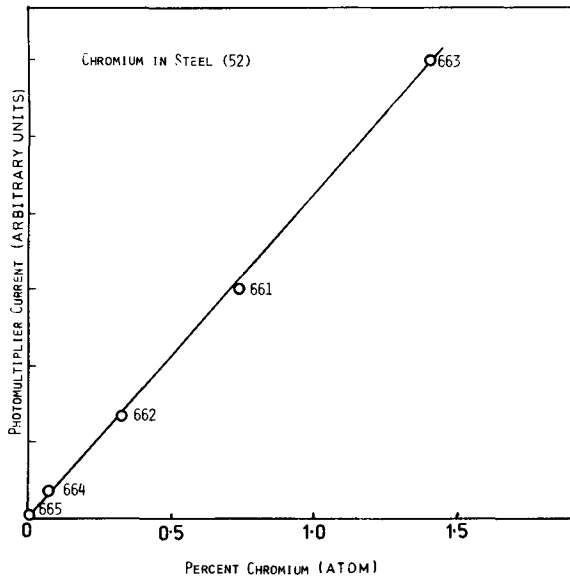


FIG. 3—Analytical working curve determined from SRM 660 series chromium in steel (52). Primary beam $^{16}\text{O}_2^+$ at 18.5 keV. Ordinate: photomultiplier current, arbitrary units.

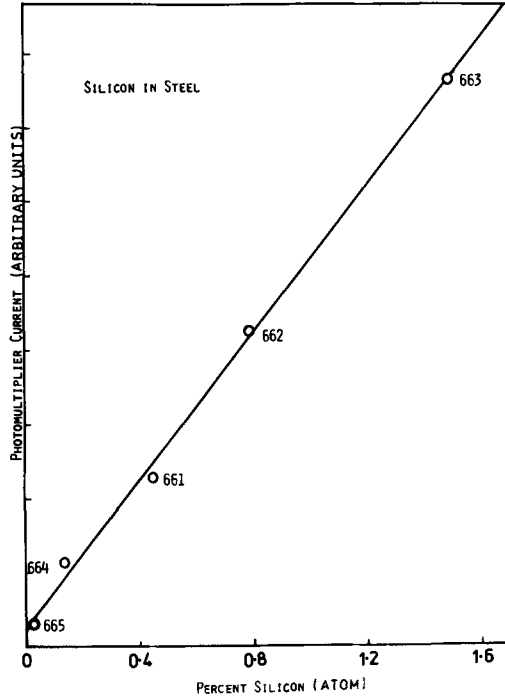


FIG. 4—Analytical working curves determined from SRM 660 series silicon in steel. Primary beam $^{16}\text{O}_2^+$ at 18.5 keV. Ordinate: photomultiplier current, arbitrary units.

The relative errors in these analyzed concentrations as compared to the certified concentrations are given in Table 2. Most of the relative errors generated in this fashion were less than 50 percent. However, relative errors in excess of 100 percent were observed in several cases. Two of these large relative errors (aluminum in SRM 664 and silicon in SRM 661) occur in spite of the fact that the intensity functions previously observed were linear. However, the zirconium/iron sensitivity factors show much less scatter than the previously determined intensity function. These anomalies may be related to the vacuum conditions or real inhomogeneities in the specimen and will be studied further. In general, the analysis by sensitivity factors is most successful in dilute solutions, as expected, since the analytical curve is a linear function with the sensitivity factor proportional to the slope of that curve. The errors that are observed in the present study indicate that even with well-characterized materials and careful technique, relative errors of 50 percent are to be expected. In more concentrated alloys, where the deviation from a linear analytical function is more severe, greater relative errors may be expected.

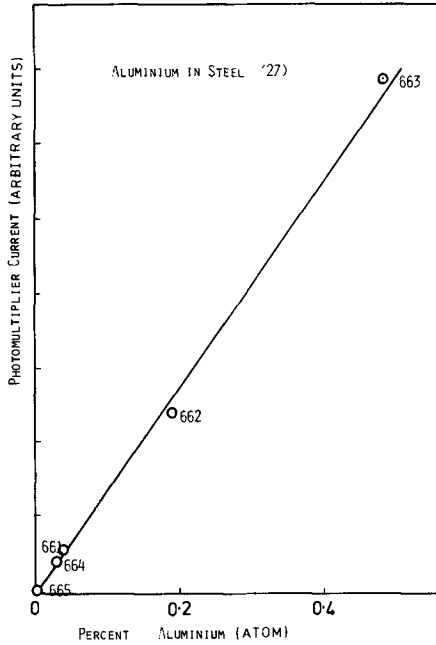


FIG. 5—Analytical working curve determined from SRM 660 series aluminum in steel (27). Primary beam $^{16}\text{O}_2^+$ at 18.5 keV. Ordinate: photomultiplier current, arbitrary units.

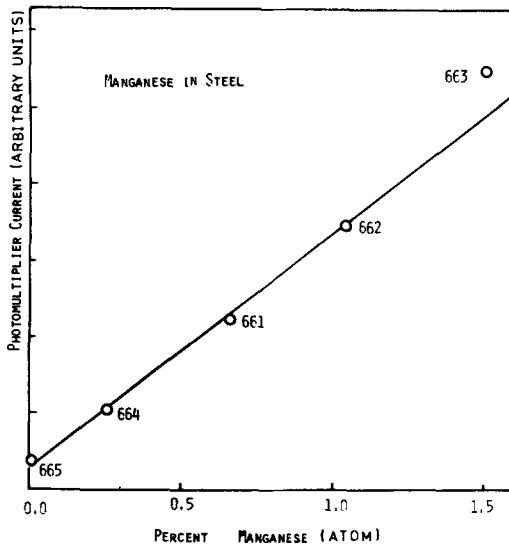


FIG. 6—Analytical working curve determined from SRM 660 series manganese in steel. Primary beam $^{16}\text{O}_2^+$ at 18.5 keV. Ordinate: photomultiplier current, arbitrary units.

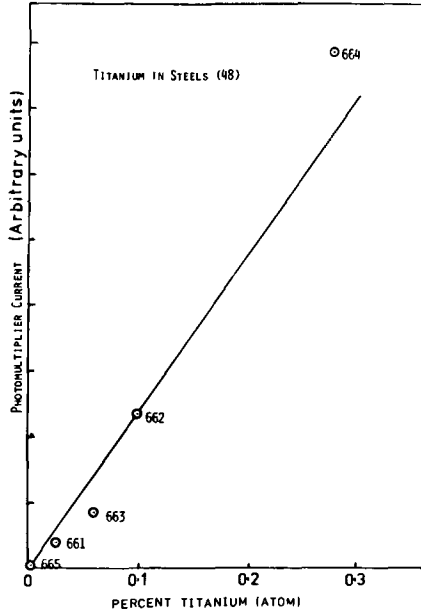


FIG. 7—Analytical working curve determined from SRM 660 series titanium in steels (48). Primary beam $^{16}\text{O}_2^+$ at 18.5 keV. Ordinate: photomultiplier current, arbitrary units.

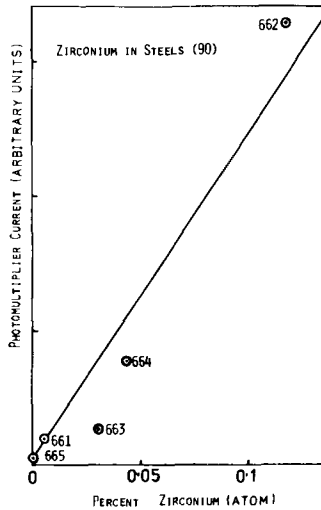


FIG. 8—Analytical working curve determined from SRM 660 series zirconium in steels (90). Primary beam $^{16}\text{O}_2^+$ at 18.5 keV. Ordinate: photomultiplier current, arbitrary units.

TABLE 2—Relative sensitivity factor analysis of low alloy steels.

Species	$S_{Al/Fe}$	Relative Error in Concentration, %		
	SRM 662	661	663	664
$^{11}B^+$	0.32	-19
$^{27}Al^+$	3.6	+41	+4.7	+105
$^{28}Si^+$	0.24	+105	+15	-8
$^{48}Ti^+$	5.8	-12	-41	-23
$^{51}V^+$	1.9	+65	+240	+44
$^{52}Cr^+$	2.1	+69	+61	+48
$^{55}Mn^+$	2.0	+17	-10	+19
$^{58}Co^+$	0.79	+9	+19	-8
$^{60}Ni^+$	0.51	-22	+22	+7
$^{63}Cu^+$	0.79	+18	+3	...
$^{93}Cb^+$	1.7	-20	-23	...
$^{90}Zr^+$	1.7	-31	-19	-18
$^{98}Mo^+$	0.38	+59

LTE Model Analysis of Glasses

To test the LTE model on well-characterized materials, two glasses of known composition were analyzed with the ion microprobe. These glasses had been prepared under carefully controlled conditions and analyzed by wet chemical techniques as well as the EPMA. The microspatial homogeneity of the glasses was also studied with the EPMA, and the composition was found to be constant within two percent relative concentration. These glasses contain six cations at levels of one atomic percent or greater totaling approximately 40 atomic percent, the balance being oxygen. Ion microprobe analyses of the glasses were obtained with a primary beam of $^{16}O^-$ at 21.5 keV, scanned over an area $100 \mu m$ square to eliminate any problems due to inhomogeneities. The specimens were polished by normal metallographic techniques and sputter coated with carbon for surface conductivity. Prior to analysis, the surface was ion eroded to a depth of at least 100 nm to remove any artifacts from specimen preparation.

Analysis with the LTE model was performed with option 3 of the CARISMA program (see footnote 4). In this scheme of analysis, the known concentration of at least two elements, the secondary ion intensity ratio of an element and its monoxide, and the total cation concentration (that is, the proportion of the specimen excluding oxygen) must be supplied. The "best fit" for the concentrations of the elements given as internal standards is calculated, and a final set of concentrations for all

elements is calculated with the thermodynamic parameters derived from the fitting procedure.

As a test of the analysis scheme, various combinations of two or three elemental concentrations were supplied to the program as internal standards, and the calculated concentrations for the other cations compared to the known values. The results are given in Tables 3 and 4. In addition, different element/monoxide combinations for analysis are compared for one glass in Table 5. In general, the calculated concentrations of "unknowns" in these glasses using the CARISMA program differ by a factor of two or three from the values obtained by wet analysis or EPMA methods. For certain elements, for example, zinc in glass K253, the calculated concentration is consistently low by about an order of magnitude. It is interesting to note the temperature and electron density obtained at the best fit of the internal standards. For glass K253 (Table 4), the temperatures fall in the range 1.4 to 1.7×10^4 K for all combinations of internal standards except (barium-cobalt-manganese) for which $T = 5.6 \times 10^3$. In this system, it is apparently important to include silicon as an internal standard. The accuracy of the calculated concentrations for the barium, cobalt, and manganese internal standards is very poor, as well as that for the calculated unknowns.

When different metal/metal oxide combinations are employed with the same set of internal standards (Table 5), the calculated temperature is about the same for barium/barium oxide and tantalum/tantalum oxide, but is much lower for silicon/silicon oxide (2.9×10^3 K compared to 1.7×10^4 K). The selection of the reference data can clearly have a strong influence on the result. It is, therefore, desirable to test several metal/oxide combinations as well as several combinations of internal standards for each analysis in order to notice unusual trends in the analysis.

Conclusions

In the well-characterized materials used in the present study, the analysis by the empirical method of relative sensitivity factors and the LTE physical model is semiquantitative at best. The value calculated for the concentration of an unknown varies by as much as a factor of 20 from the value determined by independent analysis. In applying the LTE model, the calculated results can depend strongly on the input parameters selected. Therefore, a given set of data should be analyzed with several selections of internal standards, if possible, to detect these effects. Even so, in the case of certain elements, the thermodynamic reference data are apparently not satisfactory, producing poor results. Doubtlessly, there are analytical situations where better performance can be achieved, but for any given system the performance realized in the present study is probably all that can be expected.

For improved quantitative analysis, advances must be made in several

TABLE 3—LTE model analysis of glass K251
(analyses with ten different combinations of internal standards).^a

Element	<i>a/o</i> Composition	1	2	3	4	5	6	7	8	9	10
²⁷ Al	2.1	4.6	4.3	4.6	2.1 ^b	4.3	4.3	2.8 ^b	2.9 ^b	4.1	2.3 ^b
²⁸ Si	21.6	24.3 ^b	27.8 ^b	24.4 ^b	29.7 ^b	27.8	27.9 ^b	28.3 ^b	29.4 ^b	26.7 ^b	31.8 ^b
¹³⁸ Ba	2.8	5.4	2.8 ^b	5.4	2.8	2.8 ^b	2.7 ^b	3.5 ^b	2.5	3.4 ^b	1.7
¹⁸¹ Ta	0.98	0.86	0.63	0.88 ^b	1.98	0.63	0.62	1.6	1.3 ^b	1.2 ^b	0.41
²⁰⁹ Pb	9.2	2.4 ^b	2.1	2.4	1.2	2.1 ^b	2.1 ^b	1.5	1.5	2.2	1.4 ^b
²⁰⁹ Bi	0.93	0.08	0.08	0.08	0.03	0.08	0.08	0.04	0.05	0.07	0.05
T, K		16 600	17 000	17 000	17 000	17 000	16 900	8 600	12 600	17 100	13 000
N _e , e ⁻ /cm ³		3.1 × 10 ²²	7.1 × 10 ²⁰	3.2 × 10 ²²	3 × 10 ²²	7.1 × 10 ¹⁹	7.7 × 10 ¹⁹	1.5 × 10 ¹⁴	1.9 × 10 ¹⁸	1.7 × 10 ²⁰	1.6 × 10 ²¹

^a Barium/barium oxide ratio was used.

^b Denotes internal standard.

TABLE 4—LTE model analysis of glass K253
(analyses with ten different combinations of internal standards).^a

Element	Composition	1	2	3	4	5	6	7	8	9	10
²⁸ Si	20.9	26.7 ^b	20.9 ^b	20.9 ^b	20.9 ^b	26.7	25.5 ^b	20.3 ^b	17.2 ^b	17.6 ^b	35.9
⁵⁵ Mn	3.7	2.5	3.0	3.0 ^b	3.0 ^b	2.5 ^b	2.6 ^b	3.1 ^b	3.0 ^b	3.0 ^b	0.39 ^b
⁵⁸ Co	1.0	0.48	0.49	0.47	0.47	0.48	0.49	0.49	0.45 ^b	0.45	0.11 ^b
⁶³ Cu	1.0	0.42	0.41	0.42	0.42	0.42	0.41	0.41	0.37	0.38 ^b	0.11
⁶⁷ Zn	3.9	0.38	0.38 ^b	0.37	0.38	0.38	0.38	0.38 ^b	0.26	0.29	0.47
¹³⁸ Ba	7.3	7.3 ^b	12.5	12.5	12.5	7.3 ^b	8.4 ^b	13.0	16.5	15.9	0.79 ^b
T, K		14 000	16 600	16 900	16 900	14 000	14 600	16 900	14 800	16 700	5 600
N _e , e ⁻ /cm ³		3.1 × 10 ¹⁹	1 × 10 ²⁰	5.7 × 10 ¹⁹	1.4 × 10 ²⁰	3 × 10 ²⁰	3.3 × 10 ²⁰	1 × 10 ²⁰	3.9 × 10 ²⁰	3.9 × 10 ²¹	1.1 × 10 ¹⁵

^a Barium/barium oxide ratio was used.

^b Denotes internal standard.

TABLE 5—*LTE model analysis of glass K251 effect of oxide choice.*

Element	<i>alo</i> Composition	1	2	3
²⁷ Al	2.1	4.3	2.3	4.5
²⁸ Si	21.6	27.8 ^a	26.7 ^a	27.8 ^a
¹³⁸ Ba	2.8	2.8 ^a	2.8 ^a	2.8 ^a
¹⁸¹ Ta	0.98	0.63	4.5	0.31
²⁰⁸ Pb	9.2	2.1	1.3	2.2
²⁰⁹ Bi	0.93	0.08	0.04	0.08
T, K		17 000	2 900	16 600
Ne, e ⁻ /cm ³		7.1 × 10 ¹⁹	2.3 × 10 ¹⁹	1.2 × 10 ²⁰
Oxide		BaO	SiO	TaO

^a Denotes internal standard.

areas. All quantitation techniques will benefit from improved instrumentation, particularly with regard to vacuum in the specimen region, since adsorbed species can affect secondary ion signals. The apparent variation in the analytical curves determined for the steels in two different experiments indicates that instrumental factors affecting the secondary ion intensities are significant. Quantitation techniques based on physical models will benefit greatly by improved understanding of the physical nature of the interaction of primary ions with the specimen. Finally, all models are dependent to some extent on measured physical parameters, for example, work functions, partition functions, etc., which are currently not well known under the ion bombardment conditions appropriate to SIMS studies.

Acknowledgments

The authors wish to acknowledge the glass preparation by D. H. Blackburn of the NBS Inorganic Glass Section.

T. A. Whatley,¹ D. J. Comaford,¹ John Colby,² and Paul Miller²

Small Area Depth Profiling with the Ion Microprobe

REFERENCE: Whatley, T. A., Comaford, D. J., Colby, John, and Miller, Paul, "Small Area Depth Profiling with the Ion Microprobe," *Surface Analysis Techniques for Metallurgical Applications, ASTM STP 596*, American Society for Testing and Materials, 1976, pp. 114–125.

ABSTRACT: The general technique of secondary ion mass spectrometry is now practiced in a number of instrumental variations. For certain problems, any one of these could usefully be employed. However, there is an important class of analytical problems that can be studied only with those instruments of the "small beam type," that is, an ion microprobe. These problems are those of characterizing fabricated devices, principally in the solid state electronics industry. Regions to be studied on these devices are frequently only a few tens of microns in lateral dimension.

The technique has been applied, for example, to the study of adjacent base and emitter regions of a single transistor. Detailed concentration distributions, showing the influence of phosphorus on diffusion of boron double implants were obtained from $25 \times 30\text{-}\mu\text{m}$ active areas of $100 \times 150\text{-}\mu\text{m}$ rastered regions. Even smaller areas can be successfully analyzed by utilizing reduced beam diameters and a correspondingly reduced raster size. With presently available instrumentation, the practical lower limit on analyzed area is about $4 \times 5\text{-}\mu\text{m}$ (using a 2/to $3\text{-}\mu\text{m}$ beam and a raster size of $12 \times 15\text{-}\mu\text{m}$). At this level, problems of beam diameter, sensitivity, and surface contamination all become limiting.

KEY WORDS: spectroscopy, surface analysis, ion microprobe, depth profiling, depth resolution, thin films, sputtering, craters, secondary ion mass spectroscopy

Inherent in the secondary ion mass spectroscopy (SIMS) technique is the possibility of determining concentration distributions as a function of the distance from the specimen surface, since the surface is eroded

¹ Manager, Probe Applications Laboratory, and senior spectroscopist, respectively, Applied Research Laboratories, Sunland, Calif. 91040.

² Members, Technical Staff, Bell Telephone Laboratories, Allentown, Pa. 18103.

continually during an analysis by the sputtering action of the primary beam. The various techniques for determining these distributions are called generally depth profiling. In order that measured signal intensities faithfully reflect actual concentration gradients, it is necessary that the information acquired be limited at any one instant to a narrow zone of depth and not be from a range of depths simultaneously [1].³ In practical terms, this requires that the crater created by ion beam sputtering have a flat bottom parallel to the original specimen surface.

A normally focused ion beam has an approximate Gaussian current density profile and is totally unsuitable as such for depth profiling. Several techniques have been developed to obtain a zone of uniform sputtering; the beam can be defocused to a very large diameter [2,3], or it can be rastered over a rectangular area. In both cases, there are still crater wall effects, unless the crater is so wide that the crater perimeter is outside the acceptance angle of the secondary mass spectrometer. This enables certain large beam instruments to achieve good depth resolution. The direct imaging type of instrument can utilize a mechanical aperture at a secondary ion focal plane to reject ions from the crater walls [4]. The ion microprobe mass analyzer (IMMA) [5] uses beam rastering with signal gating to reject signals from all but the central portion of a rectangular crater. We call this technique electronic aperturing.

In all depth profiling measurements, the requirement to sputter at a uniform rate over the area from which information is acquired is critically important to the quality of the experimental results. For "small area" depth profiling it can be assumed that one is working at or near the capability limits of the analytical instrumentation in order to compress the beam and raster dimensions to be comparable to the dimensions of "small" specimens. It is not surprising that instrumental conditions become more limiting, and it is appropriate to examine the practical limitations of the technique in some detail.

Small is, of course, a relative term, but, in terms of presently known SIMS apparatus [6], the IMMA with a probe diameter capability of $2\ \mu\text{m}$ is clearly a small-beam instrument. This probe diameter makes it possible to carry out depth profiles on specimens having lateral dimensions of only a few micrometres, without disturbing adjacent areas. Such dimensions are common in microcircuits where individual elements are spaced typically 10 to 15 μm apart. Sufficiently limiting the area of beam impingement allows, for instance, separate determinations of concentration profiles in base, emitter, and collector regions of a single transistor.

Electronic Aperture Technique

The purpose of electronic aperturing (beam rastering with signal gating) is to gain improved depth resolution by rejection of that portion of the

³ The italic numbers in brackets refer to the list of references appended to this paper.

sputtered ion intensity that originates from the sloping sides of the sputter crater. The technique is shown schematically in Fig. 1. The upper part of the figure indicates the path followed by the beam on the specimen surface. This rastering motion of the ion beam erodes in the specimen a rectangular crater with a sloping perimeter about one beam diameter wide. For a typical sweep length of five beam diameters, the central flat region is about three diameters wide. The line spacing is denser than shown; 50 lines per frame are normally used so that adjacent line sweeps overlap. Even so, it is necessary to avoid synchronization of the sweeps and of the beam flyback if a smooth surface is to be obtained. This randomization is assured when the raster (as observed on an oscilloscope) appears to "roll" continuously.

Electronic aperturing results if the ion detection system is activated only when the rastering beam is impacting on the flat bottom of the crater. Preset voltage levels on both the vertical and horizontal beam sweep drivers trigger gating pulses to the high speed pulse counting system, corresponding to beam positions on the specimen surface indicated by the central rectangle in the raster diagram.

Ion counts resulting from successive beam traverses through the aperture region are accumulated for a fixed period of time (typically 10 s) and then output via a teletype or multichannel scaler. This gives a series of discrete points from which the intensity profile can be constructed. At the same time, an analog trace of ion intensity can be recorded, using a rate-metered output from the counting system. A frame rate of ten per second, with a recorder time constant of 0.1 s, gives a smoothed trace. Note that this places stringent requirements on the gating response of the counting system. At 50 lines/frame and 10 frames/s, the gated-on time per sweep is less than 1 ms. Excessively slow response of this system would result in shifting the sampled region out of the flat region.

Beam Size/Raster Size Considerations

A focused ion beam is usually described as having a Gaussian current density distribution. This can be shown to be at least approximately true

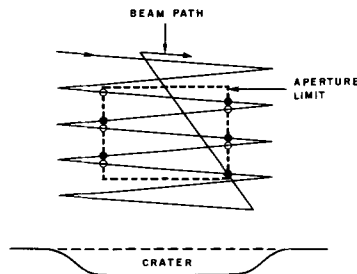


FIG. 1—Beam rastering with signal gating to create an electronic aperture.

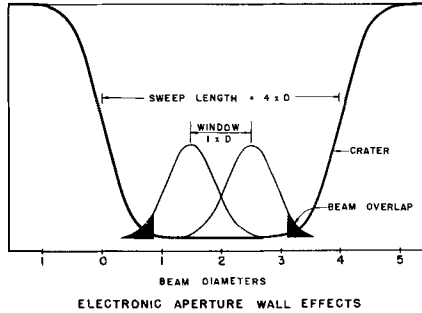


FIG. 2—Calculated crater shape resulting from a four-diameter sweep of a Gaussian beam.

by differentiating the current response obtained when the beam is scanned across an abrupt interface. The working relationships between beam size, raster size, and electronic aperture size are shown in Fig. 2, where the assumption is made that the beam current density profile is describable indeed by a normal error curve

$$I_x = I_{\max} e^{-x^2/2}$$

The illustration is shown for a sweep length of four beam diameters where the beam diameter is described, according to our convention, as the 10 to 90 percent excursion of beam current in an edge scan. For the normal curve, this corresponds to 2.56σ and is about 9 percent greater than the full width at half-maximum (FWHM) definition.

The crater resulting from sweeping this beam four diameters will be flat, to within 1 percent of the maximum depth, for a width of 2.3 beam diameters. If an aperture dimension of one diameter is chosen, the trailing edge of the beam profile will extend beyond the flat region (1 percent definition) when the beam is at the extreme excursion permitted by the selected aperture. The overlap is shown by the cross-hatched area in the superimposed beam profile and amounts to 12 percent of the instantaneous current at this position of the sweep. This can cause significant tailing effects when profiling through an abrupt interface. Some reduction in overlap would result if a narrower window were used, but this rapidly becomes self defeating because of loss of detection sensitivity. For a 1 by 1 aperture in a 4 by 4 raster, the signal intensity is reduced from that of the full beam by the area ratio, or to about 7 percent of the nonapertured signal. A better solution is to use a somewhat larger raster to beam size ratio. This also must be limited because, for a given beam current, sputter rate decreases as the square of sweep length. In practice, we have found that a raster width of five diameters is a good compromise between edge rejection, sputter rate, and sensitivity. For such a raster,

the sputter rate is approximately 2 percent of that of a static beam, and a 1 by 1 aperture is equivalent to a counting efficiency of 4 percent of the static beam.

Depth Resolution Measurement

The calculation of crater shapes by assuming a Gaussian beam is useful for visualizing the relative size relationships. A practical test of the behavior of real beams is to perform a depth profile through a layered thin film structure. A well-constructed structure ideally should show abrupt transitions at each interface. In practice, the transitions will always be more or less gradual due to beam nonuniformity, crater wall effects, and mixing effects. The depth over which an otherwise sharp interface is smeared provides a means of experimentally measuring depth resolution.

Figure 3 shows the results of profiling through 1040 Å of chromium deposited on a smooth silicon wafer. The indicated intensities are those of SiO^+ ($m/e = 44$) and $^{50}\text{Cr}^+$, measured in the fast peak switching mode during the run. This gives an essentially simultaneous measure of the two layer materials. This specimen was selected to demonstrate depth resolution because both layers were of high purity and because interferometry and electron microscopic observations indicated that the chromium film was smooth and coherent.

Further, interferometric measurement of crater depths indicated that

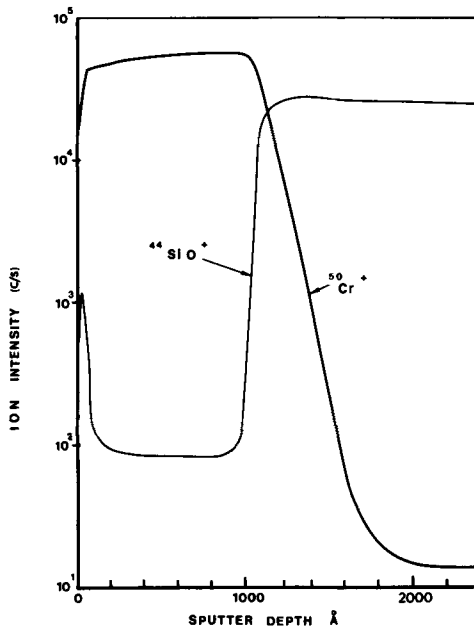


FIG. 3—Profile through a layer of chromium on silicon.

sputter rates for the two layer materials were approximately equal. Thus, it was not necessary to ascribe separate sputter rates to the two layer materials, nor to the transition composition at the interface.

The most significant feature of the profiles is the slowness with which the chromium intensity decreases; in Fig. 3, at a depth of 200 Å past the interface, chromium is still present in a sufficient amount to give a secondary ion intensity equal to 1 percent of that of pure chromium. Part of this is matrix enhancement of the ionization efficiency for chromium which is higher in silicon than in chromium. The steady exponential decrease of the signal suggests that the slope of the trailing edge of the interface could provide an easy quantitative measure of depth resolution. This can be usefully expressed as a characteristic distance, $L_{1/2}$, which is the depth to which sputtering must proceed for the measured intensity to decrease by a factor of two. For the example shown, this distance is 52 Å. The conditions of this experiment were such as to minimize this value: low primary impact energy (4.25 keV) and a large raster size/beam size ratio (>10). Before discussing the effects of these two variables on depth resolution, it should be noted that the leading edge in such an interface profile (increase in silicon ion intensity, in this case) is not a very good test of depth resolution; even a static spot will produce a fairly abrupt rising profile at an interface. The trailing edge, on the other hand, exhibits more readily all the effects of nonuniform cratering, knock on, redeposition, etc., and is a rigorous test of practical depth resolution.

Profile Resolution As a Function of Raster Size

The assumption of a Gaussian beam led to the conclusion that at five beam diameters, crater wall effects should be quite small. To test this in practice, the chromium-silicon specimen was profiled in a series of experiments where the beam diameter was kept constant, but the raster size was varied. The effective depth resolution attained is shown in Fig. 4 as a function of the raster size. Nearly as predicted, the resolution reaches a minimum value (about 130 Å) at about five beam diameters and does not improve significantly with larger raster dimensions. These experiments were performed with a primary beam of O^{2+} , impacting the specimen at 18.5 keV.

Kinetic Energy Effects

It has been demonstrated [1,7] that a knock on or subatomic mixing effect degrades depth resolution and that it is a function of the energy of the primary beam. A series of profiles through the same chromium-silicon interface were run at varying kilovolts, all with raster widths well above the five diameter limit at which crater wall effects can alter the profiles. Depth resolution as a function of kinetic energy of the primary ion is shown in Fig. 5. There is a linear relationship between the resolution

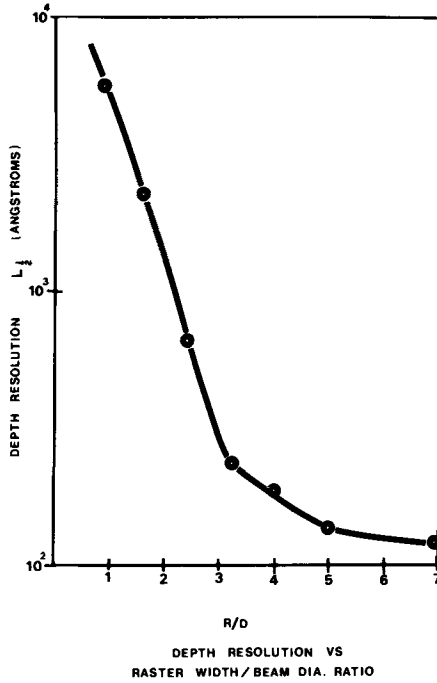


FIG. 4—Depth resolution as a function of raster size (raster width expressed in beam diameters).

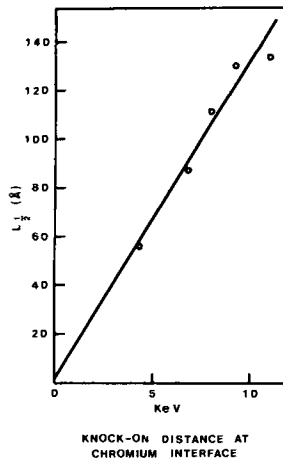


FIG. 5—Depth resolution as a function of primary ion energy.

parameter, expressed as a half distance, and primary beam energy. In most of our work we have chosen to operate at 20 kV with $^{32}\text{O}_2^+$. After subtracting the specimen bias potential of 1.5 kV, dividing the energy between the two oxygen atoms gives 9.25 keV, for which $L_{1/2}$ is 130 Å.

Effects of Knock On on Boron Profiles

While knock on is quite apparent in profiling an abrupt interface, its disturbance of a gradual distribution is certain to be less apparent [1]. A boron implanted silicon specimen that had been well characterized previously [8] was profiled for boron at primary beam energies ranging from 4.25 to 10.5 keV. The results of five profiles are shown in Fig. 6. They coincide within a band width of 150 Å. Within that band, there was no particular order with respect to kilovolts. The experimental scatter due to other factors apparently washes out the effect of knock on in the case of gradual gradients. This means that in most measurements one is free to operate at higher beam energies, where ion beam focus properties are superior.

Applications of Small Area Profiling

Some practical applications of small area profiling have included determination of concentration profiles in adjacent base and emitter

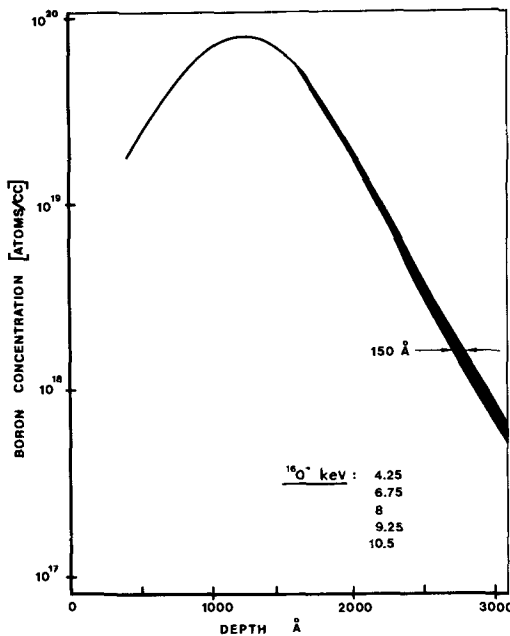


FIG. 6—Boron implant profiles as a function of primary beam energy.

region of the same transistor. One example is shown in Fig. 7. Using a less than ideal beam, an area 100 by 150 μm was rastered, with the sampled region adjusted by means of electronic aperturing to be 20 by 25 μm .

In the base region, the profile shows the expected boron distribution resulting from a double implant. Profiles of the adjacent emitter region are shown in Fig. 8. The presence of phosphorus in the emitter alters the boron distribution, and the electrical performance of the devices could be correlated to the phosphorus concentration at the junctions.

An example of a defect analysis requiring multiple profiles in a single device is illustrated in Fig. 9. This was a sample of a transistor that was being used in large numbers on a spacecraft. Long life was a requirement, but the devices were exhibiting gain degradation with time. The craters of various sizes are the results of measurements at junction, emitter, and base regions seeking impurities and profiling for boron distributions.

Lower Limits On Profile Area

The examples given previously have not involved working at the lowest attainable beam size, mainly because those particular problems did not require it. The lowest practical probe size attainable with the IMMA is 2 μm . Using the five diameter criterion for good edge rejection, it should be possible to raster an area 10 μm wide and use electronic aperturing to sample a central region about 3 by 3 μm .

To check this capability, profiles using those probe conditions were run on the same well-characterized boron implant specimen that was used in the earlier experiments (Fig. 6 and Ref 8). Figure 10 is a plot of the data obtained in one such profile. Experimental conditions were: probe

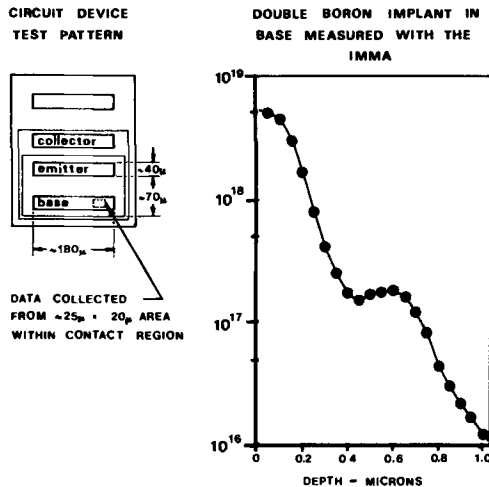


FIG. 7—Profile of boron double implant in base area of test transistor.

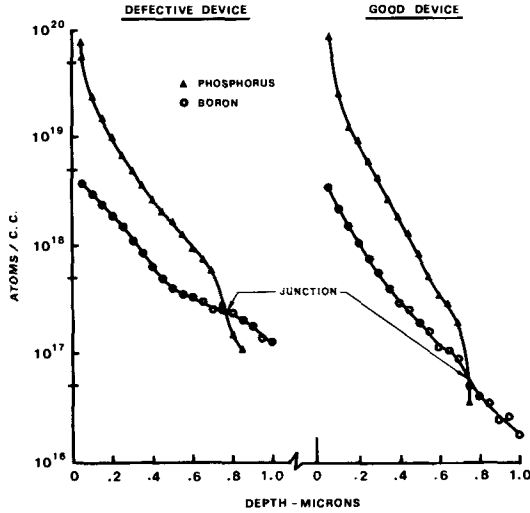


FIG. 8—Boron and phosphorus profiles in adjacent emitter regions of test transistor.

diameter, $2 \mu\text{m}$; probe current, $2 \times 10^{-10}\text{A}$; $^{32}\text{O}^+$ at 20 kV; 4 percent electronic aperture. The profile is close to that obtained in the large beam experiments in shape, but the concentration can be followed down only to a level of about 5×10^{17} atoms/cm³, which is about two orders of magnitude higher than that reported earlier [1] for large beam work on the

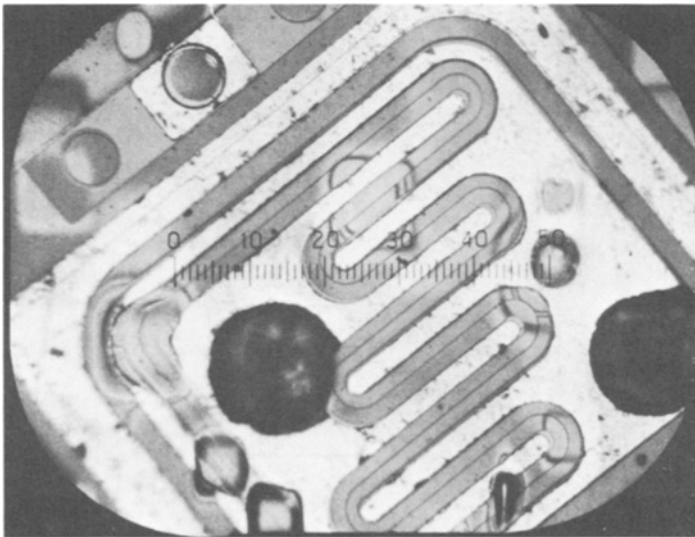


FIG. 9—Multiple sampled regions on a single defective transistor.

same specimens. The reason is clear; looking at the right hand ordinate, note that the count rates are extremely small (28 counts/s at the maximum concentration). At lower concentrations each point represents 100 counting time. At the end of the run, 20 counts per interval were recorded for a counting statistics standard deviation of about 20 percent. Counting longer would not improve the situation much, since the boron concentration is also changing by nearly 50 percent during 100 of sputtering at 1.5 Å/s. The practical detection limit for boron in silicon, for these beam conditions, is therefore about 5×10^{17} atoms/cm³.

Conclusion

There is a simple trade-off between detection sensitivity and the ability to sample small volumes. This is illustrated in Fig. 11, which is a plot of practical levels to which some boron implant profiles were extended, using two typical probe sizes to represent the large and small extremes normally used in the IMMA. Because current density in the focused probe is nominally independent of diameter and because a constant ratio of sweep length to beam diameter is used, there is a square dependence between probe diameter and sampled volume. Approximately ten times reduction in probe diameter is accompanied by a 100-fold reduction in probe current. This results in about two orders of magnitude loss in detection sensitivity at the lower extreme. The choice of where to operate along this line is clear; one uses a probe size small enough to do the job, but no smaller.

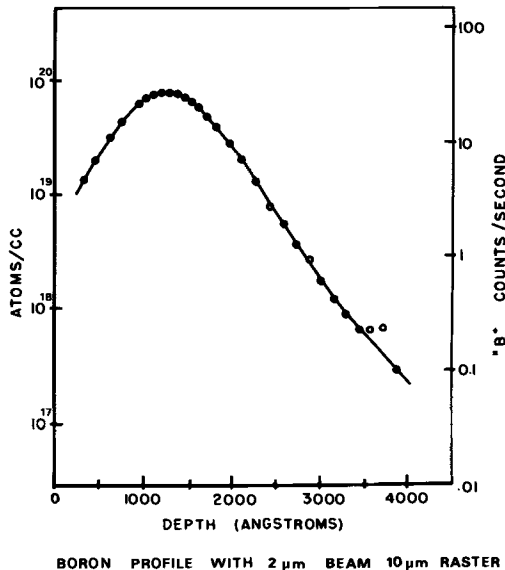


FIG. 10—Boron profile using a primary beam of 2 μm diameter.

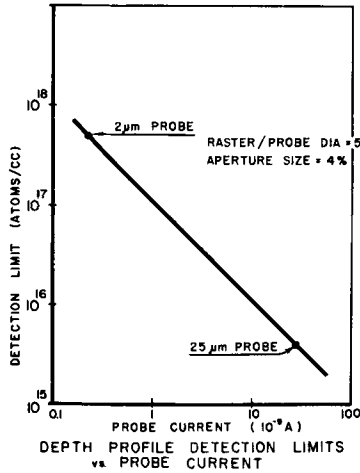


FIG. 11—Trade-off between probe current and detection limit.

Summing up, the principal difference in the results between what we have chosen to call small depth profiling and the results of large beam experiments is one of sensitivity, because of the different amounts of specimen that are consumed in the different cases. Current densities and, therefore, sputter rates are the same. Relative sizes of beam and raster are usually the same, so depth resolution is no different. The choice to apply small area profiling techniques is then dictated only by considerations of specimen size, and especially where it is desirable to sample adjacent locations on a single specimen.

References

- [1] Anderson, C. A., Colby, John, Dobrott, Robert, Whatley, T. A., and Comaford, D. J., "Fundamental Relationships Governing Depth Resolution in the Ion Probe Mass Analyzer," Paper No. 350, Abstracts of Pittsburgh Conference on Analytical Chemistry and Spectroscopy, Cleveland, 1974.
- [2] Guthrie, J. W. and Blewer, R. S., *Review of Scientific Instruments*, Vol. 43, 1972, p. 654.
- [3] Blewer, R. S. and Guthrie, J. W., *Surface Science*, Vol. 32, 1972, p. 743.
- [4] Castaing, R. and Slodzian, G., *Journal de Microscopie*, Vol. 1, 1972, p. 395.
- [5] Whatley, T. A., Slack, C. B., and Davidson, E., *Proceedings, Sixth International Conference on X-Ray Optics and Microanalysis*, Osaka, 1971.
- [6] Evans, C. A., Jr., *Analytical Chemistry*, Vol. 44, 1972, p. 67A.
- [7] McHugh, J. A., *Radiation Effects*, Vol. 21, 1974, p. 209.
- [8] Dobrott, R. D., Schwettman, F. N., and Prince, J. L., *Proceedings, Eighth National Conference on Electron Probe Analysis*, Paper No. 10, New Orleans, 1973.

R. D. Fralick,¹ H. J. Roden,¹ and J. R. Hinthorne¹

Analysis of Solids Using a Quadrupole Mass Filter

REFERENCE: Fralick, R. D., Roden, H. J., and Hinthorne, J. R., "Analysis of Solids Using a Quadrupole Mass Filter," *Surface Analysis Techniques for Metallurgical Applications*, ASTM STP 596, American Society for Testing and Materials, 1976, pp. 126–139.

ABSTRACT: The quadrupole mass analyzer for solids (QMAS) is ideally suited for multielement analysis because of the rapid scanning capabilities of its quadrupole mass filter, the high sensitivity inherent in the secondary ion mass spectroscopy (SIMS) technique, and an instrumental configuration which produces abundance sensitivities in excess of 10^5 to 1. These capabilities allow the elemental composition of solid specimens to be readily measured and permit the detection of contaminants and dopants on the surface as well as in the bulk of a specimen to be determined. A typical mass survey of a silicon specimen is shown and some of its features are discussed. Because of the correlation between the time of sputtering and the depth eroded into a specimen, multiple element in-depth profiles are also readily measured with QMAS. In-depth distributions of boron and phosphorus, both implanted and diffused into silicon, have been determined and are discussed. The effects of different specimen treatment histories are found to be reflected in the depth profiles obtained.

In addition to depth profiling, the instrument has been used successfully for isotope ratioing. Work done with the lead isotopes indicates that the accuracy of the measured ratios is limited only by counting statistics. The accuracy of these analyses verifies that the instrument can be used routinely to analyze insulators. These studies also illustrate that spectral ion interferences can often be successfully treated by peak stripping techniques. In the same study, the analytical problems associated with possible mass discrimination and the ability to obtain quantitative elemental analyses have been investigated and the results compared with the ion microprobe mass analyzer (IMMA).

KEY WORDS: spectroscopy, analyzers, quadrupole mass filter, solids mass spectrometer, depth profiling, lead age dating, sputtering, isotope ratioing

¹ Senior scientist, scientist, and research scientist, respectively, Hasler Research Center, Applied Research Laboratories, Goleta, Calif. 93017.

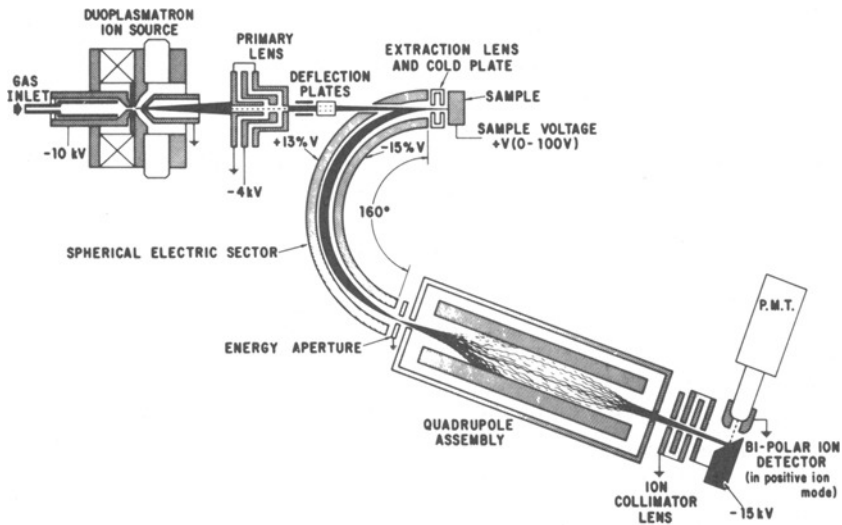


FIG. 1—Instrumental configuration of QMAS.

New and less complex instrumentation using a quadrupole mass filter is now available for doing secondary ion mass spectroscopy (SIMS). One such instrument, the quadrupole mass analyzer for solids (QMAS), has been uniquely configured to permit it to perform many different analytical tasks.

Instrument Description

The instrumental configuration of QMAS is shown in Fig. 1. A detailed description of the various components of the instrument can be found elsewhere [1].² It is appropriate, however, to mention that in addition to those components shown in the figure and discussed in the referenced paper, provisions have also been made to allow the specimen to be both viewed and manipulated during analysis. Viewing is made possible by an optional optical microscope having normal incidence and designed to operate at a nominal magnification of 200 with a field of view of approximately 1000 μm . The specimen stage is also optional and is simple in concept. The *X-Y* motions are controlled by precision micrometers while the *Z* translation and rotation are permitted through an O-ring seal.

² The italic numbers in brackets refer to the list of references appended to this paper.

With translation only, a 1-in.-diameter specimen area can be positioned under the beam. Combining translation and rotation permits a 2-in.-diameter surface to be covered. Incorporation of both these features is important for those types of analyses where particular areas of a specimen are of interest. By having these features as built-in options, analysis of such specimens is greatly simplified.

Because of the rapid scanning capabilities of the quadrupole mass filter and the high sensitivity inherent in the SIMS technique, QMAS is suited ideally for multielement analyses. These two features together with high abundance sensitivity, or lack of cross talk between adjacent mass peaks, also permit meaningful trace analyses to be performed. The high abundance sensitivity of this instrumental configuration is clearly demonstrated in Fig. 2. As can be seen in this spectrum of an aluminum alloy, the peak to valley measured between 27 and 26 1/2 atomic mass units (amu) is in excess of $10^6:1$. This indicates that for elements having comparable sensitivities to magnesium in aluminum, detection limits at the parts per million atomic (ppma) level should be readily achievable even immediately adjacent to a major isotopic concentration.

Because of the three properties just described, QMAS is a powerful tool for specimen survey work. Surveys can either be accomplished by looking at the detector output rapidly on a near flicker-free oscilloscope trace as the quadrupole is swept or on a more sensitive readout device such as a logarithmic amplifier and a *x-y* recorder. A typical example of the latter is shown in Fig. 3, where a silicon specimen was analyzed for trace elements. It is of particular interest in this specimen to note the presence of a known dopant, ^{11}B , and the low level $^{12}\text{C}^+$ peak which is also detected. We would suspect that the carbon is actually present in the specimen rather than being due to vacuum system hydrocarbons, because the instrument is ion pumped with a cryopump and a liquid nitrogen (LN^2) cold plate is located directly above the specimen surface. Also, carbon levels lower than those shown here have been observed in other specimens.

Depth Profiling

With the appropriate electronic rastering capabilities of the instrument and the ability to correlate time of sputtering to the depth eroded into a specimen, multiple element in-depth profiles are readily measured. One such profile is shown in Fig. 4. This specimen was prepared by implanting a silicon wafer with ^{11}B at 80 keV. The specimen was then sputtered at an approximate rate of 2 Å/s and the depth profile was obtained. During analysis several mass peaks were monitored, but, since they were constant in time, only the boron profile is shown. It is interesting to note two features of the depth profile measured. First, because no special specimen preparation is required, that is, no specimen precleaning is

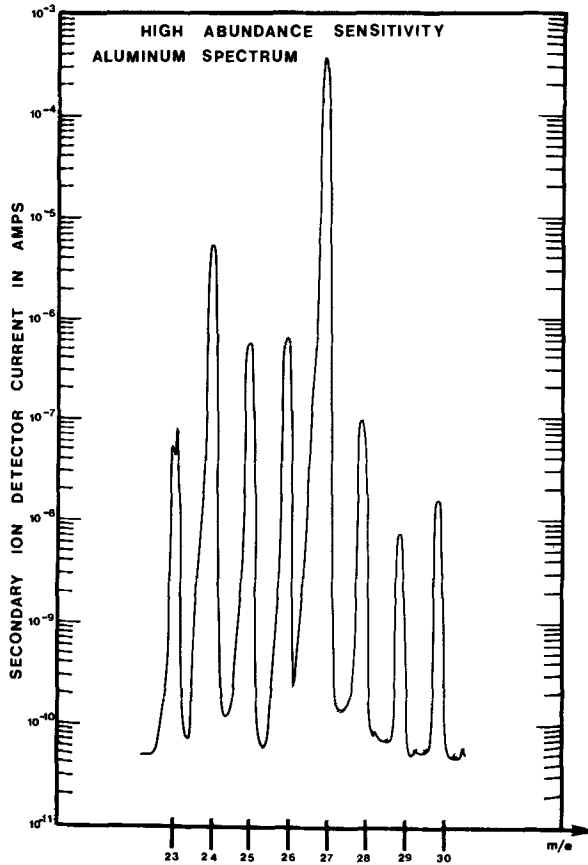


FIG. 2.—Measurement of abundance sensitivity on an aluminum specimen. Peak to valley between 27 and 26 $1/2$ amu is 2×10^6 to 1.

done, the increased boron concentration at the specimen surface is clearly shown. Second, in this analog profile a ratio of 10^4 :1 was measured between the peak and the lowest boron concentration. The lower level measured is just the analog background of the instrument; with a digital readout, this level should be lowered at least one order of magnitude.

In addition to the simple implant profile just described, other depth profiles reflecting more complicated histories have been measured with QMAS. Typical of such studies is the following set of depth profiles.³ First, a silicon specimen diffused with phosphorus at a total dose, Q , of 9.19×10^{15} atoms/cm² and then annealed at 900°C for 15 min was depth

³ Colby, J. W. and Miller, P., Bell Laboratories, Allentown, Pa., private communication.

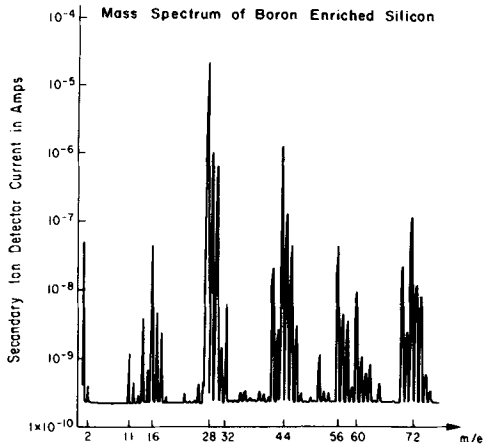


FIG. 3—Mass spectrum survey of a boron enriched silicon specimen.

profiled, yielding the results shown in Fig. 5. A second silicon specimen implanted with 50-keV boron and annealed as before was also measured and the profile obtained is shown in Fig. 6. The boron concentration is found to peak at approximately 1800 Å and the total integrated dose, Q_{\bullet} , is measured to be 1.0×10^{14} atoms/cm². In the third specimen the preceding two processes were repeated. The silicon was first diffused with phosphorus to the levels previously determined, implanted with boron at 50 keV, and then annealed at 900°C for 15 min. The depth profile obtained on this specimen is shown in Fig. 7. While the total dose of both the phosphorus and boron are unchanged, we observe that the boron concentration profile has been appreciably altered during the annealing process, and the peak has moved approximately 270 Å towards the surface. This so called "emitter suck" effect reported by Colby et al [2] appears to be related to the phosphorus in-depth concentration. Figure 8 shows a specimen having undergone nearly the same treatment history as before except that the phosphorus has been diffused further into the specimen and is more uniformly distributed in depth. In the absence of a sharp phosphorus gradient, the location of the peak boron concentration is unchanged during the annealing process. These results, which agree qualitatively with the earlier studies [3] done on similar specimens with the Applied Research Laboratories (ARL) ion microprobe mass analyzer (IMMA) and the Cameca Instruments direct-imaging mass analyzer (DIMA), demonstrate the present capability of QMAS for obtaining accurate depth profiles.

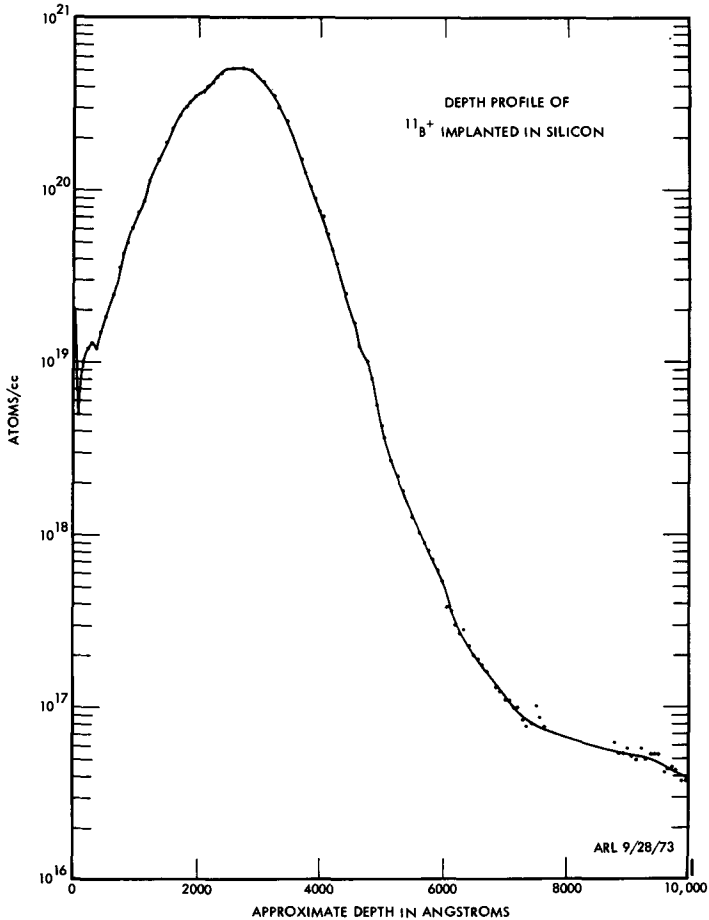


FIG. 4—Depth profile of $^{11}\text{B}^+$ implanted in silicon at 80 keV.

Depth Resolution

Because of the interest in in-depth profiling, it is important to know the depth resolution inherent in the sputtering technique. To determine the depth resolution achievable with the instrument, a well-characterized specimen has been analyzed. This specimen, part of the round robin set of specimens prepared for cross comparison of instruments for the Tarrytown Workshop [4], consists of a 50 Å thick $^{31}\text{P}^+$ enriched tantalum pentoxide (Ta_2O_5) layer buried 500 Å in pure Ta_2O_5 . The thickness of the measured $^{31}\text{P}^+$ layer compared to the known thickness of 50 Å is a measure of the depth resolution of the instrument. A typical $^{31}\text{P}^+$ profile measured in this specimen with QMAS is shown in Fig. 9. Under

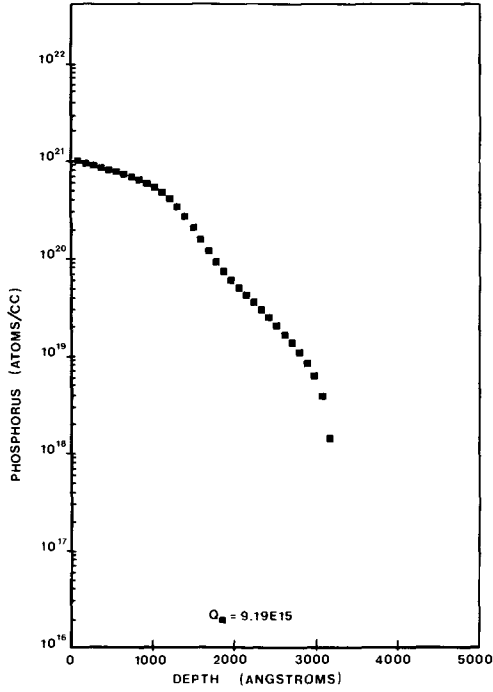


FIG. 5—Depth profile of phosphorus diffused silicon. Total phosphorus dose, Q_p , is 9.19×10^{15} atoms/cm².

bombarding conditions of 8 keV with a negative oxygen beam, the phosphorus layer is found to have a full width half maximum (FWHM) of 150 Å. This same specimen was also run on the IMMA [5]. The results of this work are shown in Fig. 10. Comparison between the two would indicate that these results are in excellent agreement. (Comparison should be made between the QMAS 8 keV, $^{16}\text{O}^-$ data, and the IMMA $^{28}\text{N}_2^+$, 15-keV data, since in the latter each nitrogen atom will have about one half the bombardment energy of the molecule or 7.5 keV.) Furthermore, based upon the IMMA results at lower bombardment energies, a FWHM depth resolution of between 50 to 100 Å should be achievable with the instrument.

Isotope Ratio Measurement

In addition to depth profiling, QMAS has been successfully used to measure isotope ratios. Under a National Aeronautics and Space Administration (NASA) study grant [6], the possibility of using QMAS as a remote sensor for the determination of lead ages on planetary missions

was investigated. Earlier results [7] obtained with the IMMA have shown that sputtered ion analysis can be an effective tool for the determination of $^{207}\text{Pb}/^{206}\text{Pb}$ crystallization ages for mineral accessory phases which concentrate uranium at the time of crystallization. It was suggested that QMAS, because of its simplicity and potential for miniaturization, would be a natural package for determining such ages on our neighboring planets as part of a soft lander package provided it could be demonstrated that the instrumental accuracy, precision, and sensitivity were such as to permit meaningful lead isotope ratio determinations to be made.

The experimental configuration used for this determination is shown in Fig. 11. The controlling element in the system is the multichannel analyzer (MCA). It serves two primary functions. First it acts as the primary data recording element when operated in the multiscaling mode. Second, by coupling it together with the appropriate associated electronics, the MCA is used to control the mass scan of the quadrupole. Thus the data recording system and the instrumental control functions both reside in the MCA, and we are assured that proper synchronization is maintained between the two. By using the MCA and sweeping rapidly and repetitively, data

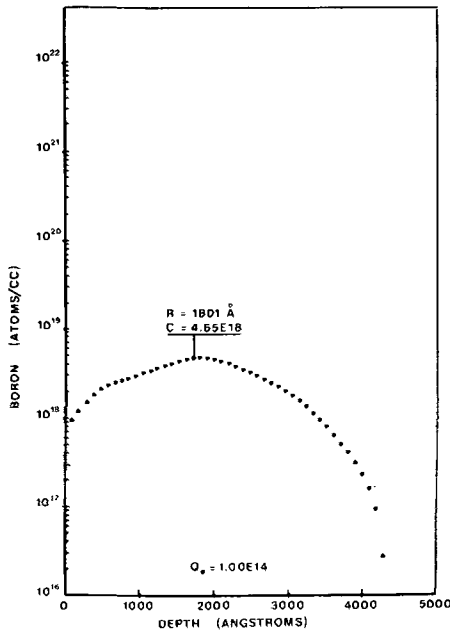


FIG. 6—Depth profile of 50 keV boron implant in silicon. Total boron dose, Q_0 , is 1×10^{14} atoms/cm², C is the peak concentration in atoms/cm³, and R is the depth into the specimen of the peak concentration.

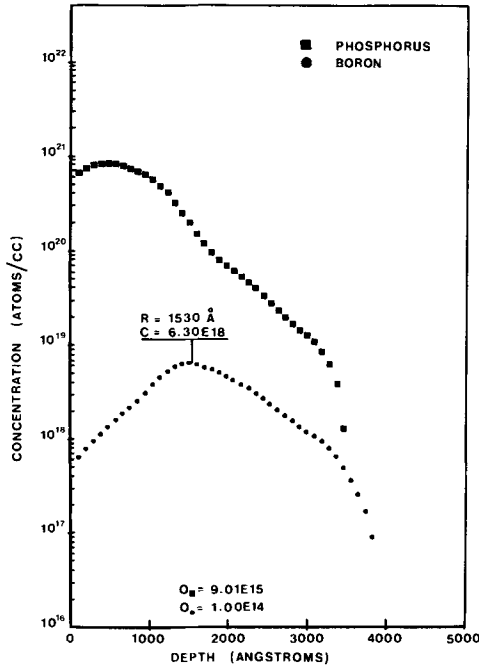


FIG. 7—Depth profile of silicon specimen diffused with phosphorus and implanted with boron. Other parameters are as defined in Figs. 5 and 6.

can be coherently summed and statistically significant counts accumulated without concern for long term system drifts. Furthermore, since the MCA can be made to integrate the number of counts in a given number of channels, one can readily ratio one mass peak to another. Using the instrumental configuration just described, the instrumental accuracy and precision of QMAS were studied by analyzing lead isotope standards which are in general use in many geochronology laboratories. The samples were provided as nitrate solutions and were prepared for the QMAS by evaporating droplets of the standard solutions onto pure quartz glass slides coated with spectrographic carbon. As the solutions dried, small mats of lead nitrate crystals were formed and these crystals were then directly analyzed. A summary of some of the typical results obtained are shown in Table 1. Taking the California Institute of Technology (CIT) specimen [8] as an example we find that based upon a set of ten separate measurements the accuracy of the determined $^{207}\text{Pb}/^{206}\text{Pb}$ ratio has an absolute error of 0.26 percent. Furthermore, it is found that the average counting error and the measured standard deviation are nearly the same indicating that we are basically limited by counting statistics. Furthermore, the small absolute error measured, together with the observed

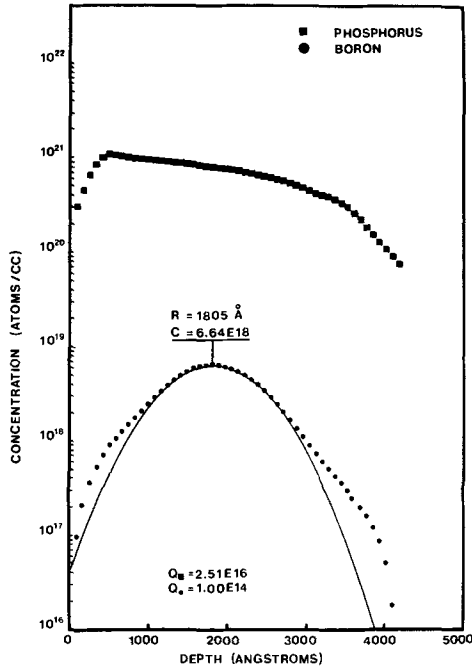


FIG. 8—Depth profile of silicon specimen diffused with phosphorus and implanted with boron. Other parameters are as previously defined.

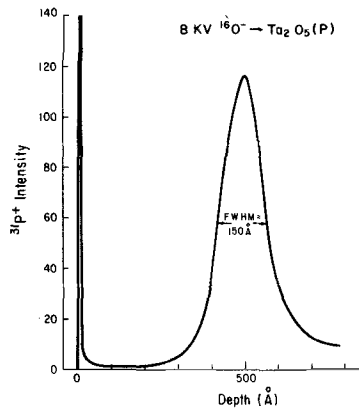


FIG. 9—QMAS detection of 50-Å-thick phosphorus enriched layer in Ta_2O_5 indicating depth resolution of the instrument under bombardment conditions specified.

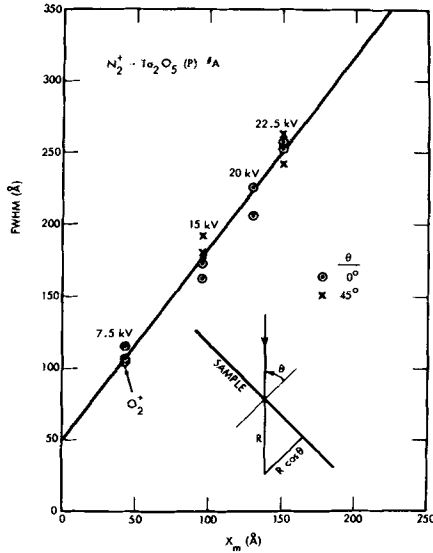


FIG. 10—The FWHM of a 50-Å-thick phosphorus enriched layer in Ta_2O_5 measured with the IMMA at different primary beam bombardment energies and angles of incidence as a function of the bombarding ion mean penetration depth X_m [6].

stability of the mass spectra obtained, give a graphic illustration that by bombarding insulators with negative ions specimen charge up can be avoided and analysis made routine.

Having established the accuracy and precision of the instrument, a study of the sensitivity of QMAS to lead in several mineral matrices of interest was made. For mineral matrices such as baddeleyite, monazite,

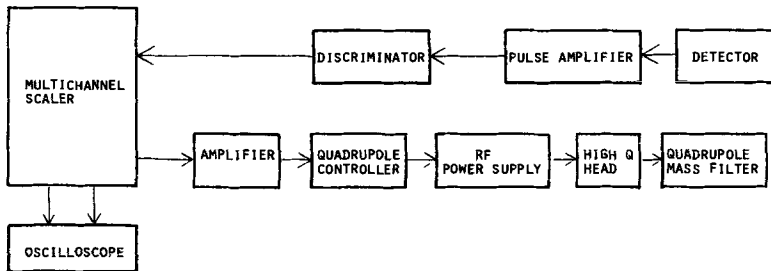


FIG. 11—Quadrupole drive and digital recording system used to measure lead isotope ratios. Multichannel scaler is responsible for both recording the data and controlling the mass range swept by the quadrupole.

TABLE 1—*Pb 207/206 precision and accuracy studies with QMAS.*

	CIT ^a	NBS 982 ^b	NBS 983 ^b
Number of measurements	10	5	11
Average value of ratio	0.93261	0.46120	0.07046
True value of ratio	0.93021	0.46707	0.071201
Absolute error, %	0.258	-1.26	-1.04
Average counting error, %	4.06	1.36	3.87
Measured standard deviation, %	4.41	0.97	2.54

^a Taken from Ref 8.

^b Catanzaro, E. J., Murphy, T. J., Shields, W. R., and Garner, E. L., *Journal of Research*, National Bureau Standards, Vol. 72A, 1968, p. 265.

and alkali feldspars which exhibit no ion interferences at mass 206 to 208, a 10-s 3σ detection limit for lead was determined to be between 1 to 3 ppma. Even for a mineral such as zircon which has a number of molecular ion interferences in the lead mass range, 206 to 208, meaningful lead isotope ratios can be determined at concentrations down to 40 ppma. This can be accomplished by removing the ion interferences using peak stripping techniques. The intensities of the peaks from 202 to 210 amu are required to correct for molecular ion interferences on ²⁰⁶Pb, ²⁰⁷Pb, and ²⁰⁸Pb. The signal at mass 203 is used as background since no peak was observed. By sequentially stripping out the interferences, the true counts and hence isotope ratios of lead can be determined. The success of this technique on a zircon specimen is illustrated by the QMAS lead age determination of 967 million years (my). This compares quite well with the previously measured age of 975 ± 25 my reported by Tilton et al [9] on this specimen and 1059 ± 39 my by the IMMA [10].

Quantitative Analysis

In the course of the work just described, a CIT glass was also analyzed. This glass was of particular interest for two important reasons. First, because its boron content was known, it afforded an opportunity to see whether or not, based upon the raw boron counts measured, QMAS could give a good quantitative analysis, and, second, to see whether or not serious mass discrimination existed in the instrument.

Through previous work with the IMMA [11] on the analysis of boron in silicon and silicon dioxide (SiO₂), a relative sensitivity factor relating boron to silicon has been derived. The relationship is as follows

$$\text{percent } ^{11}\text{B} = (11.505) \left(\frac{^{11}\text{B}^+ \text{ intensity}}{^{30}\text{Si}^+ \text{ intensity}} \right) (\text{atom fraction of silicon})$$

Applying this to the data recorded on the CIT glass we find that the boron concentration measured with QMAS of 2.83 percent agrees well with the known concentration of 2.40 percent.

In order to determine whether serious mass discrimination exists from one end of the mass spectrum to the other, the lead/silicon ratio was measured first with QMAS then IMMA. The results achieved are as follows

$$^{208}\text{Pb}^{+}/^{28}\text{Si}^{+} = 1.6 \times 10^{-4} \text{ QMAS}$$

$$^{208}\text{Pb}^{+}/^{28}\text{Si}^{+} = 1.8 \times 10^{-4} \text{ IMMA}$$

The comparable numbers obtained would indicate that in QMAS the mass discrimination as measured from 28 to 208 amu is no worse than for the IMMA, and from the quantitative work done with the IMMA it is believed that mass discrimination if any is small.

Comparison and Conclusion

Finally, although the technology developed for the IMMA has been utilized wherever possible, the unique properties of the quadrupole mass filter and the desire to produce a less complex instrument have necessitated a number of modifications. Of those modifications, three are most important. First, the IMMA has a mass separated primary beam whereas the QMAS does not. For most types of analyses performed to date with the QMAS, this has presented no serious problems. However, for those studies where the element of interest in the specimen may also be generated in the ion source (such as gases in metals) some complication in the data may result with a correspondingly higher detection limit. Second, the IMMA has a microfocus primary beam whereas the QMAS does not. For the types of analyses where spatial resolutions in excess of 100 μm are required, no serious problems are present. However, in applications where small bombarding beams are demanded, such as in small semiconductor device studies, use of a microfocus beam instrument, such as the IMMA, is required. Third, the energy band pass of the two instruments is considerably different with the IMMA having a bandpass of several hundred electron volts (eV) and QMAS of 2 to 8 eV. For many types of analyses, as has been illustrated by the results reported in the paper, this appears to cause no problem. At this time however, it is not clear as to whether or not this difference may have important implications for developing a quantitative model for QMAS similar to the model CARISMA [11] developed for IMMA. While the comparison between the QMAS measured boron concentration using an IMMA sensitivity factor and the known boron concentration in the CIT glass is encouraging, only after

additional study will it be possible to reach a final conclusion as to the implication of this important modification.

References

- [1] Roden, H. J. and Fralick, R. D., "The QMAS, A Quadrupole Mass Analyzer for Solid Samples," Paper No. 70, presented at the 26th Pittsburgh Conference, March 1975.
- [2] Colby, J. W., Miller, P., and Bridges, A. D., "Ion Microprobe Measurement of Boron Profile Redistribution During Phosphorus Diffusion," presented at the Electro-Chemical Society Meeting, San Francisco, May 1974.
- [3] Colby, J. W., "Application of the Ion Microprobe to Semiconductor Problems," presented at the Eighth National Conference on Electron Probe Analysis, New Orleans, 1973.
- [4] Evans, C. A., Jr., Colby, B. N., Kearns, G. L., and Singer, W., *Analytical Chemistry*, Vol. 45, No. 4, April 1973, pp. 398A-400A.
- [5] Andersen, C. A., Colby, J. W., Dobrott, R., Whatley, T. A., and Comaford, D. J., "Fundamental Relationships Governing Depth Resolution in the Ion Probe Mass Analyzer," Paper No. H350, presented at the 25th Pittsburgh Conference, March 1974.
- [6] Fralick, R. D., Hinthorne, J. R., and Andersen, C. A., "Feasibility of Using a Quadrupole Mass Analyzer for Solids as a Remote Sensor for the Determination of Lead Ages on Planetary Missions," NASA Contract NAS2-8247, National Aeronautics and Space Administration, Washington, D. C., Sept. 1974.
- [7] Andersen, C. A. and Hinthorne, J. R., *Geochimica et Cosmochimica Acta*, Vol. 37, 1973, pp. 745-754.
- [8] Sinha, A. K., Davis, G. H., Hart, S. R., and Krogh, T., "Lead Isotopic Analysis," Carnegie Institution Annual Report, 1969-1970, p. 386.
- [9] Tilton, G. R., Davis, G. L., Wetherill, G. W., and Aldrich, L. T., *Transactions, American Geophysical Union*, Vol. 38, 1957, pp. 360-371.
- [10] Andersen, C. A. and Hinthorne, J. R., paper to be submitted to *Geochimica et Cosmochimica Acta*, 1975.
- [11] Andersen, C. A. and Hinthorne, J. R., *Analytical Chemistry*, Vol. 45, 1973, pp. 1421-1438.

Summary

Surface analysis techniques have been on the research and development scene for several years now, and they are emerging from their infancy, where the major concern was the development and refinement of the techniques, into a stage where the application of these techniques is paramount. This is not to say that the techniques are not being developed and refined further, because many such efforts are currently under way, but rather to indicate that these are very useful techniques which are responsible for the solution of many research and development problems and the advancement of knowledge in many scientific disciplines. Also, because of the utility of these techniques, greater demands are being made of them, especially in the areas of quantification and gaining more complete knowledge of the nature of the surface. The primary goals of ASTM Subcommittee E2.02 on Surface Analysis are to provide a focal point for coordinating efforts to advance the state of the art of surface analysis and a forum for the exchange of ideas on such matters as well as establishing standard practices.

The papers in this book were compiled as a result of the Symposium for Surface Analysis Techniques for Metallurgical Applications, sponsored by ASTM Subcommittee E2.02. These papers illustrate a few areas of application of surface analysis techniques to metallurgy and metallurgical problems.

As one reads the papers in this book it is apparent that many fundamental problems remain to be explored. Most of these are related to obtaining meaningful quantitative data that can be compared specimen to specimen and technique to technique for the same specimen. Other fundamental research efforts are needed to glean more information from the available data—information not available presently.

One of the techniques utilized by almost all the authors was depth profiling the composition of the surface. This was done primarily by sputtering surface atoms with an ion beam. Depth profiling can be done also by secondary electron escape depth analysis, high energy Rutherford scattering, and secondary X-ray adsorption, but these techniques have not been employed widely nor are they understood well enough to give quantitative results. Depth profiling presents several problems in the accurate or precise determination of the composition as a function of depth into the specimen. Since a static ion beam has a Gaussian spatial distribution, the sputtering process creates a crater with a hemispherical bottom. Unless special methods are used, for example, beam rastering, signal gating, small analytical beam diameters compared to the sputtering

beam diameter, etc., the spatial resolution of the profile is determined by the crater shape. Additionally, the problem of disturbing the composition profile by the ion knock-on process degrades the profile resolution as a function of sputtering time and sputtering ion energy. Although these problems exist, depth profile analysis is possible, and methods are currently being implemented to overcome them. Several numerical techniques are available by which reasonably accurate film thicknesses can be determined from raw-profile data.

The use of ion beams as a means of determining the compositional depth profile has heightened the controversy over the decomposition or reduction of oxides by ion bombardment. This problem has not been fully resolved at this time, although there is strong evidence due to electron spectroscopy for chemical analysis (ESCA) data that something is causing a valence shift of the cation in the oxide. Data on the oxides are being taken by a number of researchers using various techniques, namely, ESCA, Auger electron spectroscopy (AES), and ion scattering spectroscopy (ISS), and comparisons of the data are not consistent with regards to the idea of reduction by bombardment. The ESCA data show zero valence cations in the oxide after bombardment; however, other surface techniques, even though they are not sensitive to valence changes, show no preferential loss of oxygen or other evidence of decomposition. Also, when bombardment energy and thermodynamic stability are considered, many inconsistencies appear.

The shape of the spectrum lines is also an area of intense interest—especially in X-ray-induced electron spectroscopy (XPS) and ESCA, and to a lesser degree in AES and ISS. Additional information concerning the nature of the surface is contained in the line shape data, and speculation as to how to extract that information is varied and needs to be explored further.

Calibration is a problem with all of these techniques, and much effort is being put into methods and standards for calibration. It is desirable that ultimately it would be possible to determine surface information independent of the technique. Whether that is a real possibility remains to be shown. Presently, surface analyses are very technique dependent as shown by several of the papers and the comparison of papers which consider similar or the same materials.

The applications of surface analysis techniques described in this book cover a wide variety of materials and processes. The ESCA or photoelectron spectroscopy has been used to examine metal and metal-oxide surfaces that have undergone specific processes or treatments. Quantitative assessments of these surfaces have been made regarding stoichiometry and oxidation states. These data are very important for obtaining optimum protective films on metals.

Auger electron spectroscopy has also been useful in protective film

analysis and studies of grain boundary segregation that leads to failures by embrittlement.

The ISS analysis of several metal-oxide surfaces have shown results that could not be interpreted as decomposition of the oxide by the ion beam as was suggested by ESCA data. However, these data were not conclusive that decomposition did not take place.

In discussing ISS, it would be remiss not to mention the work on oscillations of the cross section in ion surface scattering of Smith and Erickson, which was presented at the symposium but does not appear in this book. (The paper subsequently appeared in *Physical Review Letters*, Vol. 34, 1975, p. 297.) These oscillations, which to date have been found in only some materials, may be indicative of charge exchange between the incoming ion and the scattering center and possibly could reveal the electronic nature of the analyzed surface. Other speculations by the authors concern the use of ion scattering as a means of determining surface structure; this would supplement the other techniques, namely, low energy electron diffraction (LEED), field ion microscopy (FIM), and field emission microscopy (FEM) that are capable of surface structure determination.

Several researchers have been comparing data from the same or similar specimens using both AES and ISS. These studies show the need for a great deal of effort before the data from one technique can be converted or quantitatively compared to data from the other technique. In fact, analysis of the same data by a single technique by different researchers often does not lead to the same conclusion regarding the surface composition. This fact in itself is a significant statement as to the appropriateness of the ASTM effort in surface analysis.

A comparison has also been made between SIMS, ISS, and AES. The results show verification of data using different techniques, but they also show inconsistencies.

The secondary ion mass spectroscopy (SIMS) or ion microprobe or ion microanalyses techniques have been very useful in depth profiling and high resolution surface imaging. Attempts to put these data on a quantitative basis have met with only marginal success. Since this is a mass spectrometric technique, ion creation or production by an ion beam is of primary importance to quantitative determinations. However, this is a very complex and little understood process. The uncertainties in the ion production are a major source of error in this type of surface analysis.

It is evident from the data and discussions which were presented at this symposium that much work and cooperation is needed among researchers in surface analysis toward achieving better quantitative results. We hope that the ASTM Subcommittee E2.02 on Surface Analysis can provide some impetus toward this goal.

Index

- | A | B |
|--|---|
| Activation energy (diffusion), 72,
74, 75, 77 | Backscattering factor, 53 |
| Adhesive bonded structures, 87 | Band width, 4 |
| Chemical treatments of, 88, 93 | Beam |
| Failure of, 95, 96, 99, 100 | Current density, 117 |
| Thermal treatments of, 94 | Rastering, 93 |
| Absorbed oxygen, 21, 22 | Size, 116 |
| Alloy adherends, 86 | Boron, 128, 137 |
| Alloys | Implanted, 118, 121, 122, 123,
124, 133, 135 |
| Gold with silver, 23, 24 | |
| Nickel with | C |
| Antimony, 59 | Carbon, 79, 82 |
| Arsenic, 59 | Contamination 20 |
| Bismuth 59 | CARISMA, 102, 109, 110 |
| Boron, 28 | Chemical shift, 6 |
| Copper, 23, 24, 59 | Chromium, 118 |
| Iron, 23, 24 | Oxide (Cr_2O_3), 22 |
| Lead, 59 | Coaxial electron gun, 42 |
| Tellurium, 59 | Comparison of techniques |
| Tin, 59 | IMMA/QMAS, 138 |
| Alumina (Al_2O_3), 21, 55 | ISS/AES, 70, 79, 82, 83, 84 |
| Aluminium alloys, 79, 83, 88, 93,
94, 98 | ISS/SIMS, 91, 92, 95, 96, 98,
100 |
| Appearance Potential Spectros-
copy (APS), 7 | ISS/AES/SIMS, 86, 89 |
| Auger electron spectroscopy | ISS-SIMS/AES-SIMS, 90 |
| (AES), 9, 80 | Composition estimate by |
| Sensitivity, 83 | Attenuation of surface sensi-
tive Auger peaks, 63 |
| Auger | Peak-to-peak heights, 61 |
| Transitions, 10, 53, 55 | Copper, 21, 82, 84 |
| Lines, 10 | |

Core-level characteristic loss spectroscopy, 7

Cratering, 93, 94, 98, 115, 117, 118

Current density (beam), 117, 124

D

Depth

Profiling, 115, 128, 129, 130

Resolution, 118, 119, 120, 131

Differential scanning calorimetry, 99

Diffusion

Activation energy, 72, 74, 75, 77

Bulk, 69, 75

Chromium through gold films, 68, 76

Coefficient, 69, 72

Defect, 75

Grain boundary, 74, 75

Coefficient, 77

Kinetics, 72

Path, 71

Process, 71

Thin films, 68, 69

Dimethylamine borane, 28

Double integral amplitudes, 56

E

Electroless plating, 28

Electron energy analyzers

Cylindrical mirror type, 10, 42, 53

Retarding potential type, 9

Electron escape depth, 53, 56

Electronic aperture technique, 115, 116

Embrittlement

Antimony in iron, 59

Bismuth in copper, 59

Phosphorus in tungsten, 59

Embrittlement in nickel, 58, 64

Emitter suck, 130

Energy loss peaks, 26

Enrichment factor, 45, 51, 66

F

Field desorption spectrometer (FDS), 15

Field ion microscope (FIM), 15

Film thickness, 70

Fluorescent yield, 9

Fluorine, 25

G

Gettering of sulfur by

Manganese, 64

Hafnium, 64

Titanium, 64

Glasses, 109, 111, 112, 113, 137

Grain boundary segregation, 60

Restriction to, 66

Sulfur in nickel, 64

Grating, 94

I

Implanting, 128

Boron, 118, 121, 122, 123, 124, 133, 135

Iconel, 54

Inelastic scattering coefficients, 23

Ion backscattering, 12

Ion produced X-rays, 11

Ion microprobe mass analysis (IMMA), 101, 115

Quantitative analysis, 101

Relative errors, 106

Sensitivity, 101, 102, 104, 105, 106, 110, 124, 137

Small area depth profiling, 114, 121

Ion scattering spectrometry (ISS), 12, 80

Resolution in, 83

Sensitivity of, 83

Isotope ratio, 132, 133, 134, 137

K

Knock on, 119, 121

L

- Lifetime broadening, 6
- Lead ages, 132
- Line intensity ratios in oxides, 25
- Local thermodynamic equilibrium (LTE), 102, 109, 110
- Low energy electron diffraction (LEED), 9

M

- Magnesium oxide (MgO), 55
- Magnetite (Fe_3O_4), 20, 21
- Mass-to-charge ratio, 14
- Mean free path of electrons (inelastic scattering), 5, 7
- Multichannel analyzer, 133
- Multiple scattering, 13

N

- Nickel-boron electroless coatings
 - Analyses, 31
 - Effect of
 - Heating in air, 35
 - Heating in vacuum, 30
 - High temperature oxidation, 30
 - Mechanical abrasion, 30, 38
 - Oxidation resistance, 34
 - Preparation, 29
 - Properties, 29
- Nickel-chromia catalysts, 22
- Nickel oxides, 25

O

- Oscillator strength, 9
- Oxide thickness, 98

P

- Passive films, 39
- Peak intensity calculations
 - Auger electron spectroscopy (AES), 81
 - Ion scattering spectroscopy (ISS), 81

- Phosphorus, 123, 130, 134, 135, 136
- Photoelectron cross section, 19
- Profile area (lower limits), 122
- Profile resolution, 119
- Proton induced X-rays (PIX), 11

Q

- Quadrupole mass analyzer for solids (QMAS), 126, 127
 - Sensitivity, 128
- Quantitation techniques, 113
- Quantitative
 - Analysis, 137
 - Auger electron spectroscopy, 52
 - Surface analysis, 16, 52

R

- Raster size, 116, 119
- Rastering, 115, 128
- Resolution, 5
- Rutherford scattering, 12, 13

S

- Sampling depth, 5
- Scanning Auger microprobe (SAM), 53
- Scofield's cross section ratio, 24
- Secondary ion mass spectrometry (SIMS), 14, 87
 - Quantitation, 102
 - Sensitivity factor, 53, 54, 57
 - Boron to silicon, 137
- Sensitivity
 - Auger electron spectroscopy (AES), 83
 - Ion microprobe mass analysis (IMMA), 101, 102, 104, 105, 106, 110, 124, 137
 - Ion scattering spectrometry (ISS), 83
 - Quadrupole mass analyzer for solids (QMAS), 128
 - Secondary ion mass spectrometry (SIMS), 53, 54, 57

- Shake-up satellite structure, 35
Silicon, 118, 128, 135, 137
Silicon dioxide (SiO₂), 137
Small area depth profiling, 114, 121
Smut, 91
 Aluminium alloys, 91
 AES spectra of, 93
 ISS spectra of, 92
 SIMS spectra of, 92
Sodium, 25
 Borohydride (NaBH₄), 28, 32
Soft X-ray emission spectroscopy, 10
Sputtering, 119, 128
 Argon ion bombardment, 23, 42, 53, 59
 Depth, 60
 Preferential depletion, 24
 Profiling, 71
Stainless steel, 94, 95
 Columbium (Niobium) in, 42
 Molybdenum in, 41
 Pitting behavior, 51
 Silicon in, 41, 42
 Type 304, 44, 55
 Type 316, 55
 Type 316L, modified, 42
 Type 347, 44
 Type SP-2, 44
Steel
 Low alloy, 103, 104, 105, 106, 107, 108
 Relative sensitivity factors, 109
 Low carbon, 99
Straggling, 6, 10
Structural promoter, 22
Surface
 Charging, 19
 Chemistry, 88
 Contamination, 19
 Structure, 19
- T**
- Tantalum pentoxide (Ta₂O₅), 131, 135, 136
Thallium sulfate (Tl₂SO₄), 32
Thin film
 Aluminium, 79, 83
 Carbon, 79, 82
 Coatings, 79
 Copper, 79, 84
 Couples, 68
 Diffusion, 68
Titanium, 97
- W**
- Working curves for SIMS/IMMA, 104-108
- X**
- X-ray photoelectron spectroscopy (XPS), 6, 19
- Z**
- Zirconia (ZrO₂), 20, 21, 22, 25

